Supplementary Information for:

Selvaggio, G., Coelho, P.M.B.M., Salvador, A. (2017) "Mapping the phenotypic repertoire of the cytoplasmic 2-Cys peroxiredoxin – thioredoxin system. 1. Understanding commonalities and differences among cell types"

Table of Contents

1. The systems design space methodology for characterizing the phenotypic repertoire of biochemical circuits

1.1. Basic framework

The analysis of the dynamic properties of the PTTRS is based on the systems design space methodology [1–6], with the modifications described below relative to the published technique. These modifications aim to improve the handling of cycles and moiety conservation relationships.

The model in Figure 1 translates into the following system of ordinary differential equations:

$$
\begin{aligned}
\frac{d\,H_2O_2}{dt} &= v_{\sup} - k_{Alt}\,H_2O_2 - k_{Ox}\,Prx\text{-}S^-\,H_2O_2 - k_{Sulf}\,Prx\text{-}SO^-\,H_2O_2 \\
\frac{d\,Prx\text{-}S^-}{dt} &= k_{Red}\,Trx\text{-}S^-\,Prx\text{-}SS - k_{Ox}\,Prx\text{-}S^-\,H_2O_2 \\
\frac{d\,Prx\text{-}SO^-}{dt} &= k_{Ox}\,Prx\text{-}S^-\,H_2O_2 + k_{Srx}\,Prx\text{-}SO_2^- - k_{Sulf}\,Prx\text{-}SO^-\,H_2O_2 - k_{Cond}\,Prx\text{-}SO^- \\
\frac{d\,Prx\text{-}SO_2^-}{dt} &= k_{Sulf}\,Prx\text{-}SO^-\,H_2O_2 - k_{Srx}\,Prx\text{-}SO_2^- \\
\frac{d\,Prx\text{-}SS}{dt} &= k_{Cond}\,Prx\text{-}SO^- - k_{Red}\,Trx\text{-}S^-\,Prx\text{-}SS \\
\frac{d\,Trx\text{-}S^-}{dt} &= \frac{V_{Max}^{App}\,Trx\text{-}SS}{K_M + Trx\text{-}SS} - k_{Red}\,Trx\text{-}S^-\,Prx\text{-}SS \\
\frac{d\,Trx\text{-}SS}{dt} &= k_{Red}\,Trx\text{-}S^-\,Prx\text{-}SS - \frac{V_{Max}^{App}\,Trx\text{-}SS}{K_M + Trx\text{-}SS}
\end{aligned}
\tag{1}
$$

In order to apply the system design space methodology we must recast this system to a canonical form, called a Generalized Mass Action (GMA) system [7], such that each term in the right hand side of the equations becomes a product of power laws. In the present case, this can be straightforwardly accomplished by defining a new ancillary variable $X = K_M + Trx\text{-}SS$. Further, we note that

$$
\begin{aligned}
&\frac{d\,Prx\text{-}S^-}{dt} + \frac{d\,Prx\text{-}SO^-}{dt} + \frac{d\,Prx\text{-}SO_2^-}{dt} + \frac{d\,Prx\text{-}SS}{dt} = \\
&= \frac{d(Prx\text{-}S^- + Prx\text{-}SO^- + Prx\text{-}SO_2^- + Prx\text{-}SS)}{dt} = 0
\end{aligned}
$$

This shows that $Prx\text{-}S^- + Prx\text{-}SO^- + Prx\text{-}SO_2^- + Prx\text{-}SS = Prx_T$ is a conserved quantity, corresponding to the total concentration of peroxiredoxin. Likewise,

60 $\frac{d\,Trx\text{-}S^{-}}{dt}+\frac{d\,Trx\text{-}SS}{dt}=\frac{d(Trx\text{-}S^{-}+Trx\text{-}SS)}{dt}=0$, showing that $Trx\text{-}S^{-}+Trx\text{-}SS=Trx_T$ is also a

61 conserved quantity, corresponding to the total concentration of thioredoxin. We can simplify

62 the ordinary differential equations (ODE) system (1) by replacing two of the differential

63 equations by these conservation relationships. Upon recasting and simplification, the equations

64 are transformed to the equivalent form:

$$
\begin{aligned}
&\frac{d\,H_2O_2}{dt}=v_{\sup}-k_{Alt}\,H_2O_2-k_{Ox}\,Prx\text{-}S^{-}\,H_2O_2-k_{Sulf}\,Prx\text{-}SO^{-}\,H_2O_2\\
&\frac{d\,Prx\text{-}SO^{-}}{dt}=k_{Ox}\,Prx\text{-}S^{-}\,H_2O_2+k_{Srx}\,Prx\text{-}SO_2^{-}-k_{Sulf}\,Prx\text{-}SO^{-}\,H_2O_2-k_{Cond}\,Prx\text{-}SO^{-}\\
&\frac{d\,Prx\text{-}SO_2^{-}}{dt}=k_{Sulf}\,Prx\text{-}SO^{-}\,H_2O_2-k_{Srx}\,Prx\text{-}SO_2^{-}\\
&\frac{d\,Prx\text{-}SS}{dt}=k_{Cond}\,Prx\text{-}SO^{-}-k_{Red}\,Trx\text{-}S^{-}\,Prx\text{-}SS\\
&\frac{d\,Trx\text{-}SS}{dt}=k_{Red}\,Trx\text{-}S^{-}\,Prx\text{-}SS-V_{Max}^{App}\,Trx\text{-}SS\,X^{-1}\\
&0=K_M+Trx\text{-}SS-X\\
&0=Prx\text{-}S^{-}+Prx\text{-}SO^{-}+Prx\text{-}SO_2^{-}+Prx\text{-}SS-Prx_T\\
&0=Trx\text{-}S^{-}+Trx\text{-}SS-Trx_T
\end{aligned}
\qquad (2)
$$

66 Although not necessary for application of the system design space methodology, one can reduce

67 the dimensionality of the parameters space by scaling all parameters and variables. We used

68 the following scaling, which makes all variables and parameters dimensionless:

$$
\begin{aligned}
&\tau=k_{Cond}\,t,\\
&h=\frac{H_2O_2}{Prx_T},\quad x=\frac{Prx\text{-}S^{-}}{Prx_T},\quad y=\frac{Prx\text{-}SO^{-}}{Prx_T},\quad w=\frac{Prx\text{-}SO_2^{-}}{Prx_T},\quad z=\frac{Prx\text{-}SS}{Prx_T},\\
&r=\frac{Trx\text{-}S^{-}}{Trx_T},\quad s=\frac{Trx\text{-}SS}{Trx_T},\quad u=\frac{X}{Trx_T}\\
&\alpha=\frac{k_{Ox}\,Prx_T}{k_{Cond}},\quad \beta=\frac{k_{Alt}}{k_{Cond}},\quad \chi=\frac{K_M}{Trx_T},\quad \phi=\frac{v_{Sup}}{k_{Cond}\,Prx_T},\quad \eta=\frac{k_{Srx}}{k_{Cond}},\\
&\mu=\frac{Trx_T}{Prx_T},\quad \rho=\frac{k_{Red}\,Trx_T}{k_{Cond}},\quad \sigma=\frac{V_{Max}^{App}}{k_{Cond}\,Prx_T},\quad \psi=\frac{k_{Sulf}\,Prx_T}{k_{Cond}}.
\end{aligned}
\qquad (3)
$$

70 Scaled variables x, y, w and z represent the fractions of the peroxiredoxin pool in each

71 form, and scaled variables r, s represent the fractions of the thioredoxin pool in each form.

72 Upon this scaling, equations (2) become:

$$
\begin{aligned}
\frac{d\,h}{d\,\tau} &= \phi - (\alpha\, x\, h + \beta\, h + \psi\, y\, h) \\
\frac{d\,y}{d\,\tau} &= (\alpha\, x\, h + \eta\, w) - (y + \psi\, y\, h) \\
\frac{d\,w}{d\,\tau} &= \psi\, y\, h - \eta\, w \\
\frac{d\,z}{d\,\tau} &= y - \rho\, r\, z \\
\mu\frac{d\,s}{d\,\tau} &= \rho\, r\, z - \sigma\, s\, u^{-1} \\
0 &= (\chi + s) - u \\
0 &= (x + y + w + z) - 1 \\
0 &= (r + s) - 1
\end{aligned}
\qquad (4)
$$

The parameters space is thereby reduced from 11 $(v_{\sup}, k_{Alt}, k_{Ox}, k_{Cond}, k_{Sulf}, k_{Red}, k_{Srx}, K_M, V_{Max}^{App}, Prx_T, Trx_T)$ to 9 dimensions, of which one (corresponding to μ) is immaterial for steady state analysis.

The parentheses in equations (4) highlight that the right-hand parts of these equations are differences between two positive-coefficient linear combinations of non-negative terms. Under most conditions the value of each of these linear combinations is dominated by one of its terms. Henceforth we will denote by *dominant positive term* and *dominant negative term* the dominant terms in the positive and negative linear combinations (respectively) in an equation. For instance, if $\alpha = 20, x = 0.9, h = 0.05, \eta = 0.001, w = 0.01, y = 0.05, \psi = 0.1$, then $\alpha x h$ is the dominant positive term and y is the dominant negative term for the second equation in (4).

We will denote by *dominant subsystem* any subsystem of (4) that retains only the dominant terms of the whole system. For instance, in the case where the second consumption term for h and all the first terms in all other linear combinations are the dominant ones we obtain the dominant subsystem:

$$
\begin{aligned}
&\frac{d\,h}{d\,\tau} = \phi - \beta\, h \\
&\frac{d\,y}{d\,\tau} = \alpha\, x h - y \\
&\frac{d\,w}{d\,\tau} = \psi\, y h - \eta\, w \\
&\frac{d\,z}{d\,\tau} = y - \rho\, r\, z \\
&\mu\frac{d\,s}{d\,\tau} = \rho\, r\, z - \sigma\, s u^{-1} \\
&0 = \chi - u \\
&0 = x - 1 \\
&0 = r - 1
\end{aligned}
\quad . \qquad (5)
$$

Each system can generate $S = \prod_{i=1}^{e} P_i N_i$ dominant subsystems, where e stands for the number of equations, and P_i, N_i stand for the number of positive and negative terms (respectively) in equation *i*. For instance, the present system can generate $S =$ (1×3)(2×2)(1×1)(1×1)(1×1)(2×1)(4×1)(2×1) = 192 dominant subsystems.

Importantly, all dominant subsystems share a canonical nonlinear form such that the right-hand side of the differential equations is a difference between products of power laws. Systems exhibiting this canonical form are known as S systems [8–10] and have many desirable mathematical properties [7]. Most relevant of these, closed form analytical steady state solutions can be straightforwardly obtained upon a logarithmic transformation of all variables and parameters. For dominant subsystem (5), defining $a^* = Log(a)$, we obtain:

$$
\begin{aligned}
&\phi^* = \beta^* + h^* \\
&\alpha^* + x^* + h^* = y^* \\
&\psi^* + y^* + h^* = \eta^* + w^* \\
&y^* = \rho^* + r^* + z^* \\
&\rho^* + r^* + z^* = \sigma^* + s^* - u^* \\
&\chi^* = u^* \\
&x^* = 0 \\
&r^* = 0
\end{aligned}
\qquad (6)
$$

which yields the solution:

$$
\begin{aligned}
h^* &= \phi^* - \beta^* \\
x^* &= 0 \\
y^* &= \alpha^* + \phi^* - \beta^* \\
z^* &= \alpha^* + \phi^* - \beta^* - \rho^* \\
w^* &= 2\phi^* + \alpha^* + \psi^* - 2\beta^* - \eta^* \\
r^* &= 0 \\
s^* &= \alpha^* + \chi^* + \phi^* - \beta^* - \sigma^*
\end{aligned}
\tag{7}
$$

Each dominant subsystem approximates the behavior of the system in the region where the respective *dominance conditions* are valid. These conditions are the inequalities that define where each dominant term is higher than every other one in the respective positive or negative linear combination. For instance, the dominant subsystem (5) holds where the following set of dominance conditions is valid:

$$
\begin{aligned}
&\beta h > \alpha x h \wedge \beta h > \psi y h \wedge \\
&\alpha x h > \eta w \wedge y > \psi y h \wedge \\
&\chi > s \wedge \\
&x > y \wedge x > w \wedge x > z \wedge \\
&r > s
\end{aligned}
\tag{8}
$$

The dominance conditions define a *dominance region* in the phase space, which depends on parameters. A dominant subsystem may or may not be able to reach a steady state within its dominance region. In order to define the region of the parameters space where a dominant subsystem can attain a steady state within its dominance region, we replace its steady state solution into the dominance conditions. Again, we can transform these nonlinear inequalities to linear ones by applying the logarithmic transformation. The replaced inequalities thus become:

$$
\begin{aligned}
&\beta^* - \left(\alpha^* + \phi^*\right) > 0 \\
&\left(\beta^* + \rho^*\right) - \left(\alpha^* + \phi^*\right) > 0 \\
&\left(\beta^* + \sigma^*\right) - \left(\alpha^* + \chi^* + \phi^*\right) > 0 \\
&\left(2\beta^* + \eta^*\right) - \left(2\phi^* + \alpha^* + \psi^*\right) > 0 \\
&\beta^* - \alpha^* > 0 \\
&\beta^* - \left(\psi^* + \phi^*\right) > 0 \\
&\left(\beta^* + \sigma^*\right) - \left(\alpha^* + \phi^*\right) > 0
\end{aligned}
\tag{9}
$$

We will call these the *boundary conditions* for the dominant subsystem, and we will call the dominant subsystem *valid* if its boundary conditions are feasible.

The boundary conditions for all the valid dominant subsystems pave the parameters space into up to S discrete regions whose topology and geometry is determined by the system's interaction structure (*design*). We call this partitioned space the *system design space*.

Some dominant subsystems can be sub-determinate. This happens in systems where a fast (quasi-equilibrium) subsystem establishes under some conditions. These cases require special consideration, and can be handled in a more expedite way through the matrix formulation presented below.

System (4) can be represented in matrix form as:

$$\dot{\mathbf{X}} = \mathbf{T}.\mathbf{f}\,, \qquad (10)$$

where $\dot{\mathbf{X}}$ is the vector of time derivatives (possibly 0 for constant quantities), $\mathbf{T}$ is the $E \times T$, with T the number of different terms, is *term coefficients matrix,* and $\mathbf{f}$ is the *terms vector*. Here,

$$\mathbf{T} = \begin{bmatrix} 1 & -1 & -1 & -1 & 0 & 0 & 0 & 0 & 0 & 0 & 0 & 0 & 0 & 0 & 0 & 0 \\ 0 & 1 & 0 & -1 & 1 & -1 & 0 & 0 & 0 & 0 & 0 & 0 & 0 & 0 & 0 & 0 \\ 0 & 0 & 0 & 1 & -1 & 0 & 0 & 0 & 0 & 0 & 0 & 0 & 0 & 0 & 0 & 0 \\ 0 & 0 & 0 & 0 & 0 & 1 & -1 & 0 & 0 & 0 & 0 & 0 & 0 & 0 & 0 & 0 \\ 0 & 0 & 0 & 0 & 0 & 0 & 1 & -1 & 0 & 0 & 0 & 0 & 0 & 0 & 0 & 0 \\ 0 & 0 & 0 & 0 & 0 & 0 & 0 & 0 & 1 & 1 & -1 & 0 & 0 & 0 & 0 & 0 \\ 0 & 0 & 0 & 0 & 0 & 1 & 0 & 0 & 0 & 0 & 0 & 1 & 1 & 1 & 0 & -1 \\ 0 & 0 & 0 & 0 & 0 & 0 & 0 & 0 & 0 & 1 & 0 & 0 & 0 & 0 & 1 & -1 \end{bmatrix}, \qquad (11)$$

$$\mathbf{f} = \begin{bmatrix} \phi \\ \alpha xh \\ \beta h \\ \psi yh \\ \eta w \\ y \\ \rho rz \\ \sigma su^{-1} \\ \chi \\ s \\ u \\ x \\ w \\ z \\ r \\ 1 \end{bmatrix} \tag{12}$$

The upper left 5×8 submatrix of $\mathbf{T}$ is the reduced stoichiometric matrix of the system, and the remaining rows account for the ancillary variable and for the conservation relationships. Term coefficients matrices for dominant subsystems are obtained by selecting from each row in $\mathbf{T}$ one positive and one negative element and setting all other elements to 0. We identify each dominant subsystem by a signature in the form $(p_1, n_1, p_2, n_2, \ldots, p_e, n_e)$ where p_i and n_i are the indexes of the selected positive and negative elements in the i^{th} row of $\mathbf{T}$. Thus,

$$\mathbf{T}_{(1,3,2,6,4,5,6,7,7,8,9,11,12,16,15,16)} = \begin{bmatrix} 1 & 0 & -1 & 0 & 0 & 0 & 0 & 0 & 0 & 0 & 0 & 0 & 0 & 0 & 0 & 0 \\ 0 & 1 & 0 & 0 & 0 & -1 & 0 & 0 & 0 & 0 & 0 & 0 & 0 & 0 & 0 & 0 \\ 0 & 0 & 0 & 1 & -1 & 0 & 0 & 0 & 0 & 0 & 0 & 0 & 0 & 0 & 0 & 0 \\ 0 & 0 & 0 & 0 & 0 & 1 & -1 & 0 & 0 & 0 & 0 & 0 & 0 & 0 & 0 & 0 \\ 0 & 0 & 0 & 0 & 0 & 0 & 1 & -1 & 0 & 0 & 0 & 0 & 0 & 0 & 0 & 0 \\ 0 & 0 & 0 & 0 & 0 & 0 & 0 & 0 & 1 & 0 & -1 & 0 & 0 & 0 & 0 & 0 \\ 0 & 0 & 0 & 0 & 0 & 0 & 0 & 0 & 0 & 0 & 0 & 1 & 0 & 0 & 0 & -1 \\ 0 & 0 & 0 & 0 & 0 & 0 & 0 & 0 & 0 & 0 & 0 & 0 & 0 & 0 & 1 & -1 \end{bmatrix} \tag{13}$$

is the term coefficients matrix for the dominant subsystem (5). The rows of this matrix are linearly independent, and therefore this dominant subsystem has a unique steady state solution as seen above. However, this is not the case for, say, the dominant subsystem (1,3,5,4,4,5,6,7,8,7,9,11, 12,16,15,16):

$$\mathbf{T}_{(1,3,5,4,4,5,6,7,8,7,9,11,12,16,15,16)} =$$

$$= \begin{bmatrix} 1 & 0 & -1 & 0 & 0 & 0 & 0 & 0 & 0 & 0 & 0 & 0 & 0 & 0 & 0 & 0 \\ 0 & 0 & 0 & -1 & 1 & 0 & 0 & 0 & 0 & 0 & 0 & 0 & 0 & 0 & 0 & 0 \\ 0 & 0 & 0 & 1 & -1 & 0 & 0 & 0 & 0 & 0 & 0 & 0 & 0 & 0 & 0 & 0 \\ 0 & 0 & 0 & 0 & 0 & 1 & -1 & 0 & 0 & 0 & 0 & 0 & 0 & 0 & 0 & 0 \\ 0 & 0 & 0 & 0 & 0 & 0 & -1 & 1 & 0 & 0 & 0 & 0 & 0 & 0 & 0 & 0 \\ 0 & 0 & 0 & 0 & 0 & 0 & 0 & 0 & 1 & 0 & -1 & 0 & 0 & 0 & 0 & 0 \\ 0 & 0 & 0 & 0 & 0 & 0 & 0 & 0 & 0 & 0 & 0 & 1 & 0 & 0 & 0 & -1 \\ 0 & 0 & 0 & 0 & 0 & 0 & 0 & 0 & 0 & 0 & 0 & 0 & 0 & 0 & 1 & -1 \end{bmatrix}, \quad (14)$$

Here, the second and third rows, corresponding to the differential equations for y and w, are linearly dependent. This sub-determinate dominant subsystem thus does not permit the simultaneous determination of both y and w, but yields instead an algebraic relationship among these variables:

$$\frac{w}{y} = \frac{\psi}{\eta} h \ . \quad (15)$$

This translates the fact that under the conditions where this dominant subsystem holds a quasi-equilibrium establishes between Prx-SO^- and Prx-SO_2^- owing to rapid recycling between the sulfinylation and the sulfiredoxin-catalyzed reduction of the sulfinic acid (physiologically implausible but possible). Prx-SO^- and Prx-SO_2^- thus form an aggregated pool whose total concentration moves in a slower time scale and is determined by subdominant processes in the system. The subdominant terms that can potentially determine the concentration of the aggregated pool are those that do not cancel out upon addition of the differential equations for y and w, which expresses $\frac{d(w+y)}{dt}$. That is, those terms corresponding to non-null elements in the sum of the second and third rows of $\mathbf{T}$. By replacing one of the linearly dependent rows in $T_{(1,3,5,4,4,5,6,7,8,7,9,11,6,16,10,16)}$ by this sum, one obtains a full-rank matrix:

$$\mathbf{T}_{(1,3,(5,2),(4,6),4,5,6,7,8,7,9,11,12,16,15,16)} =$$

$$= \begin{bmatrix} 1 & 0 & -1 & 0 & 0 & 0 & 0 & 0 & 0 & 0 & 0 & 0 & 0 & 0 & 0 & 0 \\ 0 & 1 & 0 & 0 & 0 & -1 & 0 & 0 & 0 & 0 & 0 & 0 & 0 & 0 & 0 & 0 \\ 0 & 0 & 0 & 1 & -1 & 0 & 0 & 0 & 0 & 0 & 0 & 0 & 0 & 0 & 0 & 0 \\ 0 & 0 & 0 & 0 & 0 & 1 & -1 & 0 & 0 & 0 & 0 & 0 & 0 & 0 & 0 & 0 \\ 0 & 0 & 0 & 0 & 0 & 0 & -1 & 1 & 0 & 0 & 0 & 0 & 0 & 0 & 0 & 0 \\ 0 & 0 & 0 & 0 & 0 & 0 & 0 & 0 & 1 & 0 & -1 & 0 & 0 & 0 & 0 & 0 \\ 0 & 0 & 0 & 0 & 0 & 0 & 0 & 0 & 0 & 0 & 0 & 1 & 0 & 0 & 0 & -1 \\ 0 & 0 & 0 & 0 & 0 & 0 & 0 & 0 & 0 & 0 & 0 & 0 & 0 & 0 & 1 & -1 \end{bmatrix} \quad (16)$$

corresponding to a fully determinate dominant subsystem. [In this notation, the indexes in (…,(…,i),(…,j),…) express the selected subdominant terms. We will call a system generated in this way by choosing a set of subdominant terms a *subdominant subsystem*.] Note that $\mathbf{T}_{(1,3,(5,2),(4,6),4,5,6,7,8,7,9,11,12,16,15,16)} = \mathbf{T}_{(1,3,2,6,4,5,6,7,8,7,9,11,12,16,15,16)}$, and therefore the dominant subsystem (1,3,5,4,4,5,6,7,8,7,9,11,12,16,15,16) has the same steady state as the dominant subsystem (1,3,2,6,4,5,6,7,8,7,9,11,12,16,15,16). However, it holds in its own dominance region:

$$\begin{array}{l} \beta h > \alpha x h \wedge \beta h > \psi y h \wedge \\ \eta w > \alpha x h \wedge \psi y h > y \wedge \\ \chi > s \wedge \\ x > y \wedge x > w \wedge x > z \wedge \\ r > s \end{array} , \qquad (17)$$

with ensuing boundary conditions

$$\begin{array}{l} \beta^* - \alpha^* - \phi^* > 0 \\ \beta^* + \rho^* - \alpha^* - \phi^* > 0 \\ \beta^* + \sigma^* - \alpha^* - \chi^* - \phi^* > 0 \\ 2\beta^* + \eta^* - \alpha^* - \psi^* - 2\phi^* > 0 \\ 2\beta^* - \alpha^* - \psi^* - \phi^* > 0 \\ \psi^* + \phi^* - \beta^* > 0 \\ \beta^* + \sigma^* - \alpha^* - \phi^* > 0 \end{array} . \qquad (18)$$

For purposes of steady state analysis one may thus merge boundary conditions (9) and (18) into a single region.

The present example illustrates a relatively straightforward case of sub-determined dominant subsystem. However, there may be multiple quasi-equilibrium subsystems, the corresponding slow aggregated variables may not be straightforwardly identifiable, subdominant systems may have multiple subdominant subsystems, and some of the latter may be sub-determinate. Therefore, a general algorithm is necessary that handles all these possibilities. This is presented below.

1.2. Finding all the quasi-equilibrium subsystems

As illustrated in the example above, the problem of finding these quasi-equilibrium subsystems has similarities to that of finding moiety conservation relationships from the stoichiometric matrix of a reaction system. One can thus apply algorithms that were developed for the latter purpose [11] to find the $D = E - rank(\mathbf{T}_{(\ldots)})$ slow aggregated variables in a sub-

determinate dominant subsystem with term coefficients matrix $\mathbf{T}_{(...)}$. In order to do this and generate the term coefficients matrices for the subdominant subsystems we proceed as follows:

1. We first compute the left null space of $\mathbf{T}_{(...)}$, *i.e.*, the $D \times E$ matrix $\mathbf{U}$ such that $\mathbf{U}.\mathbf{T}_{(...)} = \mathbf{0}$ We then apply to $\mathbf{T}_{(...)}$ the algorithm for finding all extreme semi-positive conservation relations developed by Schuster and Höfer [11]. This algorithm returns a $F \times E, (F \leq D+1)$ matrix $\mathbf{V}$ of non-negative elements whose rows are the generating vectors of the convex polyhedral cone describing all the semi-positive conservation relations admissible by $\mathbf{T}_{(...)}$. If $F \geq D$ or all the rows of $\mathbf{U}$ are linearly dependent from those of $\mathbf{V}$ we select the first D rows from $\mathbf{V}$, and call the resulting matrix $\mathbf{B}$. If U rows from $\mathbf{U}$ cannot be expressed as a linear combination of those of $\mathbf{V}$ one picks those U rows from $\mathbf{U}$ and $D-U$ rows from $\mathbf{V}$ to form $\mathbf{B}$. The $D \times T$ matrix $\mathbf{Q} = \mathbf{B}.\mathbf{T}$ carries the coefficients of the potentially subdominant terms establishing the dynamics of each quasi-equilibrium pool.
2. From each row of $\mathbf{B}$ we select the index of a positive coordinate such that all selected indices are distinct: set $C = \{c_1, c_2, ..., c_D\}$.
3. Then, for each $c_i \in C$ we replace row c_i of $\mathbf{T}_{(...)}$ by row i of $\mathbf{Q}$.

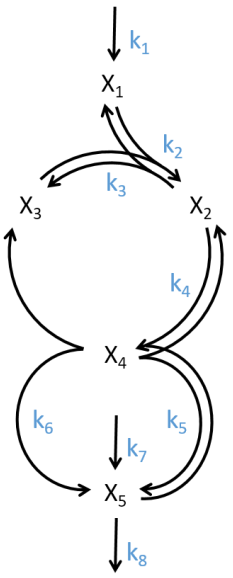

Supplementary Figure 1

This procedure can be illustrated by the example circuit in Supplementary Figure 1. The dynamics can be expressed by the system of equations:

$$\begin{aligned}
\frac{dX_1}{dt} &= k_1 + k_3 X_2 - k_2 X_1 X_3 \\
\frac{dX_2}{dt} &= k_2 X_1 X_3 + k_5 X_4 - k_3 X_2 - k_4 X_2 X_5 \\
\frac{dX_4}{dt} &= k_4 X_2 X_5 - k_5 X_4 - k_6 X_4 \\
\frac{dX_5}{dt} &= k_5 X_4 + k_6 X_4 + k_7 - k_4 X_2 X_5 - k_8 X_5 \\
0 &= X_2 + X_3 + X_4 - X_6
\end{aligned} \tag{19}$$

The steady state equations for this system can be expressed as $\mathbf{T}.\mathbf{f} = \mathbf{0}$ term coefficients matrix:

208 $$\mathbf{T}=\begin{bmatrix} 1 & 1 & -1 & 0 & 0 & 0 & 0 & 0 & 0 & 0 & 0 & 0 \\ 0 & -1 & 1 & 1 & -1 & 0 & 0 & 0 & 0 & 0 & 0 & 0 \\ 0 & 0 & 0 & -1 & 1 & -1 & 0 & 0 & 0 & 0 & 0 & 0 \\ 0 & 0 & 0 & 1 & -1 & 1 & 1 & -1 & 0 & 0 & 0 & 0 \\ 0 & 0 & 0 & 0 & 0 & 0 & 0 & 0 & 1 & 1 & 1 & -1 \end{bmatrix}. \quad (20)$$

209 and terms vector

210 $$\mathbf{f}=\begin{bmatrix} k_1 \\ k_3 X_2 \\ k_2 X_1 X_3 \\ k_5 X_4 \\ k_4 X_2 X_5 \\ k_6 X_4 \\ k_7 \\ k_8 X_5 \\ X_2 \\ X_3 \\ X_4 \\ X_6 \end{bmatrix} \quad (21)$$

211 Focusing on dominant subsystem (2,3,3,2,5,4,4,5,10,12), whose dominance region is defined by

212 $$R_{(2,3,3,2,5,4,4,5,10,12)} = f_2 > f_1 \wedge f_3 > f_4 \wedge f_4 > f_6 \wedge f_4 > f_7 \wedge f_{10} > f_9 \wedge f_{10} > f_{11} \wedge f_2 > f_5 \wedge f_5 > f_8$$

213 we find:

214 $$\mathbf{T}_{(2,3,3,2,5,4,4,5,10,12)}=\begin{bmatrix} 0 & 1 & -1 & 0 & 0 & 0 & 0 & 0 & 0 & 0 & 0 & 0 \\ 0 & -1 & 1 & 0 & 0 & 0 & 0 & 0 & 0 & 0 & 0 & 0 \\ 0 & 0 & 0 & -1 & 1 & 0 & 0 & 0 & 0 & 0 & 0 & 0 \\ 0 & 0 & 0 & 1 & -1 & 0 & 0 & 0 & 0 & 0 & 0 & 0 \\ 0 & 0 & 0 & 0 & 0 & 0 & 0 & 0 & 0 & 1 & 0 & -1 \end{bmatrix}. \quad (22)$$

215 This matrix has rank deficiency $D=2$, and accordingly we find

216 $$\mathbf{B}=\begin{bmatrix} 0 & 0 & 1 & 1 & 0 \\ 1 & 1 & 0 & 0 & 0 \end{bmatrix}, \quad (23)$$

217 identifying $X_1 + X_2$ and $X_4 + X_5$ as slow aggregated variables. Matrix $\mathbf{Q}$ is then

218 $$\mathbf{Q}=\begin{bmatrix} 0 & 0 & 0 & 0 & 0 & 0 & 1 & -1 & 0 & 0 & 0 & 0 \\ 1 & 0 & 0 & 1 & -1 & 0 & 0 & 0 & 0 & 0 & 0 & 0 \end{bmatrix}. \quad (24)$$

The third element in the first row and the first element in the second row of $\mathbf{Q}$ are non-zero. Thus, we can replace the third rows of both $\mathbf{T}$ and $\mathbf{T}_{(2,3,3,2,5,4,4,5,10,12)}$ by the first row of $\mathbf{Q}$ and the first row in the former matrices by the second row of the latter to obtain:

$$\mathbf{T}' = \begin{bmatrix} 1 & 0 & 0 & 1 & -1 & 0 & 0 & 0 & 0 & 0 & 0 & 0 \\ 0 & -1 & 1 & 1 & -1 & 0 & 0 & 0 & 0 & 0 & 0 & 0 \\ 0 & 0 & 0 & 0 & 0 & 0 & 1 & -1 & 0 & 0 & 0 & 0 \\ 0 & 0 & 0 & 1 & -1 & 1 & 1 & -1 & 0 & 0 & 0 & 0 \\ 0 & 0 & 0 & 0 & 0 & 0 & 0 & 0 & 1 & 1 & 1 & -1 \end{bmatrix}, \quad (25)$$

$$\mathbf{T}'_{(2,3,3,2,5,4,4,5,10,12)} = \begin{bmatrix} 1 & 0 & 0 & 1 & -1 & 0 & 0 & 0 & 0 & 0 & 0 & 0 \\ 0 & -1 & 1 & 0 & 0 & 0 & 0 & 0 & 0 & 0 & 0 & 0 \\ 0 & 0 & 0 & 0 & 0 & 0 & 1 & -1 & 0 & 0 & 0 & 0 \\ 0 & 0 & 0 & 1 & -1 & 0 & 0 & 0 & 0 & 0 & 0 & 0 \\ 0 & 0 & 0 & 0 & 0 & 0 & 0 & 0 & 0 & 1 & 0 & -1 \end{bmatrix}. \quad (26)$$

1.3. Handling multiple alternative subdominant terms

The first row of $\mathbf{T}'_{(2,3,3,2,5,4,4,5,10,12)}$ contains two positive elements reflecting the contributions of both reactions 1 and 4 to the aggregated pool $X_1 + X_2$, and therefore there are two subdominant subsystems: ((2,1),(3,5),3,2,(5,7),(4,8),4,5,10,12) and ((2,4),(3,5),3,2,(5,7),(4,8),4,5,10,12).

In general, each sub-determinate dominant subsystem $(p_1, n_1, ..., p_k, n_k, ..., p_E, n_E)$ can generate $A \times B$ subdominant subsystems: $(p_1, n_1, ..., (p_k, p_{i_1}), (n_k, n_{j_1}), ..., p_E, n_E)$, …, $(p_1, n_1, ..., (p_k, p_{i_A}), (n_k, n_{j_B}), ..., p_E, n_E)$, where A and B are the numbers of potentially subdominant production and consumption terms, respectively. Each of these subdominant subsystems in turn corresponds to a different dominant subsystem — $(p_1, n_1, ..., p_{i_1}, n_{j_1}, ..., p_E, n_E)$, …, $(p_1, n_1, ..., p_{i_A}, n_{j_B}, ..., p_E, n_E)$, respectively — which may be valid or invalid. The dominance region of a subdominant subsystem $(p_1, n_1, ..., (p_k, p_{i_l}), (n_k, n_{j_m}), ..., p_E, n_E)$ is the intersection between that for its originating dominant subsystem $(p_1, n_1, ..., p_k, n_k, ..., p_E, n_E)$ and the *sub-dominance region* defining where the subdominant terms $f_{p_{i_l}}$ and $f_{n_{j_m}}$ are higher than every other potentially subdominant term. More precisely, $t_{k,p_{i_l}} f_{p_{i_l}} > t_{k,p_{i_c}} f_{p_{i_c}} \wedge -t_{k,n_{j_m}} f_{n_{j_m}} > -t_{k,n_{j_d}} f_{n_{j_d}}$, $\forall_{c \in \{1,2,...,A\} \setminus \{c\}, d \in \{1,2,...,B\} \setminus \{m\}}$. The boundary conditions for the subdominant subsystem $(p_1, n_1, ..., (p_k, p_{i_l}), (n_k, n_{j_m}), ..., p_E, n_E)$ are obtained by replacing into the conditions defining its

dominance region the steady state solution for the dominant subsystem $(p_1, n_1, ..., p_{i_l}, n_{j_m}, ..., p_E, n_E)$.

Thus, the subdominance region for the subdominant subsystem ((2,4),(3,5),3,2,(5,7),(4,8),4,5,10,12) in the present example is defined by $f_4 > f_1$, and its dominance region is defined by $R_{((2,4),(3,5),3,2,(5,7),(4,8),4,5,10,12)} = R_{(2,3,3,2,5,4,4,5,10,12)} \wedge f_4 > f_1$.

1.4. Handling subdeterminate subdominant subsystems

Simple inspection of $\mathbf{T}'_{(2,3,3,2,5,4,4,5,10,12)}$ shows that $\mathbf{T}_{((2,4),(3,5),3,2,(5,7),(4,8),4,5,10,12)}$ is again subdeterminate, with $D=1$. In general, the subdetermination of $\mathbf{T}_{(p_1,n_1,...,(p_k,p_{i_l}),(n_k,n_{j_m}),...,p_E,n_E)}$ can be dealt with by iterating the steps above — treating $\mathbf{T}'$ as if it was $\mathbf{T}$ and $\mathbf{T}_{(p_1,n_1,...,(p_k,p_{i_l}),(n_k,n_{j_m}),...,p_E,n_E)}$ as if it was $\mathbf{T}_{(p_1,n_1,...,p_k,n_k,...,p_E,n_E)}$ — until no more sub-determinate dominant subsystems are generated.

In the present example, applying the procedure in point 1 we find that in this case it is not possible to express the slow aggregated variable as a positive linear combination of concentrations. We have instead:

$$\mathbf{B} = \begin{bmatrix} 1 & 0 & 0 & -1 & 0 \end{bmatrix}, \qquad (27)$$

Identifying $X_1 + X_2 - X_4$ as the new slow variable. [Note that the first row of $\mathbf{T}_{((2,4),(3,5),3,2,(5,7),(4,8),4,5,10,12)}$ contains the term coefficients for $\frac{d(X_1+X_2)}{dt}$.] Multiplying $\mathbf{B}$ by $\mathbf{T}'$ yields

$$\mathbf{Q} = \begin{bmatrix} 1 & 0 & 0 & 0 & 0 & -1 & -1 & 1 & 0 & 0 & 0 & 0 \end{bmatrix}, \qquad (28)$$

which can replace the first row of $\mathbf{T}_{((2,4),(3,5),3,2,(5,7),(4,8),4,5,10,12)}$ to give

$$\mathbf{T}'_{((2,4),(3,5),3,2,(5,7),(4,8),4,5,10,12)} = \begin{bmatrix} 1 & 0 & 0 & 0 & -1 & -1 & 1 & 0 & 0 & 0 & 0 & 0 \\ 0 & -1 & 1 & 0 & 0 & 0 & 0 & 0 & 0 & 0 & 0 & 0 \\ 0 & 0 & 0 & 0 & 0 & 0 & 1 & -1 & 0 & 0 & 0 & 0 \\ 0 & 0 & 0 & 1 & -1 & 0 & 0 & 0 & 0 & 0 & 0 & 0 \\ 0 & 0 & 0 & 0 & 0 & 0 & 0 & 0 & 0 & 1 & 0 & -1 \end{bmatrix}. \qquad (29)$$

There are now four sub-sub-dominant subsystems. Namely ((2,4,1),(3,5,5),3,2,(5,7,7),(4,8,8),4,5,10,12), with $R_{((2,4,1),(3,5,5),3,2,(5,7,7),(4,8,8),4,5,10,12)} = R_{((2,4),(3,5),3,2,(5,7),(4,8),4,5,10,12)} \wedge f_1 > f_7 \wedge f_6 > f_5$,

((2,4,1),(3,5,6),3,2,(5,7,7),(4,8,8),4,5,10,12), with

$R_{((2,4,1),(3,5,6),3,2,(5,7,7),(4,8,8),4,5,10,12)} = R_{((2,4),(3,5),3,2,(5,7),(4,8),4,5,10,12)} \wedge f_1 > f_7 \wedge f_5 > f_6$,

((2,4,7),(3,5,5),3,2,(5,7,7),(4,8,8),4,5,10,12), with

$R_{((2,4,7),(3,5,5),3,2,(5,7,7),(4,8,8),4,5,10,12)} = R_{((2,4),(3,5),3,2,(5,7),(4,8),4,5,10,12)} \wedge f_7 > f_1 \wedge f_6 > f_5$, and

((2,4,7),(3,5,6),3,2,(5,7,7),(4,8,8),4,5,10,12), with

$R_{((2,4,7),(3,5,6),3,2,(5,7,7),(4,8,8),4,5,10,12)} = R_{((2,4),(3,5),3,2,(5,7),(4,8),4,5,10,12)} \wedge f_7 > f_1 \wedge f_5 > f_6$.

All these subsystems are fully determinate, but only subsystem ((2,4,1),(3,5,6),3,2,(5,7,7),(4,8,8),4,5,10,12) has a steady state solution within its boundaries. Namely,

$$\begin{aligned} X_1^* &= k_1^* - k_2^* + k_3^* - k_4^* + k_5^* - k_6^* - k_7^* + k_8^* - X_6^* \\ X_2^* &= k_1^* - k_4^* + k_5^* - k_6^* - k_7^* + k_8^* \\ X_3^* &= X_6^* \\ X_4^* &= k_1^* - k_6^* \\ X_5^* &= k_7^* - k_8^* \end{aligned} \tag{30}$$

with boundaries

$$\begin{aligned} & k_1^* - k_7^* > 0 \wedge \\ & k_5^* - k_6^* > 0 \wedge \\ & k_3^* - k_4^* - k_7^* + k_8^* > 0 \wedge \\ & -k_1^* + k_6^* + X_6^* > 0 \wedge \\ & -k_1^* + k_4^* - k_5^* + k_6^* + k_7^* - k_8^* + X_6^* > 0. \end{aligned} \tag{31}$$

2. Design space analysis of the PTTRS model

2.1. Characterization of phenotypic regions and determination of region borders

The approach described in Section 1 yields the 13 valid dominant subsystems whose steady state properties and boundary conditions are listed in Supplementary Table 1 and Supplementary Table 2, respectively. Not all of these are representative of the phenotypes of real cells, though. To select the biologically plausible regions, one must consider the ranges of kinetic parameters and protein concentrations found in real cells. We consider the following three plausibility criteria cumulatively, which are justified in the main text.

First, reduction of sulfinylated form of peroxiredoxin is the least active process the system:

$$k_{\mathrm{Srx}} < \min(k_{\mathrm{Alt}}, k_{\mathrm{Ox}} Prx_T, k_{\mathrm{Sulf}} Prx_T, k_{\mathrm{Cond}}, k_{\mathrm{Red}} Trx_T, \frac{V_{\mathrm{Max}}^{\mathrm{App}}}{Prx_T}, \frac{V_{\mathrm{Max}}^{\mathrm{App}}}{Prx_T} \frac{Trx_T}{K_M})$$

Second, the pseudo-first order-rate constant for Prx-S^- oxidation by H_2O_2 strongly exceeds the rate constant for Prx-SO^- condensation:

$$k_{\mathrm{Ox}} Prx_T > k_{\mathrm{Cond}}$$

Third, Prx sulfinylation is the slowest among all H_2O_2-consuming processes in the model:

$$k_{\mathrm{Sulf}} Prx_T < \min(k_{\mathrm{Alt}}, k_{\mathrm{Ox}} Prx_T)$$

The steady state properties of the eight regions that satisfy these plausibility conditions are listed in Supplementary Table 1 in mathematical form in terms of unscaled variables and parameters. The boundary conditions defining each region within the parameters space are shown in Supplementary Table 2.

Supplementary Table 1. Steady state concentrations for the biologically relevant phenotypic regions. *Color code is as for Figure 2.*

Region	H_2O_2	Prx-S^-	Prx-SO^-	Prx-SS	Prx-SO_2^-	Trx-S^-	Trx-SS
HTPU	$\frac{k_{Cond}k_{Srx}Prx_T}{k_{Sulf}v_{sup}}$	$\frac{k_{Sulf}v_{sup}^2}{k_{Cond}k_{Ox}k_{Srx}Prx_T}$	$\frac{v_{sup}}{k_{Cond}}$	$\frac{v_{sup}}{k_{Red}Trx_T}$	Prx_T	Trx_T	$\frac{K_M v_{sup}}{V_{Max}^{App}}$
TTPU	$\frac{v_{sup}}{k_{Ox}Prx_T}$	Prx_T	$\frac{v_{sup}}{k_{Cond}}$	$\frac{v_{sup}}{k_{Red}Trx_T}$	$\frac{k_{Sulf}v_{sup}^2}{k_{Cond}k_{Ox}k_{Srx}Prx_T}$	Trx_T	$\frac{K_M v_{sup}}{V_{Max}^{App}}$
STAU	$\frac{v_{sup}}{k_{Alt}}$	$\frac{k_{Alt}k_{Cond}Prx_T}{k_{Ox}v_{sup}}$	Prx_T	$\frac{k_{Cond}Prx_T}{k_{Red}Trx_T}$	$\frac{k_{Sulf}Prx_T v_{sup}}{k_{Alt}k_{Srx}}$	Trx_T	$\frac{k_{Cond}K_M Prx_T}{V_{Max}^{App}}$
HTAU	$\frac{v_{sup}}{k_{Alt}}$	$\frac{k_{Alt}^2 k_{Cond}k_{Srx}Prx_T}{k_{Ox}k_{Sulf}v_{sup}^2}$	$\frac{k_{Alt}k_{Srx}Prx_T}{k_{Sulf}v_{sup}}$	$\frac{k_{Alt}k_{Cond}k_{Srx}Prx_T}{k_{Red}k_{Sulf}v_{sup}Trx_T}$	Prx_T	Trx_T	$\frac{k_{Alt}k_{Cond}k_{Srx}Prx_T K_M}{k_{Sulf}V_{Max}^{App}v_{sup}}$
TTAU	$\frac{v_{sup}}{k_{Alt}}$	Prx_T	$\frac{k_{Ox}Prx_T v_{sup}}{k_{Alt}k_{Cond}}$	$\frac{k_{Ox}Prx_T v_{sup}}{k_{Alt}k_{Red}Trx_T}$	$\frac{k_{Ox}k_{Sulf}Prx_T v_{sup}^2}{k_{Alt}^2 k_{Cond}k_{Srx}}$	Trx_T	$\frac{k_{Ox}K_M Prx_T v_{sup}}{k_{Alt}V_{Max}^{App}}$
DTAU	$\frac{v_{sup}}{k_{Alt}}$	$\frac{k_{Alt}k_{Red}Prx_T Trx_T}{k_{Ox}v_{sup}}$	$\frac{k_{Red}Prx_T Trx_T}{k_{Cond}}$	Prx_T	$\frac{k_{Red}k_{Sulf}Prx_T v_{sup}Trx_T}{k_{Alt}k_{Cond}k_{Srx}}$	Trx_T	$\frac{k_{Red}K_M Prx_T Trx_T}{V_{Max}^{App}}$
DDAU	$\frac{v_{sup}}{k_{Alt}}$	$\frac{k_{Alt}V_{Max}^{App}Trx_T}{k_{Ox}K_M v_{sup}}$	$\frac{V_{Max}^{App}Trx_T}{k_{Cond}K_M}$	Prx_T	$\frac{k_{Sulf}Trx_T v_{sup}V_{Max}^{App}}{k_{Alt}k_{Cond}k_{Srx}K_M}$	$\frac{V_{Max}^{App}Trx_T}{k_{Red}K_M Prx_T}$	Trx_T
DDAS	$\frac{v_{sup}}{k_{Alt}}$	$\frac{k_{Alt}V_{Max}^{App}}{k_{Ox}v_{sup}}$	$\frac{V_{Max}^{App}}{k_{Cond}}$	Prx_T	$\frac{k_{Sulf}V_{Max}^{App}v_{sup}}{k_{Alt}k_{Cond}k_{Srx}}$	$\frac{V_{Max}^{App}}{k_{Red}Prx_T}$	Trx_T

300 ***Supplementary Table 2. Boundary conditions for the biologically relevant phenotypic regions.***

Region	Boundary conditions
HTPU	$\max\left(k_{\mathrm{Srx}}Prx_{\mathrm{T}}, \sqrt{\frac{k_{\mathrm{Alt}}k_{\mathrm{Cond}}k_{\mathrm{Srx}}Prx_{\mathrm{T}}}{k_{\mathrm{Sulf}}}}\right) < v_{\mathrm{sup}} <$ $< \min\left(k_{\mathrm{Cond}}Prx_{\mathrm{T}}, \sqrt{\frac{k_{\mathrm{Cond}}k_{\mathrm{Ox}}k_{\mathrm{Srx}}}{k_{\mathrm{Sulf}}}}Prx_{\mathrm{T}}, k_{\mathrm{Red}}Prx_{\mathrm{T}}Trx_{\mathrm{T}}, V_{Max}^{App}, \frac{V_{Max}^{App}}{K_M}Trx_{\mathrm{T}}\right)$
TTPU	$v_{\mathrm{sup}} < \min\left(k_{\mathrm{Cond}}Prx_{\mathrm{T}}, \sqrt{\frac{k_{\mathrm{Cond}}k_{\mathrm{Ox}}k_{\mathrm{Srx}}}{k_{\mathrm{Sulf}}}}Prx_{\mathrm{T}}, \frac{k_{\mathrm{Cond}}k_{\mathrm{Ox}}}{k_{\mathrm{Sulf}}}Prx_{\mathrm{T}}, k_{\mathrm{Red}}Prx_{\mathrm{T}}Trx_{\mathrm{T}}, V_{Max}^{App}, \frac{V_{Max}^{App}}{K_M}Trx_{\mathrm{T}}\right) \wedge k_{\mathrm{Alt}} < k_{\mathrm{Ox}}Prx_{\mathrm{T}}$
STAU	$V_{Max}^{App} > k_{\mathrm{Cond}}Prx_{\mathrm{T}} \max\left(1, \frac{K_M}{Trx_{\mathrm{T}}}\right) \wedge Trx_{\mathrm{T}} > \frac{k_{\mathrm{Cond}}}{k_{\mathrm{Red}}} \wedge k_{\mathrm{Alt}} > k_{\mathrm{Sulf}}Prx_{\mathrm{T}} \wedge$ $\wedge k_{\mathrm{Cond}} \max\left(\frac{k_{\mathrm{Alt}}}{k_{\mathrm{Ox}}}, Prx_{\mathrm{T}}\right) < v_{\mathrm{sup}} < \frac{k_{\mathrm{Alt}}k_{\mathrm{Srx}}}{k_{\mathrm{Sulf}}}$
HTAU	$v_{\mathrm{sup}} > \frac{k_{\mathrm{Alt}}k_{\mathrm{Srx}}}{k_{\mathrm{Sulf}}} \max\left(1, \sqrt{\frac{k_{\mathrm{Cond}}k_{\mathrm{Sulf}}}{k_{\mathrm{Ox}}k_{\mathrm{Srx}}}}, \frac{k_{\mathrm{Cond}}}{k_{\mathrm{Red}}Trx_{\mathrm{T}}}, \frac{k_{\mathrm{Cond}}Prx_{\mathrm{T}}}{V_{Max}^{App}}, \frac{k_{\mathrm{Cond}}Prx_{\mathrm{T}}}{V_{Max}^{App}}\frac{K_M}{Trx_{\mathrm{T}}}\right) \wedge$ $\wedge\left(\sqrt{\frac{k_{\mathrm{Alt}}k_{\mathrm{Cond}}k_{\mathrm{Srx}}Prx_{\mathrm{T}}}{k_{\mathrm{Sulf}}}} < v_{\mathrm{sup}} < \frac{k_{\mathrm{Alt}}k_{\mathrm{Cond}}}{k_{\mathrm{Sulf}}} \vee v_{\mathrm{sup}} > \max\left(\frac{k_{\mathrm{Alt}}k_{\mathrm{Cond}}}{k_{\mathrm{Sulf}}}, k_{\mathrm{Srx}}Prx_{\mathrm{T}}\right)\right)$
TTAU	$v_{\mathrm{sup}} < \frac{k_{\mathrm{Alt}}}{k_{\mathrm{Ox}}Prx_{\mathrm{T}}} \min\left(k_{\mathrm{Cond}}Prx_{\mathrm{T}}, \frac{k_{\mathrm{Cond}}}{k_{\mathrm{Sulf}}}k_{\mathrm{Alt}}, \sqrt{\frac{k_{\mathrm{Cond}}k_{\mathrm{Ox}}}{k_{\mathrm{Sulf}}}k_{\mathrm{Srx}}}Prx_{\mathrm{T}}, k_{\mathrm{Red}}Prx_{\mathrm{T}}Trx_{\mathrm{T}}, V_{Max}^{App}, \frac{V_{Max}^{App}}{K_M}Trx_{\mathrm{T}}\right) \wedge k_{\mathrm{Alt}} > k_{\mathrm{Ox}}Prx_{\mathrm{T}}$
DTAU	$k_{\mathrm{Red}}Trx_{\mathrm{T}} \max\left(\frac{k_{\mathrm{Alt}}}{k_{\mathrm{Ox}}}, Prx_{\mathrm{T}}\right) < v_{\mathrm{sup}} < \frac{k_{\mathrm{Alt}}k_{\mathrm{Cond}}k_{\mathrm{Srx}}}{k_{\mathrm{Red}}k_{\mathrm{Sulf}}Trx_{\mathrm{T}}} \wedge$ $\wedge V_{Max}^{App} > k_{\mathrm{Red}}K_M Prx_{\mathrm{T}} \wedge Trx_{\mathrm{T}} < \frac{k_{\mathrm{Cond}}}{k_{\mathrm{Red}}} \min\left(1, \frac{k_{\mathrm{Alt}}}{k_{\mathrm{Sulf}}Prx_{\mathrm{T}}}, \frac{V_{Max}^{App}}{k_{\mathrm{Cond}}Prx_{\mathrm{T}}}\right)$
DDAU	$\frac{V_{Max}^{App}}{K_M}Trx_{\mathrm{T}} \max\left(1, \frac{k_{\mathrm{Alt}}}{k_{\mathrm{Ox}}Prx_{\mathrm{T}}}\right) < v_{\mathrm{sup}} < \frac{k_{\mathrm{Alt}}k_{\mathrm{Cond}}k_{\mathrm{Srx}}K_M Prx_{\mathrm{T}}}{k_{\mathrm{Sulf}}V_{Max}^{App}Trx_{\mathrm{T}}} \wedge$ $\wedge Trx_{\mathrm{T}} < K_M \min\left(1, \frac{k_{\mathrm{Alt}}k_{\mathrm{Cond}}}{k_{\mathrm{Sulf}}V_{Max}^{App}}, \frac{k_{\mathrm{Cond}}Prx_{\mathrm{T}}}{V_{Max}^{App}}, \frac{k_{\mathrm{Red}}Prx_{\mathrm{T}}Trx_{\mathrm{T}}}{V_{Max}^{App}}\right)$
DDAS	$V_{Max}^{App} \max\left(1, \frac{k_{\mathrm{Alt}}}{k_{\mathrm{Ox}}Prx_{\mathrm{T}}}\right) < v_{\mathrm{sup}} < \frac{k_{\mathrm{Alt}}k_{\mathrm{Cond}}}{k_{\mathrm{Sulf}}}\frac{k_{\mathrm{Srx}}Prx_{\mathrm{T}}}{V_{Max}^{App}} \wedge$ $\wedge V_{Max}^{App} < \min\left(\frac{k_{\mathrm{Alt}}k_{\mathrm{Cond}}}{k_{\mathrm{Sulf}}}, k_{\mathrm{Cond}}Prx_{\mathrm{T}}, k_{\mathrm{Red}}Prx_{\mathrm{T}}Trx_{\mathrm{T}}\right) \wedge Trx_{\mathrm{T}} > K_M$

2.2. Inventory of the qualitatively distinct arrangements of phenotypic regions and responses

The qualitatively distinct arrangements (relative positions) of the phenotypic regions in the various slices of the $\left(v_{\sup}, V_{Max}^{App}\right)$ plane [or similarly, in the $\left(\phi^*, \sigma^*\right)$ plane, in logarithmic scaled coordinates, as per Section 1] determines a set of qualitatively different responses to $v_{\sup}$ and to TrxR inhibition. In what follows we are only interested in *generic* arrangements; that is in those that do not hold just for a specific pointwise condition. In order to enumerate all the qualitatively distinct arrangements we proceeded as follows. These relative positions are

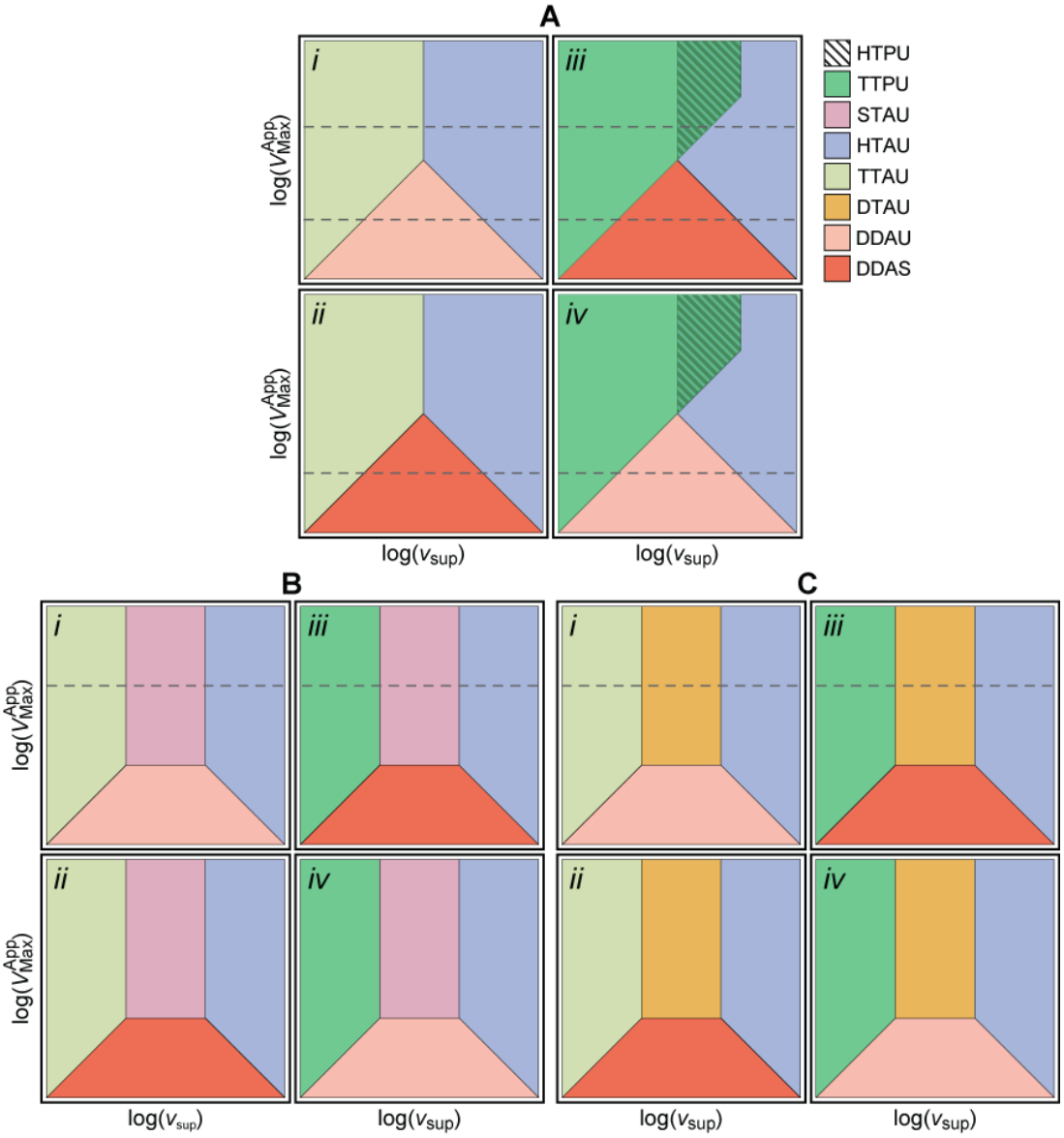

Supplementary Figure 2. The generic qualitatively different arrangements of phenotypic regions for slices in the $\left(v_{\sup}, V_{Max}^{App}\right)$ ***plane.*** *The gray dashed lines illustrate the ten generic qualitatively different responses to* $v_{\sup}$ *.*

determined by the set of relationships in Supplementary Table 2. More concretely, by the relative values of the various sub-expressions entering the inequalities. Expressed in terms of the logarithms of the scaled parameters introduced in Section 1, these inequalities can be written as function of the following 9 quantities:

$$\rho^*, \chi^*, 0, \alpha^* - \beta^*, \alpha^* - \psi^* + \eta^*, \beta^* - \psi^* + \eta^*, \frac{\alpha^* - \beta^*}{2}, \frac{\alpha^* - \psi^* + \eta^*}{2}, \frac{\beta^* - \psi^* + \eta^*}{2} \quad (32)$$

There can be 9!= 362 880 distinct orderings of these quantities, (e.g., $\rho^* < \chi^* < 0 < \alpha^* - \beta^* < < \alpha^* - \psi^* + \eta^* < \beta^* - \psi^* + \eta^* < \frac{\alpha^* - \beta^*}{2} < \frac{\alpha^* - \psi^* + \eta^*}{2} < \frac{\beta^* - \psi^* + \eta^*}{2}$), each of which corresponding to one subsector of the full-dimensional design space. However, only 1152 of these orderings (subsectors) satisfy the plausibility constraints introduced in Section 2.1. Each ordering is consistent with one and only one arrangement of the phenotypic regions in the (ϕ^*, σ^*) plane. After examining all the 1152 biologically plausible orderings, we find that only the 12 arrangements shown in Supplementary Figure 2 are possible. Combining this analysis with that of the properties that characterize each region (as per Supplementary Table 1 and Table 1) these 12 arrangements can be grouped by similarity of the responses at high V_{Max}^{App} into three major families (A, B, C) as follows. In family A (Supplementary Figure 2A), increasing $v_{\sup}$ leads directly from a region where Prx-S^- is the dominant Prx form (TTPU or TTAU) to region HTAU, where Prx-SO_2^- is the dominant Prx form. In turn, families B (Supplementary Figure 2B) and C (Supplementary Figure 2C) are characterized by regions at intermediate $v_{\sup}$ where Prx accumulates in Prx-SO^- or Prx-SS forms, respectively. Each of these families has four variants (*i-iv*), characterized by the nature of the basal (*i.e.*, low $v_{\sup}$) state and by TrxR saturation at intermediate $v_{\sup}$ and low V_{Max}^{App}.

The necessary and sufficient conditions for each arrangement to hold are straightforwardly derived as the reunion of all subsectors that are consistent with it (*i.e.*, ORing all the consistent ordering conditions). The conditions for the four arrangements that are represented in our sample of cell types are presented in Figure 2.

One can recognize 10 qualitatively different generic responses to $v_{\sup}$ (Supplementary Figure 2, Figure 2), defined by as many different region sequences. The conditions for occurrence of each of these responses are shown in Supplementary Table 3.

Supplementary Table 3. Generic qualitatively different responses of the PTTRS to v_{sup} and the conditions for their occurrence.

Response*	Sequence	Condition
A	TTAU → HTAU	$\frac{k_{Ox}}{k_{Cond}k_{Sulf}}k_{Srx} < \frac{k_{Ox}Prx_T}{k_{Alt}} < 1 \wedge \sqrt{\frac{k_{Cond}k_{Ox}}{k_{Sulf}}k_{Srx}Prx_T} < \min\left(k_{Red}Trx_T Prx_T, V_{Max}^{App}, V_{Max}^{App}\frac{Trx_T}{K_M}\right)$
P	TTPU → (HTPU) → HTAU	$\max\left(k_{Srx}Prx_T, \sqrt{\frac{k_{Cond}}{k_{Sulf}}k_{Srx}k_{Alt}Prx_T}\right) < \min\left(k_{Cond}Prx_T, \sqrt{\frac{k_{Cond}k_{Ox}}{k_{Sulf}}k_{Srx}Prx_T}, k_{Red}Prx_T Trx_T, V_{Max}^{App}, \frac{V_{Max}^{App}}{K_M}Trx_T\right)$
AS	TTAU → STAU → HTAU	$k_{Cond}Prx_T < \min\left(k_{Red}Trx_T Prx_T, \frac{k_{Ox}k_{Srx}}{k_{Sulf}}Prx_T, V_{Max}^{App}, V_{Max}^{App}\frac{Trx_T}{K_M}\right) \wedge k_{Alt} > \max\left(k_{Ox}, k_{Sulf}\right)Prx_T$
PS	TTPU → STAU → HTAU	$k_{Cond}Prx_T < \min\left(k_{Red}Trx_T Prx_T, \frac{k_{Alt}k_{Srx}}{k_{Sulf}}, V_{Max}^{App}, V_{Max}^{App}\frac{Trx_T}{K_M}\right) \wedge k_{Sulf}Prx_T < k_{Alt} < k_{Ox}Prx_T$
AD	TTAU → DTAU → HTAU	$k_{Red}Trx_T Prx_T < \min\left(k_{Cond}Prx_T, \frac{k_{Cond}}{k_{Sulf}}k_{Alt}, \sqrt{\frac{k_{Cond}k_{Ox}}{k_{Sulf}}k_{Srx}Prx_T}, V_{Max}^{App}, V_{Max}^{App}\frac{Trx_T}{K_M}\right) \wedge k_{Alt} > k_{Ox}Prx_T$
PD	TTPU → DTAU → HTAU	$k_{Red}Trx_T Prx_T < \min\left(k_{Cond}Prx_T, \frac{k_{Cond}}{k_{Sulf}}k_{Alt}, \sqrt{\frac{k_{Cond}}{k_{Sulf}}k_{Srx}k_{Alt}Prx_T}, V_{Max}^{App}, V_{Max}^{App}\frac{Trx_T}{K_M}\right) \wedge k_{Alt} < k_{Ox}Prx_T$
ADU	TTAU → DDAU → HTAU	$V_{Max}^{App} < \frac{K_M}{Trx_T}\min\left(k_{Cond}Prx_T, k_{Red}Trx_T Prx_T, \frac{k_{Cond}}{k_{Sulf}}k_{Alt}, \sqrt{\frac{k_{Cond}k_{Ox}}{k_{Sulf}}k_{Srx}Prx_T}\right) \wedge k_{Alt} > k_{Ox}Prx_T \wedge Trx_T < K_M$
PDU	TTPU → DDAU → HTAU	$V_{Max}^{App} < \frac{K_M}{Trx_T}\min\left(k_{Cond}Prx_T, k_{Red}Trx_T Prx_T, \frac{k_{Cond}}{k_{Sulf}}k_{Alt}, \sqrt{\frac{k_{Cond}}{k_{Sulf}}k_{Srx}k_{Alt}Prx_T}\right) \wedge k_{Alt} < k_{Ox}Prx_T \wedge Trx_T < K_M$
ADS	TTAU → DDAS → HTAU	$V_{Max}^{App} < \min\left(k_{Cond}Prx_T, k_{Red}Trx_T Prx_T, \frac{k_{Cond}}{k_{Sulf}}k_{Alt}, \sqrt{\frac{k_{Cond}k_{Ox}}{k_{Sulf}}k_{Srx}Prx_T}\right) \wedge k_{Alt} > k_{Ox}Prx_T \wedge Trx_T > K_M$
PDS	TTPU → DDAS → HTAU	$V_{Max}^{App} < \min\left(k_{Cond}Prx_T, k_{Red}Trx_T Prx_T, \frac{k_{Cond}}{k_{Sulf}}k_{Alt}, \sqrt{\frac{k_{Cond}}{k_{Sulf}}k_{Srx}k_{Alt}Prx_T}\right) \wedge k_{Alt} < k_{Ox}Prx_T \wedge Trx_T > K_M$

*Responses are named as follows: 1st character: basal (low v_{sup}) state: A = TTAU, P = TTPU. 2nd character: dominant Prx form in the intermediate v_{sup} region if one exists: S = Prx-SO$^-$, D = Prx-SS. 3rd character: TrxR saturation if Trx-SS is the dominant Trx form in the intermediate region: S = saturated, U = unsaturated.

3. Parameter Estimations

3.1. Estimation of protein concentrations in human cells from proteomic datasets

Where more reliable determinations were lacking, we estimated protein concentrations in human cell lines based on the proteomic dataset from Geiger *et al.* [12] as reported in the Proteomaps database (http://www.proteomaps.net/) [13]. Geiger *et al.* [12] report the absolute protein abundance estimates for eleven human cell lines. The data for all these cell types was obtained through the same methods in a single lab, and applying the most accurate approach for proteome-scale absolute protein quantification. Furthermore, most proteins of the PTTRS are very abundant and can thus be more precisely quantified than most other proteins.

The estimates follow the method of Milo *et al.* [14]. They are based on the observation that most mammalian cells have a mean protein density of 0.2 g/mL cell volume [15,16]. For instance, Jurkat T cells contain 0.14 mg protein/10^6 cells [17], which translates into C_p= 0.21 g/mL, considering a mean Jurkat T cell volume of 6.6±0.46×10^{-13} dm^3 [18]. Then, considering that an average human protein contains 375 aminoacyl residues ($\overline{Laa}$ below) [19], and a mean molecular weight of 110 Da per aminoacid, and that only about $f_{water} = 0.7$ of the cell volume is occupied by water [20] we obtain the following average concentration of total protein in a human cell:

$$C_{tot} = \frac{0.21\,(\mathrm{g/mL})}{0.7 \times 110\,(\mathrm{Da}) \times 375\,(\mathrm{aa})} = 7.0\,\mathrm{mM} \tag{33}$$

Knowing the mass fraction (φ_{Prot} , expressed as "size weighted abundance" in the Proteomaps database) and its primary sequence length (Laa_{Prot}) one can then calculate its concentration by applying the following formula:

$$C_{\mathrm{Prot}} = \frac{\varphi_{\mathrm{Prot}}\, C_{tot}}{\frac{Laa_{\mathrm{Prot}}}{\overline{Laa}}} \tag{34}$$

Wiśniewski *et al.* [21] performed a quantitative proteomic analysis of human hepatocytes and of HepG2 cells and expressed their results (c_{Prot}) as nmol/mg total protein. In order to refer these concentrations to cell water volume we apply the following conversion:

$$C_{\mathrm{Prot}} = \frac{C_p}{f_{water}} c_{\mathrm{Prot}} = 2.9 \times 10^{2}\,(\mathrm{g\ dm^{-3}}) \times 10^{-9}\,(\mathrm{mol\ nmol^{-1}}) \times c_{\mathrm{Prot}}\,. \quad (367)$$

Many of the proteins of interest in this study are confined to the cytoplasm. Their cytoplasmic concentration can be readily estimated by dividing C_{Prot} by the cytoplasm volume fraction, $f_{cytoplasm}$. A few other proteins are distributed by other compartments as well, and in these cases we assume that their concentration is identical in the various compartments. Therefore, unless otherwise stated we estimate their cytoplasmic concentration by dividing C_{Prot} by the sum of the volumes of the compartments where the protein is present. Subcellular localizations were obtained from the Uniprot database (http://www.uniprot.org/) [22], neglecting those that were just electronically inferred and not confirmed experimentally. Compartment volume fractions were estimated from the literature, or $f_{cytoplasm} = f_{nucleus} = 0.5$ was assumed when no data was available (Supplementary Table 4).

Supplementary Table 4. Cell volume fractions of nucleus and cytoplasm for human cells.

	Cell type	$f_{nucleus}$	$f_{cytoplasm}$	***Ref.***
Jurkat T	Acute T-Cell leukemia	0.6	0.3	[18] [a]
A549	Lung carcinoma	0.28	0.72	[23]
GaMG	Glioblastoma	*0.5*	*0.5*	[b]
HEK293	Embryonic kidney cells	0.56	0.44	[24]
HeLa	Cervical carcinoma	0.18	0.78	[25]
HepG2	Hepatoma	0.25	0.63	[21] [c,d]
K562	Chronic myeloid leukemia	0.5	0.5	[26] [e]
LnCap	Prostate carcinoma	0.44	0.56	[27] [f]
MCF-7	Mammary carcinoma	0.53	0.47	[28]
RKO	Colon carcinoma	*0.5*	*0.5*	[b]
U2-OS	Osteosarcoma	0.5	0.5	[29] [f]
Hepatocyte		0.10	0.53	[21] [c,g]

[a] *Mitochondria account for 5% of cell volume.*
[b] *Assumed.*
[c] *Estimate based on relative protein masses in each compartment.*
[d] *Mitochondria account for 12% of cell volume, as inferred from protein mass.*
[e] *Estimated by visual inspection of microscopy images.*
[f] *Estimated using 2D-area data to approximate the partition of the intracellular space in cytoplasm and nucleus.*
[g] *Mitochondria and endoplasmic reticulum + Golgi account for 25% and 12% of cell volume, respectively, as inferred from protein mass.*

3.2. Estimations for Jurkat T Cells

Jurkat T are arguably the nucleated human cells where the PTTRS has been most thoroughly characterized. For this reason, we used them as a reference for the estimation of the parameters for other nucleated human cell types. In the sections below we also discuss information for these other cells, where available.

3.2.1. H_2O_2 Permeability

Cells' permeability to H_2O_2 can be determined from the experimentally observable decay exponent of extracellular H_2O_2 provided that the internal H_2O_2 consumption activity is either known or sufficient to outcompete the H_2O_2 efflux and the morphometric parameters are available (see *eg.* [30]). Based on the diagram in Supplementary Figure 3, the dynamics of permeation can be described by the following model:

$$\begin{aligned}\frac{d\,H_2O_{2,out}}{dt} &= \frac{n_{cells}\kappa_p S}{V_{medium}}(H_2O_{2,in} - H_2O_{2,out}) \\ \frac{d\,H_2O_{2,in}}{dt} &= \frac{\kappa_p S}{V_{in}}(H_2O_{2,out} - H_2O_{2,in}) - k_{sink}H_2O_{2,in}.\end{aligned} \tag{35}$$

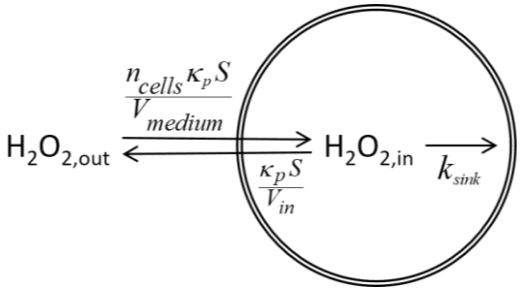

Supplementary Figure 3. Model for cell permeation by H_2O_2.

Here, n_{cells} stands for the number of cells per medium volume V_{medium}, κ_p stands for the permeability constant, S and V_{in} stand for the permeant surface area and cytoplasmic water volume, and k_{sink} stands for the pseudo-first order rate constant for H_2O_2 consumption in the cytoplasm. After a short time period in the order of $1/\left(k_{sink} + \frac{\kappa_p S}{V_{in}}\right)$, $H_2O_{2,in}$ approaches a quasi-steady state

$$H_2O_{2,in}(t) = \frac{H_2O_{2,out}(t)}{1 + \frac{k_{sink}\,V_{in}}{\kappa_p S}}\,. \tag{}$$

Replacing this equation into equation (35) and integrating yields

$$H_2O_{2,out}(t) = H_2O_{2,out}(0)e^{-k_{cells}t}\,, \tag{36}$$

with

411 $$k_{cells} = \frac{n_{cells}}{V_{medium}} \frac{\kappa_p S}{1 + \frac{\kappa_p S}{k_{sink} V_{in}}} \quad (37)$$

412 being the decay exponent. It follows from this equation that under experimental conditions
413 where cells retain sufficient cytoplasmic H_2O_2 clearance activity to strongly outcompete the H_2O_2
414 efflux (*i.e.*, $k_{\text{sink}} \gg \frac{\kappa_p S}{V_{in}}$) the permeability per cell — $\kappa_p \times S$ — and the pseudo-first order rate
415 constant for H_2O_2 influx (k_{inf}) can be straightforwardly computed from k_{cells} :

416 $$\kappa_p \times S = \frac{V_{medium}}{n_{cells}} k_{cells}, \quad (38)$$

417 $$k_{\text{inf}} = \frac{\kappa_p S}{V_{in}} \ . \quad (39)$$

418 These conditions are met in experiments where H_2O_2 concentrations in the medium are kept
419 low enough to avoid extensive oxidation of the Prx and other peroxidases, or where cells have
420 a high cytoplasmic catalase activity. A $k_{sink} \geq 100\,\text{s}^{-1}$ would warrant accurate determinations.
421 This is achieved if the Prx are no more than 70% oxidized or inhibited, or if cells contain abundant
422 cytoplasmic Cat activity. The latter is the case for human erythrocytes, which permitted
423 estimating $\kappa_p = 5.8 \times 10^{-5}\ \text{dm}\,\text{s}^{-1}$ and $k_{\text{inf}} = 11.\ \text{s}^{-1}$ [31].

424 However, the following observations indicate that the conditions above are not met in most
425 determinations of k_{cells} published so far [e.g. ,32–35]. Determinations of k_{cells} for a variety of
426 cell lines strongly correlate with cells' Cat activity [35], and inhibition of Cat with 3-aminotriazole
427 decreases the value of k_{cells} by 1.2 to 4.6-fold, for determinations based on high H_2O_2 doses per
428 cell [34,35]. Should these values of k_{cells} be determined by the cells' permeability they would
429 be virtually independent of the Cat activity.

430 Likewise, all the determinations of k_{cells} of HEK293 in ref. [33] were done under conditions
431 where PrxII (and presumably also PrxI) was mostly oxidized. Because in HEK293 cells, as in most
432 other human cells, Cat is confined within peroxisomes, it cannot effectively compete with the
433 H_2O_2 efflux. The value of k_{cells} should thus reflect not the permeability of the cell membrane
434 but the activity of Cat (limited by permeation of the peroxisomal membrane) plus some residual
435 peroxidase activity.

In lack of information about the value of k_{sink} that applies under these conditions, the value of k_{cells} can provide just lower bounds for the permeability and influx rate constant (k_{inf}). Such a lower bound for k_{inf} in HEK293 cells can be obtained based on the observation [33] that 1.5×10^6 cells grown on 2.5 mL of medium consume H_2O_2 with $k_{cells} = 1.35\times10^{-3}\ \mathrm{s^{-1}}$, considering a $V_{cytoplasm} = 8.22\times10^{-13}\ \mathrm{dm^3}$ [24] and a water content of 0.7 mL water/mL cell:

$$k_{\mathrm{inf}} > \frac{V_{medium}}{n_{cells} f_{water} V_{cytoplasm}} k_{cells} = \frac{2.5\times10^{-3}\ \mathrm{dm^3}}{(1.5\times10^{6}\ \mathrm{cells})\times 0.7 \times (8.22\times10^{-13}\ \mathrm{dm^3})} 1.35\times10^{-3}\ \mathrm{s^{-1}} = 3.9\ \mathrm{s^{-1}}.$$

On the other hand, if the H_2O_2 efflux cannot be neglected but k_{sink} is known, equation (37) yields:

$$\kappa_p S = \frac{1}{\frac{n_{cells}}{k_{cells} V_{medium}} - \frac{1}{k_{sink} V_{in}}}. \qquad (40)$$

Under the assumption that at the high extracellular H_2O_2 used k_{sink} is determined by the joint activities of GPx and Cat, Antunes and Cadenas [30] determined the permeability of the Jurkat T cell membrane as $\kappa_p = 2\times10^{-5}\ \mathrm{dm\,s^{-1}}$. Considering a mean Jurkat T cell volume $V =$ 6.6×10^{-13} dm^3, a surface area $S = 3.7\pm1.7\times10^{-8}$ dm^2, a cytoplasmic to cell volume fraction $f_{Cytoplasm} \approx 0.3$ [18] and a water content of 0.7 mL water/mL cell, one obtains a first order rate constant for H_2O_2 influx from the extracellular medium into the cytoplasm of:

$$k_{\mathrm{inf}} = \frac{\kappa_p \times S}{f_{water} \times f_{cytoplasm} \times V_{cell}} = \frac{2\times10^{-5}(\mathrm{dm\,s^{-1}})\times 3.7\times10^{-8}(\mathrm{dm^2})}{0.7\times0.3\times6.6\times10^{-13}(\mathrm{dm^3})} = 5.2\ \mathrm{s^{-1}}. \qquad (41)$$

The values of κ_p and k_{inf} for HeLa and MCF-7 cells can also be estimated under the same assumption about k_{sink} from data provided by references [36] and [37]. For HeLa cells, replacing $\frac{V_{medium}}{n_{cells}} k_{cells} = (0.50\pm0.017)\mathrm{mL/10^6 cells/min} = (8.3\pm0.28)\times10^{-12}\ \mathrm{dm^3 cell^{-1} s^{-1}}$ [36], $k_{sink} = k_{GPx} + k_{Cat} = 86.\ \mathrm{s^{-1}}$ (Sections 3.2.2.1 and 3.2.2.4) and $V_{in} = f_{water} \times V_{cytoplasm} = 0.7\times9.4\times10^{-13}\mathrm{dm^3} = 6.6\times10^{-13}\mathrm{dm^3}$ [25] into equations (40) and (39) yields

$$\kappa_p S = 9.7\times10^{-12}\ \mathrm{dm^3 cell^{-1} s^{-1}},$$
$$k_{inf} = 15.\ \mathrm{s^{-1}}.$$

Considering a surface area $S = 3.7\times10^{-8}\,\mathrm{dm}^2$ [25] one obtains $\kappa_p = 2.6\times10^{-4}\,\mathrm{dm\,s^{-1}}$.

Huang & Sikes [32] performed similar experiments for HeLa cells, which through similar calculations yield values in good agreement: $\kappa_p S = 5.1\times10^{-12}\,\mathrm{dm^3 cell^{-1} s^{-1}}$, $k_{inf} = 9.9\,\mathrm{s^{-1}}$, $\kappa_p = 1.4\times10^{-4}\,\mathrm{dm\,s^{-1}}$. We will thus consider the geometric mean $k_{inf} = 12.0\,\mathrm{s^{-1}}$ as reference for these cells.

For MCF-7 cells, from the values $\frac{V_{medium}}{n_{cells}} k_{cells} = (0.43 \pm 0.015)\mathrm{mL/10^6 cells/min} =$ $= (7.1 \pm 0.25)\times10^{-12}\,\mathrm{dm^3 cell^{-1} s^{-1}}$ [37], $k_{sink} = k_{GPx} + k_{Cat} = 14.\,\mathrm{s^{-1}}$ (Sections 3.2.2.1 and 3.2.2.4) and $V_{in} = f_{water} \times V_{cytoplasm} = 0.7\times1.0\times10^{-12}\,\mathrm{dm^3} = 7.3\times10^{-13}\,\mathrm{dm^3}$, $S = 7.6\times10^{-8}\,\mathrm{dm^2}$ [28] we obtain:

$$\kappa_p S = 1.4\times10^{-11}\,\mathrm{dm^3 cell^{-1} s^{-1}},$$
$$k_{inf} = 14.\,\mathrm{s^{-1}},$$
$$\kappa_p = 1.9\times10^{-4}\,\mathrm{dm\,s^{-1}}.$$

As we are unaware of k_{inf} estimations for any other human cells and the results above suggest that this parameter does not vary widely among cell types, we assume a $k_{inf} = 10.\,\mathrm{s^{-1}}$, the geometric mean of the values for the four cell types discussed above, for all other human cells in this work.

3.2.2. Alternative H_2O_2 sinks

The capacity of Jurkat T cells to clear cytoplasmic H_2O_2 through processes other than reduction by PrxI and PrxII is arguably the most uncertain parameter in the model. However, despite all the uncertainties one can ascertain that at low oxidative loads their aggregated contribution is much lower than the pseudo-first order rate constant for H_2O_2 reduction by Prx: $k_{Prx} = 4.\times10^7\,\mathrm{M^{-1} s^{-1}} \times (1.2\times10^{-4} + 4.6\times10^{-5})\mathrm{M} = 6.6\times10^3\,\mathrm{s^{-1}}$. (This calculation is based on the PrxI and PrxII concentrations estimated in Section 3.2.3.) At least five other processes that will be discussed in the subsections below may contribute for H_2O_2 clearance.

3.2.2.1. Reduction by glutathione peroxidase

At low to moderate H_2O_2 supply rates the kinetics of glutathione peroxidase 1 (GPx1) is well approximated by a simple mass action rate expression, as demonstrated by the following considerations. GPx1 follows ping-pong kinetics with rate expression [38]

$$v_{GPx1} = \frac{GPx1}{\frac{\Phi_1}{H_2O_2} + \frac{\Phi_2}{GSH}}.$$

This rate expression can be rearranged as

$$v_{GPx1} = \frac{\frac{GPx1}{\Phi_2} GSH \times H_2O_2}{\frac{\Phi_1}{\Phi_2} GSH + H_2O_2} ,$$

highlighting that the apparent Michaelis constant for H_2O_2 is given by $K_M^{App}(H_2O_2) = \frac{\Phi_1}{\Phi_2} GSH.$

Considering the value $\Phi_1 / \Phi_2 = 5.6 \times 10^{-3}$ determined for human GPx1 [39] and 3 mM GSH, one obtains $K_M^{App}(H_2O_2) = 17.\ \mu M$. Such a high intracellular H_2O_2 concentration is unlikely to be approached except under strong oxidative stress.

Antunes and Cadenas [30] determined the pseudo-first-order rate constant for this process in Jurkat T cells as 4.1 s^{-1}. From the activity per cell determinations for HeLa [36] and MCF-7 [37] — 3.18±0.45 mL/min/10^6 cells and 0.41±0.063 mL/min/10^6 cells, respectively — we estimate the pseudo-first-order rate constants 80. s^{-1} and 6.8 s^{-1}, considering the respective cell volumes 9.4×10^{-13} dm^3 [25] and 1.1×10^{-12} dm^3 [28], the cytoplasm volume fractions in Supplementary Table 4 and a cell water volume fraction of 0.7. Huang & Sikes [32] made similar determinations for HeLa cells, which through similar calculations yield a pseudo-first order rate constant of 67. s^{-1}. We will thus consider the geometric mean of these determinations — 73. s^{-1} — as reference for this parameter in HeLa cells.

3.2.2.2. Reduction by peroxiredoxin VI

Recent proteomic studies [12] point to a substantial concentration of the 1-Cys peroxiredoxin PrxVI in Jurkat T cells. Using the estimation method described in Section 3.1 we obtain:

$$PrxVI = \frac{\varphi_{\mathrm{PrxVI}} C_{tot}^{Jurkat}}{f_{cytoplasm} \frac{Laa_{\mathrm{PrxVI}}}{\overline{Laa}}} = \frac{6.4 \times 10^{-4} \times 7.0 \times 10^{-3} (\mathrm{M})}{0.3 \frac{224}{375}} = 25. \mu M$$

Considering a rate constant for H_2O_2 reduction of $k_{\mathrm{Ox,PrxVI}} =$ 3×10^6 $M^{-1}s^{-1}$ [40], this translates into a pseudo-first-order rate constant of $k_{\mathrm{Pr}\,xVI} = 3.0 \times 10^6 (\mathrm{M^{-1}s^{-1}}) \times 25. \times 10^{-6} (\mathrm{M}) = 75.\ \mathrm{s^{-1}}$ when all the protein is in thiolate form.

Upon reaction with H_2O_2 the active site thiolate is oxidized to a sulfenate whose reduction is dependent on glutathionylation by GSH-loaded glutathione S-transferase π [41,42], which is also abundant in Jurkat T cells [13]. At high H_2O_2 concentrations the rate-limiting step in the catalytic cycle is quite likely the reduction of the glutathionylated PrxVI molecule by another GSH

molecule [41]. Therefore, the contribution of PrxVI for H_2O_2 reduction will decrease when GSH is depleted.

3.2.2.3. Reduction by other thiol proteins

Hansen *et al*. [43] showed that the concentration of oxidizable protein thiols in human cell lines is in the order of 10 mM, which is comparable or higher than GSH concentrations. However, the use of diamide as oxidizing agent in this study may have caused a substantial over-estimation of the concentration of thiols that can potentially react with H_2O_2. This because diamide can oxidize thiols to $–RS^+$, which in turn readily react with other thiols.[44] In contrast, H_2O_2 can react at significant rates with thiolates but not with protonated thiols. Considering the mean protonation state under physiological pH, protein thiols are expected to react with H_2O_2 at rate constants ≈1 $M^{-1}s^{-1}$ or lower, similar to GSH [$k = 0.87$ $M^{-1}s^{-1}$ [45]]. Other than those in the active centers of peroxidases and peroxiredoxins, few protein thiols characterized to date have H_2O_2 reactivities in excess of 200 $M^{-1}s^{-1}$ [46,47]. Accordingly, a study analyzing the profile of thiol reactivities under more controlled conditions has shown that only a small fraction of the protein thiols are very reactive [48]. Likewise, redox proteomic studies of various cell types and organisms show few thiol proteins being oxidized in response to H_2O_2 boluses [49–51].

The considerations above and the fact that Prx are both very reactive and very abundant suggest that the overall contribution of protein thiols other than those in the active centers of peroxidases and peroxiredoxins for H_2O_2 clearance is modest. The following observations further support this notion. First, other very abundant proteins are not very H_2O_2-reactive. Only 6 cytoplasmic proteins are more abundant than PrxI + PrxII in Jurkat T cells [13,52], and among these, glyceraldehyde 3-phosphate dehydrogenase (GAPDH) has been flagged as the most prominent H_2O_2 target in a redox proteomic study,[49] indicating that the few more abundant proteins are less H_2O_2-reactive. Using the method described in Section 3.1 we estimate the concentration of GAPDH as ≈71 μM. This protein reacts with H_2O_2 with a rate constant 500 $M^{-1}s^{-1}$ [53,54]. Hence, the pseudo-first order rate constant for H_2O_2 reduction by this protein is a meager $k_{GAPDH} = 0.036 s^{-1}$.

Second, only two cytoplasmic proteins other than peroxiredoxins and Trx were detected as significantly reversibly oxidized in response to exposure of a HEK293T cell culture to a 50 μM H_2O_2 bolus for 5 min, in a redox proteomics study that was able to quantitatively assess the redox state of 404 thiol proteins.[51] Those oxidized proteins were GAPDH and proteasome subunit α type 1. Because the bolus was sufficient to extensively oxidize both PrxI and PrxII,[51] intracellular H_2O_2 concentrations should have increased very substantially during the pulse.

Third, although the redox-proteomic studies mentioned in the previous paragraph are biased towards abundant proteins it is unlikely that the set of less abundant H_2O_2-reactive proteins contributes significantly for H_2O_2 clearance. Indeed, even generously considering a total of 10 mM H_2O_2-oxidizable thiols at a 500 $M^{-1}s^{-1}$ mean reactivity would amount to a pseudo-first order rate constant $k_{RSH} = 5\,s^{-1}$ for H_2O_2 consumption, which is still less than other reductants discussed in this section.

Nevertheless, a quantitative analysis based on a mathematical model for H_2O_2 metabolism in Jurkat T cells [55] suggested that these cells contain an abundant pool (1 mM) of quite reactive (5×10^5 $M^{-1}s^{-1}$) protein thiols, amounting to a substantial $k_{RSH} = 5\times10^2\ s^{-1}$. More recently, a thorough analysis of the redox response of the 2-Cys peroxiredoxin Tpx1 from the fission yeast *Schizosaccharomyces pombe* to high concentrations of ectopic H_2O_2 also suggested the existence of a large (≈13 mM) pool of moderately H_2O_2-reactive (5×10^2 $M^{-1}s^{-1}$) protein thiols [56], yielding $k_{RSH} = 7.\,s^{-1}$. Nevertheless, none of these works identified the thiol proteins that might be oxidized at such rates. And in both cases reactivities and pool sizes were estimated quite indirectly by fitting complex kinetic models to experimentally determined time courses. Such estimates are very sensitive to the considerable uncertainties in both data and models. For instance, estimations in ref. [55] were based on experimental determinations of the redox potential of GSH that did not account for subcellular distribution of GSSG, which is now known to be concentrated in lysosomes and present at much lower concentrations in the cytoplasm [57]. In turn, in ref. [56] the observation of a bi-phasic response of Prx-SO_2^- and intracellular H_2O_2 concentrations in HEK293 to H_2O_2 boluses has been attributed to saturation of the peroxidases and a buffering effect from abundant protein thiols. But as we shall see in the main text and in Section 5 the same bi-phasic behavior is predicted by a model that neglects both these factors.

Finally, it should be noted that the pseudo-first order rate constants above represent upper estimates of the contribution of the protein thiols for H_2O_2 consumption, as they embody the assumption that the respective oxidized forms are readily reduced. Otherwise, this thiol pool will be progressively oxidized, and its contribution for eliminating H_2O_2 under sustained load (*i.e.,* at steady state) vanishes. We therefore neglected the contribution of non-peroxidase protein thiols for H_2O_2 clearance at steady state.

3.2.2.4. Dismutation by catalase

In Jurkat T cells, as in most human cells, all catalase is contained within peroxisomes. As consequence, the consumption of cytoplasmic H_2O_2 by catalase is rate limited by the permeation

of the peroxisomal membrane [30]. Taking this fact into account, Antunes and Cadenas [30] estimated the contribution of catalase for the clearance of cytoplasmic H_2O_2 as $k_{Cat} = 0.4\ s^{-1}$.

From the activity per cell determinations for HeLa [36] and MCF-7 [37] — 0.21±0.042 mL/min/10^6 cells and 0.42±0.061 mL/min/10^6 cells, respectively — we estimate the pseudo-first-order rate constants 5.3 s^{-1} and 7.0 s^{-1}, considering the respective cell volumes 9.4×10^{-13} dm^3 [25] and 1.1×10^{-12} dm^3 [28], the cytoplasm volume fractions in Supplementary Table 4 and a cell water volume fraction of 0.7. Huang & Sikes [32] made similar determinations for HeLa cells, which through similar calculations yield a pseudo-first-order rate constant of 1.7 s^{-1}. We will thus consider the geometric mean of these determinations — 3.0 s^{-1} — as reference for this parameter in HeLa cells.

3.2.2.5. Efflux

Because the plasma membrane is relatively permeable, part of the H_2O_2 can leave the cell. The rate constant for this process is $k_{effl} = k_{\mathrm{inf}} = 5.2\ s^{-1}$ as determined above.

Unlike all the other H_2O_2 clearance processes discussed above, catalase and the efflux are virtually non-saturable.[58,59] Therefore, at very high H_2O_2 supply rates able to saturate all other processes, cytoplasmic H_2O_2 will nearly equilibrate with the extracellular environment, because $k_{effl} \gg k_{Cat}$.

Altogether, the H_2O_2 clearance capacity through processes other than reduction by the typical 2-Cys peroxiredoxins adds up to:

$$k_{Alt} = (4.1 + 75. + 0.4 + 5.2)\,\mathrm{s}^{-1} = 85.\ \mathrm{s}^{-1}$$

at low oxidative loads, and to

$$k_{Alt} = (0.40 + 5.2)\ \mathrm{s}^{-1} = 5.6\ \mathrm{s}^{-1}$$

under strong enough oxidative loads to deplete GSH.

3.2.3. Peroxiredoxin concentrations and rate constants

We consider Prx total concentration as the sum of the concentration of PrxI (Prdx1, 199aa, 22.11 kDa) and PrxII (Prxd2, 196aa, 21.892 kDa) the two main 2-cys cytoplasmic peroxiredoxin.

Rhee *et al.* [60] determined the PrxI and PrxII contents in Jurkat T cells as $R_{\mathrm{PrxI/T}} = 2.7$ μg/mg of total soluble protein, and $R_{\mathrm{PrxII/T}} = 1.0$ μg/mg of soluble protein. Considering an average cell

609 volume of 6.6×10^{-13} dm^3 [18], an average protein content of 210 g/dm^3 [14] and the molecular
610 weights of PrxI (22,110 Da) and PrxII (21,892 Da) we obtain, the following concentrations:

611 $$PrxI = \frac{C_{tot}^{Jurkat} R_{\mathrm{PrxI/T}}}{f_{water} \times f_{cytoplasm} \times MW} = \frac{2.1\times10^{2}(\mathrm{g/dm^3})\times 2.7\times10^{-3}(\mathrm{g\ PrxII/g})}{0.7\times0.3\times2.21\times10^{4}(\mathrm{g/mol})} = 0.12\,\mathrm{mM}$$

612 $$PrxII = \frac{C_{tot}^{Jurkat} R_{\mathrm{PrxI/T}}}{f_{water} \times f_{cytoplasm} \times MW} = \frac{2.1\times10^{2}(\mathrm{g/dm^3})\times 1.0\times10^{-3}(\mathrm{g\ PrxII/g})}{0.7\times0.3\times2.19\times10^{4}(\mathrm{g/mol})} = 46.\,\mu\mathrm{M}$$

613 The rate constants for the oxidation of PrxII-S^- to PrxII-SO^- and of PrxII-SO^- to PrxII-SO_2^-, as well
614 as the rate constant for conversion of PrxII-SO^- to PrxII-SS, were experimentally determined as
615 $k_{Ox} = (1.0\pm0.1)\times10^{8}\,\mathrm{M^{-1}s^{-1}}$ [61] or $1.2\times10^{7}\,\mathrm{M^{-1}s^{-1}}$ [62], $k_{Sulf} = (1.2\pm0.2)\times10^{4}\,\mathrm{M^{-1}s^{-1}}$ [63,64],
616 $k_{Cond} = 1.7\pm0.3\,\mathrm{s^{-1}}$ [63] or $0.25\pm0.01\,\mathrm{s^{-1}}$ [65], respectively. The latter value for k_{Cond} was
617 determined based on the intrinsic Trp fluorescence method, which reflects the conformational
618 changes taking place over the PrxII redox cycle. One limitation of this method is that there is no
619 way to unequivocally attribute the observed slow component of the fluorescence variation to
620 the condensation step. This attribution is questioned by the observation that the low rate
621 constant inferred in ref. [65] leads to overestimation of the susceptibility of Prx2 to sulfinylation
622 relative to that observed *in vitro* [66]. For this reason, we adopted the value $k_{Cond} = 1.7\,\mathrm{s^{-1}}$ [63]
623 in the PTTRS model.

624 The rate constant for PrxII-SS reduction by human Trx1-S^- was determined as
625 $k_{Red} = (2.1\pm0.3)\times10^{5}\,\mathrm{M^{-1}s^{-1}}$ [61].

626 For Prx1 the following rate constants were experimentally determined:
627 $k_{Ox} = (3.8\pm0.15)\times10^{7}\,\mathrm{M^{-1}s^{-1}}$, $k_{Cond} = 9.0\pm0.2\,\mathrm{s^{-1}}$ [67]. The 36-fold higher k_{Cond} value for PrxI
628 than for PrxII is in keeping with the lower sensitivity of the former to hyperoxidation [68,69]. We
629 estimated the value of k_{Sulf} by fitting the following kinetic model

$$\frac{d\,H_2O_2}{dt} = k_{Ox}\,Prx\text{-}S^-\,H_2O_2 - k_{Sulf}\,Prx\text{-}SO^-\,H_2O_2$$

$$\frac{d\,Prx\text{-}S^-}{dt} = k_{Red}\,Trx\text{-}S^-\,Prx\text{-}SS - k_{Ox}\,Prx\text{-}S^-\,H_2O_2$$

$$\frac{d\,Prx\text{-}SO^-}{dt} = k_{Ox}\,Prx\text{-}S^-\,H_2O_2 + k_{Srx}\,Prx\text{-}SO_2^- - k_{Sulf}\,Prx\text{-}SO^-\,H_2O_2 - k_{Cond}\,Prx\text{-}SO^-$$

630

$$\frac{d\,Prx\text{-}SO_2^-}{dt} = k_{Sulf}\,Prx\text{-}SO^-\,H_2O_2$$

$$\frac{d\,Prx\text{-}SS}{dt} = k_{Cond}\,Prx\text{-}SO^- - k_{Red}\,Trx\text{-}S^-\,Prx\text{-}SS$$

$$\frac{d\,NADPH}{dt} = -k_{Red}\,Trx\text{-}S^-\,Prx\text{-}SS$$

631 to several independent NADPH consumption time series from coupled Prx1/Trx/TrxR assays. Namely, the first 150 s of the time courses reported in Fig. 1A of ref. [70] for 100 μM and 200 μM H_2O_2, after subtracting the basal NADPH consumption rate as computed from the time course for $[H_2O_2]$= 0. And the first 110 s of the time course reported in Figure 6A of ref. [68], after subtracting the basal NADPH consumption rate as computed from the late phase (t > 120 s) of the curve.

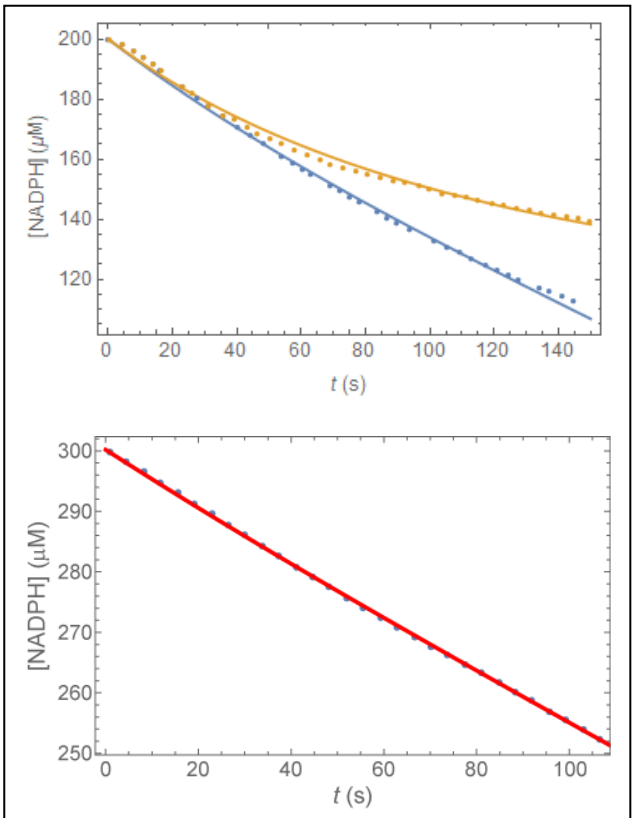

Supplementary Figure 4. Fit to the time courses of NADPH consumption reported in Figure 1A of ref. [70] ***(top) and Figure 6A of ref.*** [68] ***(bottom).*** *Dots, sampled points; lines, best fit curves.*

The parameters k_{Ox} and k_{Cond} were fixed at the values indicated above, whereas k_{Sulf} and k_{Red} were left as adjustable parameters. The fits were made using *Mathematica*™ v 11 NonlinearModelFit function with default settings.

650 The best fit for the first dataset was obtained for $k_{Sulf} = (1.61 \pm 0.026)\times 10^3\ \mathrm{M^{-1}s^{-1}}$,

651 $k_{Red} = (1.43 \pm 0.012)\times 10^5\ \mathrm{M^{-1}s^{-1}}$ (Adjusted R^2= 0.99992, Supplementary Figure 4, top), whereas

652 the best fit for the second one was for $k_{Sulf} = (1.1 \pm 0.11)\times 10^3\ \mathrm{M^{-1}s^{-1}}$,

653 $k_{Red} = (1.11 \pm 0.010)\times 10^5\ \mathrm{M^{-1}s^{-1}}$ (Adjusted R^2= 0.999999, Supplementary Figure 4, bottom).

These values for k_{Sulf} of PrxI are in close agreement, prompting us to adopt the compromise value $k_{Sulf} = 1.3\times10^{3}\,\mathrm{M^{-1}s^{-1}}$ in subsequent analyses. In turn, this value is one order of magnitude lower than that determined for PrxII, which indicates that the lower sensitivity of PrxI to hyperoxidation [68,69] is due to both a faster condensation step and less favorable sulfinylation. This is in contrast to PrxIII, whose increased sulfinylation sensitivity relative to PrxII is entirely due to a lower value of k_{Cond}, the value of k_{Sulf} being virtually identical to that for PrxII [63].

The best-fit values for the k_{Red} of PrxI determined above are close to each other and comparable to that reported for PrxII [61]. For this reason and because we could not determine the origin of the Trx used in the experiments in refs. [68,70] we assumed that the value of k_{Red} for PrxI is the same as for PrxII.

For simplicity, in the design space analysis we considered a single typical 2-Cys peroxiredoxin with $k_{Ox} = 4.\times10^{7}\,\mathrm{M^{-1}s^{-1}}$, corresponding to the geometric mean of the values determined for PrxI and PrxII and k_{Cond}, k_{Sulf} values that are concentration-weighted averages of the values for PrxI and PrxII:

$$k^{*}_{Cond} = f_{PrxI}\times k^{\mathrm{PrxI}}_{Cond} + f_{PrxII}\times k^{\mathrm{PrxII}}_{Cond} = 0.72\times9.0\,\mathrm{s^{-1}} + 0.28\times0.65\,\mathrm{s^{-1}} = 6.7\ \mathrm{s^{-1}}$$

$$k^{*}_{Sulf} = f_{PrxI}\times k^{\mathrm{PrxI}}_{Sulf} + f_{PrxII}\times k^{\mathrm{PrxII}}_{Sulf} = 0.72\times1.3\times10^{3}\,\mathrm{M^{-1}s^{-1}} + 0.28\times1.2\times10^{4}\,\mathrm{M^{-1}s^{-1}} = 4.3\times10^{3}\,\mathrm{M^{-1}s^{-1}}.$$

The value $k^{\mathrm{PrxII}}_{Cond} = 0.65\,\mathrm{s^{-1}}$ is the geometric mean of those determined in refs. [63,65].

3.2.4. Peroxiredoxin glutathionylation

Both PrxI [71] and PrxII [72] can be glutathionylated and Grx1 and/or Srx [71,72] catalyze their deglutathionylation. These findings raise the question of the overall importance of these processes for the dynamics of the PTTRS, which we discuss below.

Peskin *et al.* [72] determined a rate constant $k_{Glut} = 500\,\mathrm{M^{-1}s^{-1}}$ for PrxII-SO^{-} glutathionylation and found that deglutathionylation was fast in presence of Grx1+GSH, such that glutathionylated PrxII (PrxII-SSG) could only be detected in erythrocytes from Grx1-knockout mice after a peroxide challenge. In turn, although GSH was also able to reduce PrxII-SS, this process is relatively slow.[72]

The following considerations help evaluating the extent to which Prx-SO^{-} de/glutathionylation contributes to inhibit hyperoxidation and for Prx's catalytic redox cycle. Once a Prx-SO^{-} forms,

its fate is determined by a competition between sulfinylation, glutathionylation, and condensation. At physiological H_2O_2 and GSH concentrations both glutathionylation and condensation are much faster than sulfinylation. But for glutathionylation to strongly inhibit sulfinylation it must be faster than condensation, because otherwise it is the latter that will most strongly compete with sulfinylation. In erythrocytes, where PrxII is by far the dominant Prx and the GSH concentration is ≈3 mM, the pseudo-first order rate constant for glutathionylation is 1.5 s^{-1}. This is comparable to the $k_{Cond} = 1.7\ s^{-1}$ determined by the same group, and therefore in erythrocytes PrxII-SO^- de/glutathionylation can almost double the overall redox turnover of PrxII and inhibit is hyperoxidation by up to ≈50%. (However, GSH may be depleted at the oxidative loads where this inhibition might otherwise be most relevant.) Prx-SO^- reduction by GSH is thus relevant in erythrocytes, where PrxII is the dominant Prx.

In turn, the following observations indicate that de/glutathionylation plays only a minor role in PrxI's redox cycle and protection against hyperoxidation. Park *et al.* [71] determined PrxI-SSG deglutathionylation rates of ≈20 nM s^{-1} with 22 μM PrxI-SSG and 1 μM Grx1 or Srx. This Grx1 and Srx concentration is similar to the cytoplasmic concentrations in the A549 and HeLa cell lines used by these authors, from which we can roughly infer a deglutathionylation pseudo-first order rate constant (k_{Deglut}) in the order of 10^{-3} s^{-1} in these cells. In order to examine the consequences of such a k_{Deglut} consider that the PrxI-SO^- production rate is $v^+_{\text{PrxI-SS}} = k_{Ox} \times PrxI\text{-}S^- \times H_2O_2$. If glutathionylation is the dominant process consuming PrxI-SO^- then the rate of PrxI-SSG production will also approach $v^+_{\text{PrxI-SS}}$, and the ratio between the concentrations of PrxI-SSG and Prx-S^- at steady state will be approximately:

$$\frac{PrxI\text{-}SSG}{PrxI\text{-}S^-} = \frac{k_{Ox}}{k_{Deglut}} H_2O_2 = \frac{3.8\times10^7\ \text{M}^{-1}\text{s}^{-1}}{10^{-3}\ \text{s}^{-1}} H_2O_2 = 3.8\times10^{10}\ \text{M}^{-1} H_2O_2 .$$

Therefore, PrxI would be strongly glutathionylated even at H_2O_2 concentrations as low as 0.1 nM. Similar arguments apply with respect to Prx-SS glutathionylation. However, Park et al (2009) needed to use an enrichment approach to detect PrxI-SSG even in cells exposed to 10 μM H_2O_2. This shows that glutathionylation/deglutathionylation cannot significantly contribute for PrxI's redox turnover or strongly inhibit PrxI sulfinylation. This low contribution may have the following two explanations. First, because k_{Cond} for PrxI-SO^- is substantially higher than for PrxII-SO^- (Section 3.2.3) k_{Glut} for PrxI ought to be comparably higher than that for PrxII-SO^- for glutathionylation to have a comparable contribution for the redox turnover of the former Prx.

Second, the estimated k_{Deglut} is at least 100-fold lower than the pseudo-first order rate constant for PrxI-SS reduction by a similar (1 μM) Trx1-S^- concentration (>0.1 s^{-1} as per Section 3.2.3). Moreover, Grx1 and Srx together are over one order of magnitude less abundant in A549 and HeLa cells than Trx1 (Supplementary Table 6), and they are also substantially less abundant than Trx1 in all other human cell lines examined in the present work.

As further evidence for a low contribution of GSH for the Prx redox turnover, even a strong GSH depletion failed to increase the fraction of PrxII-SS in HeLa and A549 cells.[74] Because PrxI is the main H_2O_2 reductant in these cells (Supplementary Table 6), if GSH contributed substantially its redox turnover its depletion would translate on a significant elevation of the cytoplasmic H_2O_2 concentration, resulting in increased PrxII dimerization.

Because in all these cell lines examined in this work PrxI is several-fold more abundant than PrxII, the overall contribution of de/glutathionylation for the redox turnover and sulfinylation inhibition can be neglected in the coarse-grained single-Prx model.

On the other hand, it also follows from the estimates above and from the estimated activities of PrxVI and GPx1 (Section 3.2.2 and Supplementary Table 6) that PrxII should be the main driver of GSH oxidation in all the examined human cells.

3.2.5. Sulfiredoxin concentration and activity

The reduction of Prx-SO_2^- to Prx-SO^- requires ATP and a reductant and is catalyzed by sulfiredoxin. The rate-limiting step in this process is the formation of a thiosulfinate intermediate [75–78] (Srx-Prx) whose existence for the human enzyme has been confirmed [79]. The resolution of this complex generates an intramolecular disulfide bond Srx-SS, that is then reduced by Trx1-SH in the case of the yeast [80] or presumably GSH in the case of human Srx [81]. Human Srx has a catalytic constant of 3.0×10^{-3} s^{-1} for PrxI-SO_2^-, and $K_M(\mathrm{ATP}) =$ 30 μM.[82] Therefore, the enzyme is normally

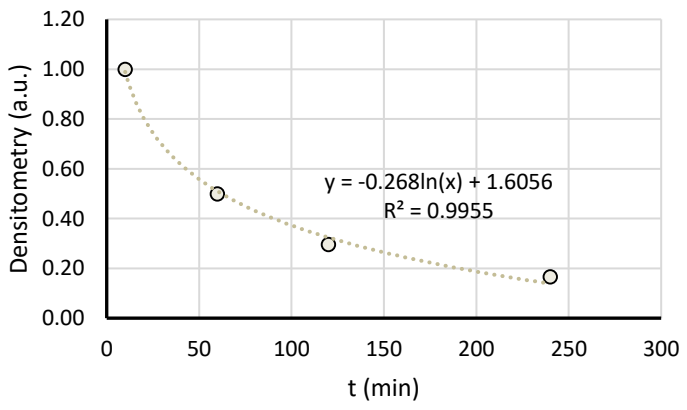

Supplementary Figure 5. Fit of the time course of PrxI-SO_2^- reduction in A549 cells previously exposed to 250 μM H_2O_2 *from the immunoblot images for "Control RNA","α-PrxSO_2" panel in Figure 8 from ref.* [82].

745 saturated with ATP. The $K_M(GSH)$ is unknown but presumed to be much lower than
746 physiological GSH concentrations. [81] The Michaelis constant for Prx-SO_2^- also has not been
747 characterized, which prevents a detailed modeling of this process' kinetics. On the other hand,
748 we were able to estimate a pseudo-first-order rate constant for PrxI-SO_2^- reduction in A549 cells
749 previously exposed to 250 μM H_2O_2 from the immunoblot images for "Control RNA","α-PrxSO_2"
750 panel in Figure 8 from ref. [82]. Densitometry analysis of the image reveals a mono-exponential
751 decay of the concentration of PrxI-SO_2^-, which is well fitted (R^2=0.996) by a
752 $k_{Srx}^{A549} = 4.45\times10^{-3}\,\mathrm{s}^{-1}$ (Supplementary Figure 5). From the data in the Proteomaps database,
753 using the method described in Section 3.1, we estimated the concentration of Srx in A549 and
754 in Jurkat T cells as:

755
$$Srx(\mathrm{A549}) = \frac{\varphi_{\mathrm{Srx}}^{\mathrm{A549}}\, C_{tot}}{f_{cytoplasm}\,\dfrac{Laa_{\mathrm{Srx}}}{\overline{Laa}}} = \frac{39.76\times10^{-6}\times7.0\times10^{-3}(\mathrm{M})}{0.7\,\dfrac{145}{375}} = 1.0\ \mu\mathrm{M}$$

$$Srx(\mathrm{Jurkat}) = \frac{1.9\cdot10^{-6}\times7.0\times10^{-3}(\mathrm{M})}{0.28\,\dfrac{145}{375}} = 0.13\ \mu\mathrm{M}.$$

756 Therefore, assuming that the pseudo-first-order rate constant is proportional to the
757 concentration of Srx in each cell, we obtained:

758
$$k_{\mathrm{Srx}} = \frac{0.13\,\mu\mathrm{M}}{1.0\ \mu\mathrm{M}}\,4.45\times10^{-3}\,\mathrm{s}^{-1} = 5.8\times10^{-4}\,\mathrm{s}^{-1}\ .$$

759 The slower reduction of Prx-SO_2^- in HeLa than in A549 cells observed in ref. [83] is consistent
760 with the 11-fold lower Srx concentration in those cells as per the proteomic dataset (Section
761 3.5).

762 Although PrxII-SO_2^- is known to be more rapidly reduced than PrxI-SO_2^- in cells,[84] there is
763 insufficient information in the literature to determine k_{Srx} for the former Prx. However, because
764 PrxI is the predominant Prx in all the cell lines the assumption of similar k_{Srx} for both Prx does
765 not strongly affect the results.

766 3.2.6. Thioredoxin concentration

767 Trx1 is a predominantly cytoplasmic protein [22] that can also be found in the nucleus
768 [29,85]. Assuming a fully cytoplasmic localization, the cytoplasmic concentration of Trx1 (105aa)
769 estimated using the method described above is:

$$Trx1 = \frac{\varphi_{Trx}\, C_{tot}^{Jurkat}}{f_{cytoplasm}\, \frac{Laa_{Trx}}{\overline{Laa}}} = \frac{4.3\times10^{-4}\times 7.0\times10^{-3}(\mathrm{M})}{0.3\frac{105}{375}} = 36.\,\mu\mathrm{M}\ .$$

The quantitative proteomics data for the other *nucleated* human cells considered in this work yield cytoplasmic concentrations in the range 17. – 69. μM (Supplementary Table 6). These values are in the range of determinations obtained by other methods (Supplementary Table 5), including a recent one to determine redox-active Trx1 [86]. The widely held view that Trx1 concentrations in human cells are in the μM or sub-μM range may have been biased by early determinations for erythrocytes, which are exceptionally Trx1-poor.

However, not all the Trx1 is necessarily available to reduce Prx-SS. Trx1 can covalently bind numerous proteins [87], including very abundant actin [88]. Thioredoxin-interacting protein (TXNIP), which inhibits Trx1's redox cycling [89], is much less abundant than Trx1 in the proteomic datasets under consideration, though. Trx1 also extensively translocates to the nucleus under some stress conditions,[85,90] including exposure of cells to extracellular H_2O_2 [91].

Supplementary Table 5: Cytoplasmic thioredoxin concentrations estimated from non-proteomic methods. *Cytoplasmic concentrations were estimated from the values provided in the cited references by assuming that the cytoplasm accounts for 50% of the cell volume (except erythrocytes, 100%), a protein density of 0.2 g/mL cell volume [15,16] and a cell water content of 70% by volume. Although the methods used do not discriminate between Trx1 and Trx2, the latter accounts for <6% of the total Trx contents in cells, according to the quantitative proteomics determinations. Note the very good agreement between the value for K562 cells in this table and that in Supplementary Table 6.*

Cell type	Concentration (μM)	Method	Ref.
Peripheral blood mononuclear cells	86.	Fluorescein isothiocyanate-labeled insulin	[86]
Lymphocytes	53.	Fluorescein isothiocyanate-labeled insulin	[86]
Ramos	21.	Fluorescein isothiocyanate-labeled insulin	[86]
U937	1.1×10^2	Fluorescein isothiocyanate-labeled insulin	[86]
K562	22.	Fluorescein isothiocyanate-labeled insulin	[86]
Fibroblasts	18.	Immunochemical	[92]
Erythrocytes	0.56	Immunochemical	[93]

3.2.7. Thioredoxin oxidation

Besides the reduction of typical 2-Cys peroxiredoxins other processes also contribute for Trx1 oxidation. Prominent among these are the reduction of ribonucleotides to deoxyribonucleotides catalyzed by ribonucleotide reductase, and the reduction of protein

disulfides. The former process is essential for DNA replication. Replication of the 3.0×10^9 base pairs of the human genome during the ≈12 h duration of S phase in a Jurkat T cell [94] implies an average Trx1 oxidation rate of ≈2 μMs^{-1}. In turn, an upper estimate of the mean Trx1 oxidation rate imposed by a massive oxidation of the protein thiols can be derived from the following data. Hansen et al. [43] determined that 3.6 protein thiols (PSH) per 1000 aminoacyl residues (aa) were oxidized to disulfides upon treatment of HEK293 cells with excess diamide. Reduction of the protein disulfides was essentially complete 20 minutes after the treatment. Considering that cells contain $\approx5\times10^6$ proteins/fL cell water [14], and an average human protein contains 375 aa, the concentration of protein thiols oxidized to disulfides by this extreme treatment can be roughly estimated as (5×10^6 proteins/10^{-15} L)×(375 aa/protein)×(3.6 PSH/1000 aa) / (6.0×10^{23} PSH/mol) = 11. mM. Therefore, the mean rate of PSS reduction was (11. mM/2) / 1200 s = 4.6 $\mu M\ s^{-1}$. Values for HeLa cells are in the same range [43]. However, only a small fraction of the oxidized PSH reside in the cytoplasm [43]. These mean rates are much lower than the V_{Max}(TrxR)= 180 μMs^{-1}, estimated in Section 3.2.8. Therefore, they are insufficient to sustain a strong Trx1 oxidation, although peak rates may be much higher. In turn, the 166 μM Prx if fully oxidized to Prx-SS can drive Trx1-S^- oxidation at a maximal rate of $2.1\times10^5(M^{-1}s^{-1})\times1.7\times10^{-4}(M\ \text{Prx-SS})\times1.2\times10^{-5}(M\ \text{Trx-S}^-)=0.43\,mMs^{-1}$, and can thus in principle cause the complete Trx1-S^- oxidation.

3.2.8. Thioredoxin reductase concentration and activity

Low et al. [95] determined the activity of Trx reductase in Jurkat T cells for 5-(3-Carboxy-4-nitrophenyl)disulfanyl-2-nitrobenzoic acid (DTNB) as substrate as 1.63±0.35 nmol/10^6 cells/min, at 37 °C, pH 7.4. We estimated [31] that the activity with human Trx1 as substrate is 1.3-fold higher. Therefore, considering a mean Jurkat T cell volume of 6.6×10^{-13} dm^3 and a cytoplasmic fraction of 0.3 [18] one can estimate:

$$V_{Max,TrxR}=1.3\frac{1.6\times10^{-9}(\text{mol})}{0.3\times6.6\times10^{-9}(\text{dm}^3)\times60(\text{s/min})}=0.18\,\text{mMs}^{-1}\ .$$

This is the value we will use as reference in our modelling.

A partly independent estimate follows from the mass fraction of thioredoxin reductase (TxnRd1, Laa= 649) ($\varphi_{\text{TrxR}}=4.04\times10^{-4}$) obtained from the proteomic dataset from Geiger *et al.* [12] and as reported in the Proteomaps database [13]. Applying the method described in Section 3.1, this corresponds to the following concentration:

825 $$TrxR = \frac{\varphi_{\mathrm{TrxR}} \cdot C_{tot}}{f_{cytoplasm} \frac{Laa_{\mathrm{TrxR}}}{\overline{Laa}}} = \frac{4.0\times10^{-4} \times 7.0\times10^{-3}(\mathrm{M})}{0.3\frac{649}{375}} = 5.3\,\mu\mathrm{M}$$

826 Considering the $k_{cat} = 76.3\,\mathrm{s}^{-1}$ estimated in ref. [31] this concentration yields
827 $V_{Max,TrxR} = 0.45\,\mathrm{mM\,s}^{-1}$, in reasonable agreement with the previous estimate.

828 TrxR follows a ping-pong catalytic mechanism [96,97] whose kinetics can be described by:

829 $$v = \frac{V_{Max,TrxR}}{1 + \frac{K_{M,TrxR,NADPH}}{NADPH} + \frac{K_{M,TrxR,TrxSS}}{TrxSS}}$$

830 We considered $K_{M,TrxR,TrxSS} = 1.8\,\mu\mathrm{M}$ [98]. The low $K_{M,TrxR,NADPH} = 6.0\,\mu\mathrm{M}$ [99] implies that
831 except under strong and prolonged oxidative stress NADPH concentrations can be considered
832 saturating. This should be especially true for tumor cell lines, which tend to over-express the
833 pentose phosphates pathway [100] and thus have a large capacity to reduce $NADP^+$ to NADPH.
834 Therefore, we assume that TrxR is saturated with NADPH and approximate its kinetics as

835 $$v = \frac{V_{Max,TrxR}\, TrxSS}{TrxSS + K_{M,TrxR,TrxSS}}\,.$$

836 ### 3.2.9. $NADP^+$ reduction capacity

837 The oxidative branch of the pentose phosphate pathway (oxPPP) is the main supplier of
838 reducing equivalents for $NADP^+$ reduction in the cytoplasm of most cells, with the oxidation of
839 methylene tetrahydrofolate to 10-formyl-tetrahydrofolate sometimes contributing significantly
840 (≈20%).[101] The flux over oxPPP is normally limited at the first step, catalyzed by by glucose
841 6-phosphate (G6P) dehydrogenase (G6PD). Ursini *et al.* [102] determined a G6PD activity of 0.23
842 μmol NADPH / mg protein / min in untreated proliferating Jurkat T cells, which transiently
843 increased to 0.51 μmol NADPH / mg protein / min within 6 h after cells were treated with a 200
844 μM H_2O_2 bolus for 30 min. Similar results were found for HepG2 and Hep3B cells [102].
845 Considering a mean Jurkat T protein contents of 210 g dm^{-3} (Section 3.1) and a cytoplasmic
846 fraction of 0.3 [18], and noting that each G6P molecule entering the oxidative branch of the PPP
847 permits the reduction of 2 $NADP^+$ molecules, one finds the following $NADP^+$ reduction capacity
848 of the oxPPP:

849 $$V_{PPP} = 2 \times \frac{2.3\times10^{-4}(\mathrm{mol\,g^{-1}min^{-1}}) \times 2.1\times10^{2}(\mathrm{g\,dm^{-3}})}{0.3\times 60\,\mathrm{s}} = 5.4\,\mathrm{mM\,s^{-1}}$$

for untreated cells, and 12. mM s^{-1} for the treated ones. In turn, from the cytoplasmic G6PD concentration estimated from the proteomic data in ref. [12] through the method described in Section 3.1 (9.2 μM), one can estimate an upper limit for this rate by considering a 690 s^{-1} catalytic constant for G6PD [103]. The value obtained, 13. mM s^{-1}, is in good agreement with the rate above.

However, the activity of G6PD is in substantial excess of cells' capacity to supply G6P [104]. Indeed, at physiological plasma glucose concentrations, in the absence of oxidative stress, Jurkat T cells import glucose at a rate of just ≈150 μM s^{-1}.[105] Under oxidative stress conditions cells can not only direct most of the G6P through the oxPPP but also recycle intermediates from upper glycolysis into the oxPPP.[106] Upon this metabolic reconfiguration, the oxPPP could reduce up to 12 $NADP^+$ per G6P consumed, yielding a maximum ≈1.8 mM s^{-1} NADPH production. This is a theoretical upper limit corresponding to the full oxidation of glucose with a net expenditure of 1 ATP/glucose. As discussed in detail in refs. [104,107], the "excess" G6PD activity is instrumental in avoiding NADPH depletion and ensuring a fast response to changes in the demand for reducing equivalents.

In turn, actual NADPH consumption rates are much lower than the production capacities discussed in the previous paragraph. The cytoplasmic consumption of NADPH in proliferating HEK293T and other cell lines is ≈8 μM s^{-1}.[101] Most (>80%) of this flux is devoted to biosynthesis, and in cells that were growth arrested by exposure to a 150 μM H_2O_2 bolus the mean NADPH consumption over 5h actually decreases to ≈5 μM s^{-1}.[101] (Though substantially higher instantaneous fluxes may have been attained immediately after treatment.)

Altogether, these considerations indicate that cells have the means to avoid sustained strong NADPH depletion under low to moderate oxidative stress. Indeed, Kuehne *et al.* [106] found that exposure of fibroblasts to a 500 μM H_2O_2 bolus caused just ≈30% NADPH depletion.

3.3. Estimations for other human cells

The concentrations of the relevant proteins in the other cell lines considered in the work, were computed through the mass fraction method described in Section 3.1, using the data generated by Geiger *et al.* (2012) [12]. We have also used the dataset from Wiśniewski *et al.* [21] for human hepatocytes and HepG2 cells.

The condensation rate constants for the peroxiredoxin and the pseudo-first order rate constants for Srx were estimated through the methods described for Jurkat T cells in Sections 3.2.1 and 3.2.4, respectively.

882 The V_{Max} for TrxR was estimated from the concentration of this enzyme by considering the
883 catalytic constant $k_{cat} = 76.3\,\mathrm{s}^{-1}$ estimated in ref. [31].

884 As discussed in Section 3.2.1, we were able to estimate k_{inf} for Jurkat T, HeLa, MCF-7 cells and
885 erythrocytes but are unaware of data that permit this estimation for any other human cells.
886 However, the estimates for these cells suggest that this parameter does not vary widely among
887 cell types. Therefore we assume $k_{inf} = 10.\,\mathrm{s}^{-1}$, the geometric mean of the values for the four cell
888 mentioned above, for all other human cells examined.

889 The sum of the contributions from PrxVI, GPx1, catalase and efflux were used as an
890 approximation of the cytoplasm's capacity to scavenge H_2O_2 through processes other than
891 reduction by PrxI and PrxII.

892 The contribution from PrxVI activity for all other cell lines was estimated as described in Section
893 3.2.2.2 for Jurkat T cells.

894 The GPx1 activities in Jurkat T, HeLa, MCF-7 cells and erythrocytes were obtained from the
895 literature (Section 3.2.2.1). For all the other human cells the GPx1 activity was assumed as
896 proportional to GPx1 protein mass as given in the Proteomaps database [13] for the dataset
897 from ref. [12] or from the dataset in ref. [21] and the same proportionality constant as for Jurkat
898 T cells. Therefore, drawing on the estimate in Section 3.2.2.1, and further assuming that the
899 total protein concentration is essentially invariant among cell types (*i.e.*, $C_{tot}^{Cell\,type} = C_{tot}^{Jurkat}$), the
900 estimated value is given by:

901 $$k_{GPx}^{Cell\,type} = \frac{k_{GPx}^{Jurkat}}{\varphi_{GPx}^{Jurkat}} \varphi_{GPx}^{Cell\,type} = \frac{4.1\,\mathrm{s}^{-1}}{32.17\ \mathrm{ppm}} \varphi_{GPx}^{Cell\,type}\ \mathrm{s}^{-1} \quad (42)$$

902 In all cell lines examined catalase is confined to peroxisomes. As a consequence, its action on
903 cytoplasmic H_2O_2 is limited by the membrane permeation step. The peroxisomal-membrane-
904 limited Cat activities in Jurkat T, HeLa, MCF-7 cells and erythrocytes were obtained from the
905 literature (Section 3.2.2.4). For simplicity we assumed that all other cell lines show the same
906 proportionality between catalase abundance and effective pseudo-first-order rate constant for
907 consumption of cytoplasmic H_2O_2 as Jurkat T cells. Therefore, drawing on the estimate in Section
908 3.2.2.4, and further assuming that the total protein concentration is essentially invariant among
909 cell types (*i.e.*, $C_{tot}^{Cell\,type} = C_{tot}^{Jurkat}$), the estimated value is given by:

910 $$k_{Cat}^{Cell\ type} = \frac{\varphi_{Cat}^{Cell\ type}}{\varphi_{Cat}^{Jurkat}} k_{Cat}^{Jurkat} = \frac{0.4\ \mathrm{s}^{-1}}{246.98\ \mathrm{ppm}} \varphi_{Cat}^{Cell\ type}\ \mathrm{s}^{-1}. \quad (43)$$

911 Although this is admittedly a rough estimate of $k_{Cat}^{Cell\ type}$, its uncertainty is a minor concern
912 because $k_{Cat}^{Cell\ type}$ typically has a minor contribution to k_{Alt}.

913 3.4. Estimations for *Saccharomyces cerevisiae*

914 3.4.1. H_2O_2 Permeability

915 The permeability constant and pseudo-first order rate constant for permeation to/from
916 the cytoplasm were estimated from data in figure 1 of ref. [108], which shows the time course
917 of H_2O_2 consumption by a yeast liquid culture with OD 0.5 (7x10^6 cells/ml). By fitting an
918 exponential decay to this data (Supplementary Figure 6) we first find the pseudo-first order rate
919 constant for the consumption of extracellular H_2O_2: $k_{\mathrm{cells}} = (1.33 \pm 0.08) \times 10^{-3}\ \mathrm{s}^{-1}$. From this
920 value and considering the average cell surface area for yeast as 133±9.5 µm^2 [109] we then
921 obtain the permeability coefficient:

922 $$\kappa_{perm} = \frac{1.33 \times 10^{-3}\ (\mathrm{s}^{-1})}{7 \times 10^{9}\ (\mathrm{cells\ dm}^{-3}) \times 1.33 \times 10^{-8} (\mathrm{dm}^2)} = 1.43 \times 10^{-5}\ \mathrm{dm\ s}^{-1}$$

923 Considering that the water volume fraction of *S. cerevisiae* cells is $f_{water} = 0.68$ [110], that the
924 cell volume is 42 µm^3 [111] and that the volume ratio of cytoplasm to full cell is $f_{cytoplasm} = 0.70$
925 [112], we obtain the cytoplasmic water volume:

926 $$V_{cytoplasm} = f_{cytoplasm} f_{water} V_{yeast\ cell} = 0.70 \times 0.68 \times 4.2 \times 10^{-14}\ \mathrm{dm}^3 = 2.0 \times 10^{-14}\ \mathrm{dm}^3.$$

927 From this we finally obtain the following pseudo-first order rate constant for permeation:

928 $$k_{\mathrm{inf}} = \frac{1.43 \times 10^{-5} (\mathrm{dm\ s}^{-1}) \times 1.33 \times 10^{-8} (\mathrm{dm}^2)}{2.0 \times 10^{-14} (\mathrm{dm}^3)} = 9.5\ \mathrm{s}^{-1},$$

929 which is similar to that for human cells.

930 3.4.2. Alternative H_2O_2 sinks

931 The cytoplasm of *S. cerevisiae* contains catalase T (CTT1) and alkyl hydroperoxide
932 reductase (Ahp1), an atypical 2-Cys peroxiredoxin. Furthermore, cytochrome c peroxidase (CcP)
933 in the mitochondrial intermembrane space may also contribute to clear cytoplasmic H_2O_2, as the
934 latter is expected to freely cross the mitochondrial outer membrane. The contributions of these
935 enzymes for cytoplasmic H_2O_2 clearance were estimated as follows.

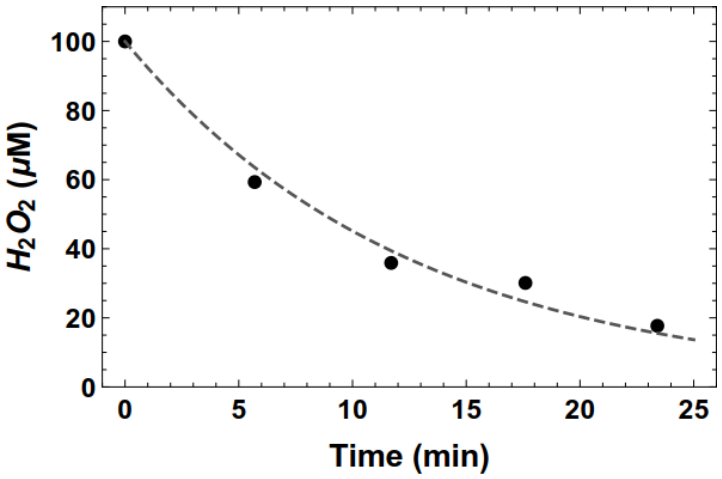

Supplementary Figure 6. Fit of the time course of H_2O_2 consumption in S. cerevisiae cells culture exposed to a 100 μM H_2O_2 bolus. *Black dots, experimental data; broken line, best fit to the function H_2O_2 = 100 exp(-$k_{consumption}$ t). Best fit parameter was $k_{consumption}$= (1.33±0.08)×10^{-3} s^{-1}. The fitting was done using the function NonLinearModelFit in Mathematica 10.3.*

3.4.2.1. Cytochrome c peroxidase

From the molecule counts per cell in ref. [113], and assuming that H_2O_2 can freely permeate between cytosol and the mitochondrial intermembrane space and that the volume of the latter compartment is negligible, the estimated concentration of CcP is:

$$CcP = \frac{\frac{N_{CcP}}{N_A}}{V_{cytoplasm}} = \frac{\frac{6725\ \text{molecule}}{6.02\times10^{23}\ \text{molecule mol}^{-1}}}{2.0\times10^{-14}\ \text{dm}^3} = 0.54\ \mu\text{M}$$

Considering the rate constant for H_2O_2 reduction by CcP (3.9x10^7 M^{-1}s^{-1} [114]) one obtains:

$$k_{CcP} = 0.54\times10^{-6}\,(\text{M})\times3.9\times10^{7}\,(\text{M}^{-1}\text{s}^{-1}) = 21.\,\text{s}^{-1}\ .$$

3.4.2.2. Catalase T

Branco *et al.* [108] determined a $A_{Cat} = 1.1\times10^{-2}\ \text{dm}^3\text{g}^{-1}\text{s}^{-1}$ catalase activity in extracts from yeast growing in exponential phase, which is abolished in *ctt1*Δ mutants. Considering $m_{prot} = 5.7\ \text{pg}$ as the protein content of a yeast cell [115], this activity translates into:

$$k_{CTT1} = \frac{A_{cat}\,m_{prot}}{V_{cytoplasm}} = \frac{1.1\times10^{-2}\,(\text{dm}^3\text{g}^{-1}\text{s}^{-1})\times5.7\times10^{-12}\,(\text{g})}{2.0\times10^{-14}\ (\text{dm}^3)} = 3.1\,\text{s}^{-1}\,.$$

3.4.2.3. Alkyl hydroperoxide reductase

From the molecule counts per cell in ref. [113] the estimated concentration of Ahp1 is:

$$Ahp1 = \frac{\frac{N_{Ahp1}}{N_A}}{V_{cytoplasm}} = \frac{\frac{16228\ \text{molecule}}{6.02\times10^{23}\ \text{molecule mol}^{-1}}}{2.0\times10^{-14}\ \text{dm}^3} = 1.3\ \mu\text{M}$$

The second-order rate constant for H_2O_2 reduction by Ahp1 can be estimated from the specific activity (3.3×10^{-4} mol g^{-1} s^{-1}) and Michaelis constant (1.5×10^{-4} M) determined in ref. [116], considering a molecular mass of 1.9×10^4 g mol^{-1} (http://www.uniprot.org/)[22]:

$$k^*_{Ahp1} = \frac{3.3\times10^{-4}\,(\mathrm{mol\,g^{-1}\,s^{-1}})\times 1.9\times10^{4}\,(\mathrm{g\,mol^{-1}})}{1.5\times10^{-4}\,(\mathrm{M})} = 4.2\times10^{4}\,\mathrm{M^{-1}s^{-1}}\ .$$

From this one obtains the following pseudo-first order rate constant:

$$k_{Ahp1} = 1.3\times10^{-6}\,(\mathrm{M})\times 4.2\times10^{4}\,(\mathrm{M^{-1}s^{-1}}) = 0.054\,\mathrm{s^{-1}}\ ,$$

which is negligible in comparison to other H_2O_2 sinks.

Altogether, the H_2O_2 clearance capacity through processes other than reduction by the typical 2-Cys peroxiredoxins and including the efflux through the plasma membrane adds up to:

$$k_{Alt} = (21. + 3.1 + 9.5)\,\mathrm{s^{-1}} = 34.\,\mathrm{s^{-1}}$$

3.4.3. Peroxiredoxin concentrations and rate constants

S. cerevisiae contains two cytoplasmic typical 2-Cys peroxiredoxins, Tsa1 and Tsa2. Their cytoplasmic concentrations can be estimated from the protein counts in ref. [113] as:

$$Tsa1 = \frac{\frac{N_{Tsa1}}{N_A}}{V_{cytoplasm}} = \frac{\frac{378212\ \mathrm{molecule}}{6.02\times10^{23}\,\mathrm{molecule\ mol^{-1}}}}{2.0\times10^{-14}\ \mathrm{dm^3}} = 31.\,\mu\mathrm{M}\ ,$$

$$Tsa2 = \frac{\frac{N_{Tsa2}}{N_A}}{V_{cytoplasm}} = \frac{\frac{4820\ \mathrm{molecule}}{6.02\times10^{23}\,\mathrm{molecule\ mol^{-1}}}}{2.0\times10^{-14}\ \mathrm{dm^3}} = 0.40\ \mu\mathrm{M}\ .$$

The rate constants for H_2O_2 reduction by these Prx have been determined by Tairum *et al.* [117] as (4.7±2.2)x10^7 $M^{-1}s^{-1}$ and (5.0±1.7)x10^6 $M^{-1}s^{-1}$, respectively. (For comparison, previous determinations [118] yielded 2.2x10^7 $M^{-1}s^{-1}$ and 1.3x10^7 $M^{-1}s^{-1}$, respectively.) Because Tsa1 is much more abundant than Tsa2 it is a good approximation to consider $Prx_T = 31.\,\mu\mathrm{M}$, $k_{Ox} = 4.7\times10^{7}\,\mathrm{M^{-1}s^{-1}}$.

The rate constants for the condensation reaction and for Prx-SS reduction by Trx1 were estimated through a global fit of the following model (44) to the NADPH oxidation progress curves reported in ref. [119]:

$$\frac{d\ Tsa1\text{-}S^-}{dt} = k_{Red} \times Tsa1\text{-}SS \times Trx1\text{-}S^- - k_{Ox} \times Tsa1\text{-}S^- \times H_2O_2$$

$$\frac{d\ Tsa1\text{-}SO^-}{dt} = k_{Ox} \times Tsa1\text{-}S^- \times H_2O_2 - k_{Cond} \times Tsa1\text{-}SO^- - k_{Sulf} \times Tsa1\text{-}SO^- \times H_2O_2$$

$$\frac{d\ Tsa1\text{-}SS}{dt} = k_{Cond} \times Tsa1\text{-}SO^- - k_{Red} \times Tsa1\text{-}SS \times Trx1\text{-}S^-$$

$$\frac{d\ Trx1\text{-}S^-}{dt} = k_{Trr1} \times Trx1\text{-}SS - k_{Red} \times Tsa1\text{-}SS \times Trx1\text{-}S^- \quad (44)$$

$$\frac{d\ NADPH}{dt} = -k_{Trr1} \times Trx1\text{-}SS$$

$$Tsa1_T = Tsa1\text{-}SS + Tsa1\text{-}S^- + Tsa1\text{-}SO^- + Tsa1\text{-}SO_2^-$$

$$Trx1_T = Trx1\text{-}SS + Trx1\text{-}S^-$$

In order to make all the relevant parameters identifiable and facilitate the global fitting we rescaled all the variables as follows:

$$x = \frac{Tsa1\text{-}S^-}{Tsa1_T},\ y = \frac{Tsa1\text{-}SO^-}{Tsa1_T},\ z = \frac{Tsa1\text{-}SS}{Tsa1_T},\ w = \frac{Tsa1\text{-}SO_2^-}{Tsa1_T},$$

$$r = \frac{Trx1\text{-}S^-}{Trx1_T},\ s = \frac{Trx1\text{-}SS}{Trx1_T},\ n = \frac{NADPH}{Trx1_T},$$

$$\tau = t \times k_{Trr1},\ \mu = \frac{Tsa1_T}{Trx1_T},\ \delta = \frac{k_{Cond} \times Tsa1_T}{Trx1_T},$$

$$\psi = \frac{k_{Cond}}{k_{Trr1}},\ \rho = \frac{k_{Red} \times Tsa1_T}{k_{Trr1}},\ \alpha = \frac{k_{Ox} \times Tsa1_T^2}{k_{Trr1}},\ \xi = \frac{k_{Sulf} \times Tsa1_T}{k_{Trr1}}.$$

We fixed the value of $k_{Trr1} = 3.4 \times 10^7\,(\mathrm{M^{-1}s^{-1}}) \times 2.0 \times 10^{-7}\,(\mathrm{M}) = 6.8\,\mathrm{s^{-1}}$ based on the $k_{cat}\ /\ K_M = 3.4 \times 10^7\,\mathrm{M^{-1}s^{-1}}$ value determined in ref. [120], and we used the NonlinearModelFit

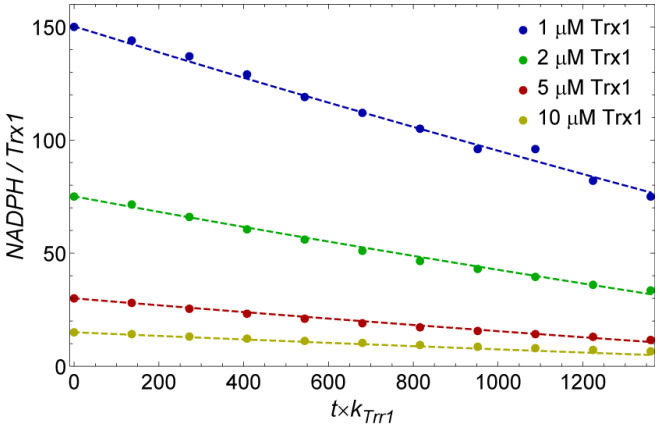

Supplementary Figure 7. Global fit (broken lines) of the NADPH progress curves reported in ref. [119] *(dots) for reaction mixtures containing 150 μM NADPH, 200 μM H_2O_2, 1 μM Tsa1, 0.2 μM Trr1, and 1 μM , 2 μM, 5 μM and 10 μM Trx1. Fitted values are ρ= 0.195±0.015, ψ= 0.0854±0.0045, ξ= (9.±5.0)×10^{-7} (R^2= 0.9996).*

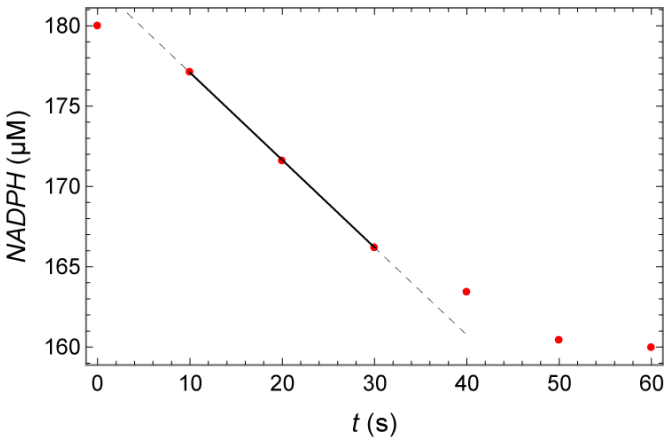

Supplementary Figure 8. Determination of the rate of NADPH consumption in the experiment reported in in Figure 6A from ref. [121]**.** *The reaction mixture contained 0.225 μM Trx2, 0.075 μM thioredoxin reductase 2, 2.1 μM Tsa1, 0.18 mM NADPH, 20 μM H_2O_2, 1 mM azide, 100 μM DTPA, 50 mM Hepes.NaOH, pH 7.4. The black line was fitted to the 10 s – 20 s data points, yielding a slope 5.4×10^{-7} M s^{-1}.*

function of *Mathematica*™ 10.3 with default settings to fit the scaled model to the data, with ρ, ψ as adjustable parameters. This procedure achieved an excellent fit (Supplementary Figure 7). Solving the scaling for the original parameters yields $k_{Cond} = 0.58 \pm 0.046\ \mathrm{s}^{-1}$, $k_{Red} = (1.33 \pm 0.071) \times 10^6\ \mathrm{M}^{-1}\mathrm{s}^{-1}$, $k_{Sulf} = 7. \pm 3.4\ \mathrm{M}^{-1}\mathrm{s}^{-1}$. Of note, this value for k_{Sulf} is much lower than that estimated for the human typical 2-Cys peroxiredoxins [63], consistent with the low hyperoxidation shown in the experiments in ref. [119] for Tsa1 treatment with 200 μM H_2O_2.

The value of k_{Red} for the reduction of Tsa1 by Trx2 was roughly estimated from the rate of NADPH oxidation reported in Figure 6A from ref. [121] (Supplementary Figure 8). In order to approximate the concentration of NADPH we assumed that the decrease in absorbance at 340 nm over the course of the experiment corresponded to the consumption of 20 μM NADPH, the H_2O_2 concentration initially present in the reaction medium. With this approximation, the time course showed a decrease in NADPH concentration at a constant rate of 0.54 μM s^{-1} from 10 s to 30 s, from which a $k_{Red} = 1.2 \times 10^6\ \mathrm{M}^{-1}\mathrm{s}^{-1}$ can be estimated. This value is within the experimental error of the value estimated above for Tsa1 reduction by Trx1 and of the same order of magnitude of that (6.4x10^6 M^{-1}s^{-1}) determined for the reduction of Ahp1 by Trx2 [122].

The value of k_{Red} to be considered in the model is a concentration-weighted average of the values for Trx1 and Trx2:

$$k_{Red} = 0.33 \times 1.33 \times 10^6\ \mathrm{M^{-1}s^{-1}} + 0.67 \times 1.2 \times 10^6\ \mathrm{M^{-1}s^{-1}} = 1.2 \times 10^6\ \mathrm{M^{-1}s^{-1}}\ ,$$

where 0.33 and 0.67 are the fractions of Trx contributed by Trx1 and Trx2, respectively (Section 3.4.5). In lack of specific data we assume that the sulfinylation rate constant for Tsa2 is similar to that for Tsa1. This assumption is of minor consequence, given the low concentration of Tsa2.

3.4.4. Sulfiredoxin concentration and activity

The cytoplasmic concentration of Srx was estimated from spectral count in ref. [113], under the assumptions that concentration is the same in the cytoplasm and in the nucleus and that the nucleus constitutes 9% of the cell volume [112]:

$$Srx = \frac{\frac{N_{Srx}}{N_A}}{V_{cytoplasm} + V_{nucleus}} = \frac{\frac{538\ \mathrm{molecule}}{6.02 \times 10^{23}\ \mathrm{molecule\ mol^{-1}}}}{(20. + 2.6) \times 10^{-15}\ \mathrm{dm^3}} = 0.039\ \mu\mathrm{M}\ .$$

The catalytic constant for yeast Srx is (3.0±0.1)×10^{-2} s^{-1} [78] and a K_M(Tsa1-SO_2^-)= 20 μM can be inferred from data in ref. [76]. Thus, except when a large fraction of Tsa1 is sulfinylated the reduction of Tsa1-SO_2^- follows approximately pseudo-first order kinetics with a rate constant

$$k_{Srx} = \frac{3.0 \times 10^{-2}\ (\mathrm{s^{-1}})}{2.0 \times 10^{-5}\ (\mathrm{M})} 3.9 \times 10^{-8}\ (\mathrm{M}) = 5.9 \times 10^{-5}\ \mathrm{s^{-1}}.$$

At Tsa1-SO_2^- concentrations substantially above 20 μM the reduction rate will eventually saturate at $3.0 \times 10^{-2}\ (\mathrm{s^{-1}}) \times 3.9 \times 10^{-8}\ (\mathrm{M}) = 1.2\ \mathrm{nM\,s^{-1}}$. Because these high Tsa1-SO_2^- concentrations, corresponding to >65% hyperoxidation, should only be attained at very high v_{sup}, we neglect Srx saturation.

3.4.5. Thioredoxin concentration

S. cerevisiae has two thioredoxin isoforms that are functionally redundant to a large extent and are present in most organelles: Trx1 and Trx2. We considered the two isoform as a single thioredoxin. From the protein count in ref. [113] we can estimate their aggregate concentration as:

$$Trx_T = \frac{\frac{N_{Trx1} + N_{Trx2}}{N_A}}{f_{water} V_{yeast}} = \frac{\frac{(8579 + 17237)\ \mathrm{molecule}}{6.02 \times 10^{23}\ \mathrm{molecule\ mol^{-1}}}}{0.68 \times 4.2 \times 10^{-14}\ \mathrm{dm^3}} = 1.5\ \mu\mathrm{M}$$

3.4.6. Thioredoxin reductase concentration and activity

From the spectral count in ref. [113] we can estimate the concentration of TrxR1 as follows, neglecting its contents in the mitochondrial intermembrane space:

$$TrxR = \frac{\frac{N_{TrxR}}{N_A}}{V_{cytoplasm}} = \frac{\frac{292122\ \text{molecule}}{6.02\times10^{23}\ \text{molecule mol}^{-1}}}{2.0\times10^{-14}\ \text{dm}^3} = 24.\ \mu\text{M}$$

S. cerevisiae TrxR has similar $k_{cat} = 43.\,\text{s}^{-1}$ for both Trx1 and Trx2,[120] which translates into

$$V_{Max} = k_{cat} \times TrxR = 43.(\text{s}^{-1}) \times 2.4\times10^{-5}(\text{M}) = 1.0\ \text{mM}\,\text{s}^{-1}.$$

The K_M for these two substrates are also quite similar (1.3 μM and 0.6 μM, respectively [120]) yielding a weighted average

$$K_M = \frac{8579\times1.3\,(\mu\text{M}) + 17237\times0.6\,(\mu\text{M})}{8579+17237} = 0.8\,\mu\text{M}\,.$$

3.5. Summary of protein concentrations and kinetic parameters

Supplementary Table 6. Summary of the protein concentrations and kinetic parameters estimated in this work. *The values of the concentrations and parameters entering the kinetic model are presented in Table 2 of the main text. Italicized values were determined specifically for the cells in point.*

	PrxI	PrxII	PrxVI	GPx1	Cat	Srx	Grx1	Trx1	TrxR1	k_{Cat}	k_{PrxVI}	k_{Gpx1}	k_{Inf}
Localization:	C	C	C	C/M	P [a]	C	C	C	C	-	-	-	-
Units:	μM	μM	μM	μM	μM	μM	μM	μM	μM	s^{-1}	s^{-1}	s^{-1}	s^{-1}
A549	47.	2.0	11.	0.27	1.4	1.0	1.9	29.	7.7	0.13	33.	0.96	10.
GAMG	71.	5.4	14.	3.6	3.2	0.57	1.2	44.	7.6	0.32	42.	13.	10.
HEK293	1.1×10^2	32.	45.	4.6	1.1	0.092	0.33	46.	2.5	0.11	1.3×10^2	16.	10.
HeLa	51.	15.	27.	0.98	1.9	0.24	0.41	24.	3.1	*3.0*	80.	*73.*	*12.*
HepG2	69.	24.	36.	2.1	4.5	0.57	4.9	27.	1.5	0.44	1.1×10^2	7.1	10.
Jurkat T	1.2×10^2	46.	25.	1.2	4.1	0.12	9.4	36.	5.5	*0.40*	75.	*4.1*	*5.2*
K562	72.	29.	55.	0.1	3.9	0.077	0.026	28.	1.8	0.38	1.6×10^2	0.35	10.
LnCap	50.	36.	33.	5.6	9.8	0.21	0.23	17.	4.1	0.96	1.0×10^2	19.	10.
MCF-7	59.	33.	17.	3.5	1.9	0.74	0.17	23.	3.0	*7.0*	51.	*6.8*	*14.*
RKO	59.	28.	43.	1.1	0.89	1.5	15.	69.	3.6	0.086	1.3×10^2	3.7	10.
U-2 OS	73.	11.	27.	1.5	1.6	0.55	2.9	18.	4.4	0.16	82.	5.2	10.
HepG2[b]	86.	24.	21.	0.049	7.8	0.34	2.9	24.	0.62	0.76	63.	0.17	10.
Hepatocytes[b]	67.	19.	61.	2.4	43.	0.065	4.7	63.	0.65	4.2	1.8×10^2	8.3	10.
Erythrocytes	6.8	5.7×10^2	3.0	1.3×10^2	24.[c]	-	-	0.56	0.13	*218.*	9.0	*25.*	*11.*
Yeast	31.[d]	0.40[e]	-	0.54[f]	-	0.039[g]	-	1.5[h]	24.	3.1	-	21.	9.5

Subcellular localization is reported as: N, nuclear; C, cytoplasmic; M, mitochondrial; P, peroxisome.

[a] Concentration referred to cell water volume. [b] From the dataset in ref. [21]. [c] In erythrocytes catalase is localized in the cytoplasm.

[d] Tsa1. [e] Tsa2. [f] CcP [g] Also localized to the nucleus. [h] Present in most organelles.

4. Numerical model considering PrxI and PrxII separately

In order to evaluate the redox state of PrxI and PrxII separately in simulations of wet-lab experiments we set up the model below, which treats these Prx as separate entities and accounts for H_2O_2 permeation.

$$\frac{d\,H_2O_{2,out}}{dt} = \frac{\kappa\, n_{cells} S}{V_{medium}}(H_2O_2 - H_2O_{2,out})$$

$$\frac{d\,H_2O_2}{dt} = \frac{\kappa\, S}{V_{cytoplasm}}(H_2O_{2,out} - H_2O_2) - k_{Alt}H_2O_2 - k_{Ox}\,(PrxI\text{-}S^- + PrxII\text{-}S^-)\,H_2O_2 - \\ - k'_{Sulf}\,PrxI\text{-}SO^-\,H_2O_2 - k''_{Sulf}\,PrxII\text{-}SO^-\,H_2O_2$$

$$\frac{d\,PrxI\text{-}SO^-}{dt} = k_{Ox}\,PrxI\text{-}S^-\,H_2O_2 + k_{Srx}PrxI\text{-}SO_2^- - k'_{Sulf}\,PrxI\text{-}SO^-\,H_2O_2 - k'_{Cond}\,PrxI\text{-}SO^-$$

$$\frac{d\,PrxI\text{-}SO_2^-}{dt} = k'_{Sulf}\,PrxI\text{-}SO^-\,H_2O_2 - k_{Srx}PrxI\text{-}SO_2^-$$

$$\frac{d\,PrxI\text{-}SS}{dt} = k'_{Cond}\,PrxI\text{-}SO^- - k_{Red}\,Trx\text{-}S^-\,PrxI\text{-}SS$$

$$\frac{d\,PrxII\text{-}SO^-}{dt} = k_{Ox}\,PrxII\text{-}S^-\,H_2O_2 + k_{Srx}PrxII\text{-}SO_2^- - k''_{Sulf}\,PrxII\text{-}SO^-\,H_2O_2 - k''_{Cond}\,PrxII\text{-}SO^-$$

$$\frac{d\,PrxII\text{-}SO_2^-}{dt} = k''_{Sulf}\,PrxII\text{-}SO^-\,H_2O_2 - k_{Srx}PrxII\text{-}SO_2^-$$

$$\frac{d\,PrxII\text{-}SS}{dt} = k''_{Cond}\,PrxII\text{-}SO^- - k_{Red}\,Trx\text{-}S^-\,PrxII\text{-}SS$$

$$\frac{d\,Trx\text{-}SS}{dt} = k_{Red}Trx\text{-}S^-(PrxI\text{-}SS + PrxII\text{-}SS) - \frac{V_{Max}^{App}\,Trx\text{-}SS}{K_M + Trx\text{-}SS}$$

$$PrxI_T = PrxI\text{-}S^- + PrxI\text{-}SS + PrxI\text{-}SO^- + PrxI\text{-}SO_2^-$$

$$PrxII_T = PrxII\text{-}S^- + PrxII\text{-}SS + PrxII\text{-}SO^- + PrxII\text{-}SO_2^-$$

$$Trx_T = Trx\text{-}S^- + Trx\text{-}SS$$

Here, $H_2O_{2,out}$ stands for the concentration of H_2O_2 in the medium, κ stands for the permeability constant of the cell membrane, n_{cells} stands for the number of cells in the medium volume (V_{medium}) considered, and k'_{Cond}, k''_{Cond} (k'_{Sulf}, k''_{Sulf}) represent the condensation (sulfinylation) rate constants for PrxI-SO$^-$ and PrxII-SO$^-$, respectively.

5. Simulation of experimental results

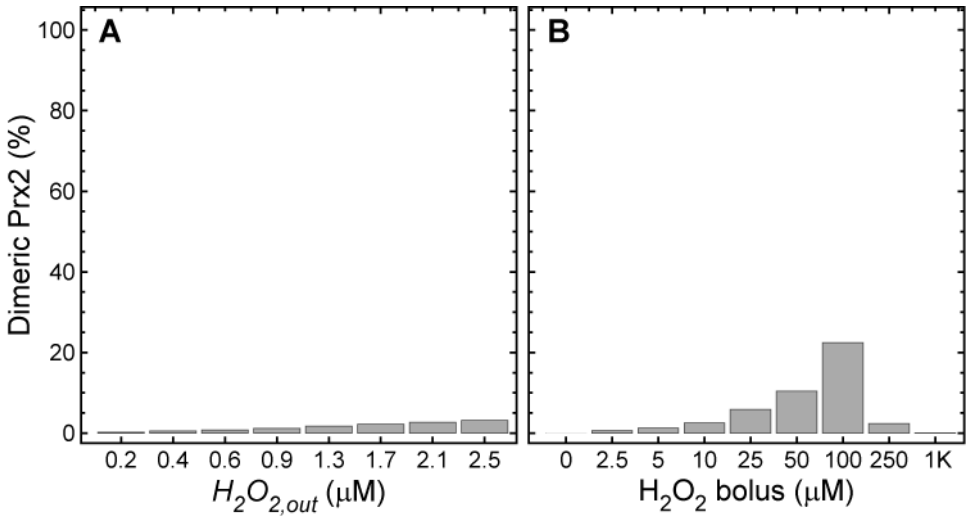

Supplementary Figure 9. Simulation of experiments treating HEK293 cells with H_2O_2 steady states (A) and boluses (B). *Plots show the percentage of disulfide-crosslinked PrxII dimers at various steady extracellular H_2O_2 concentrations (A), or 5 min after bolus treatment (B) under the conditions of the experiments described in Figures 6A and 6B (respectively) from Sobotta et al.* [33]. *Simulations were carried out using Model 2 (Section 0) with the parameters in Table 2 and Supplementary Table 6.*

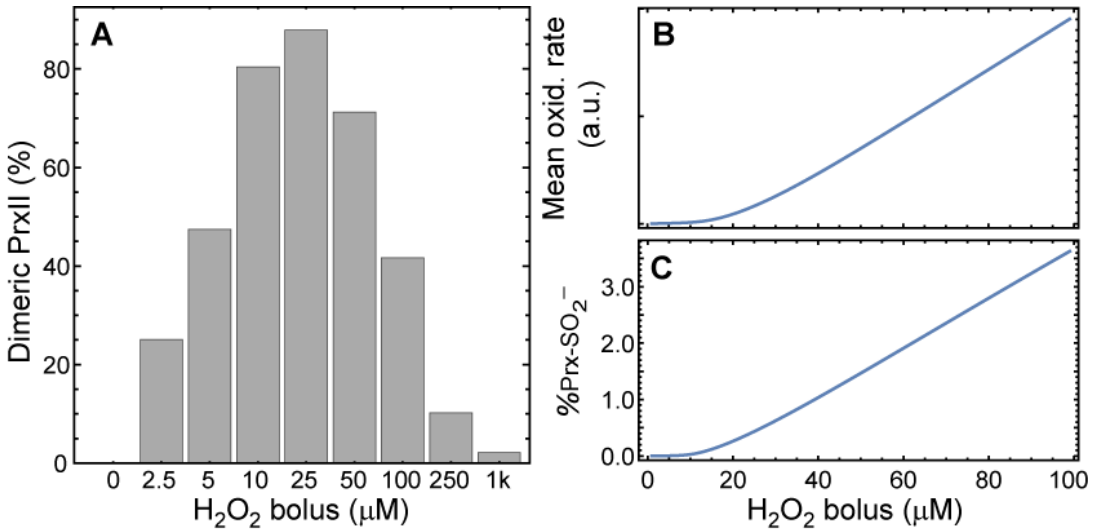

Supplementary Figure 10. Simulation of experiments treating HEK293 cells with H_2O_2 boluses considering a low Trx1 availability. *(A) Percentage of disulfide-crosslinked PrxII dimers 5 min after bolus treatment under the conditions of the experiments described in Figure 6B from Sobotta et al.* [33]*. The underestimation of crosslinked PrxII monomers at very high H_2O_2 boluses is likely due to the neglect of GSH and NADPH depletion at the extremely high v_{sup} values attained under these non-physiological conditions. (B) Mean H_2O_2 probe oxidation rate between t=30 s and t=120 s and (C) percentage of hyperoxidized Prx monomers 10 min after bolus treatment under the conditions of the experiments described in Figures 6D and 6F (respectively) from Tomalin et al.* [56]*. Simulations were carried out using Model 2 (Section 0) with the parameters in Table 2 and Supplementary Table 6, except for [Trx1]= 1.5 μM.*

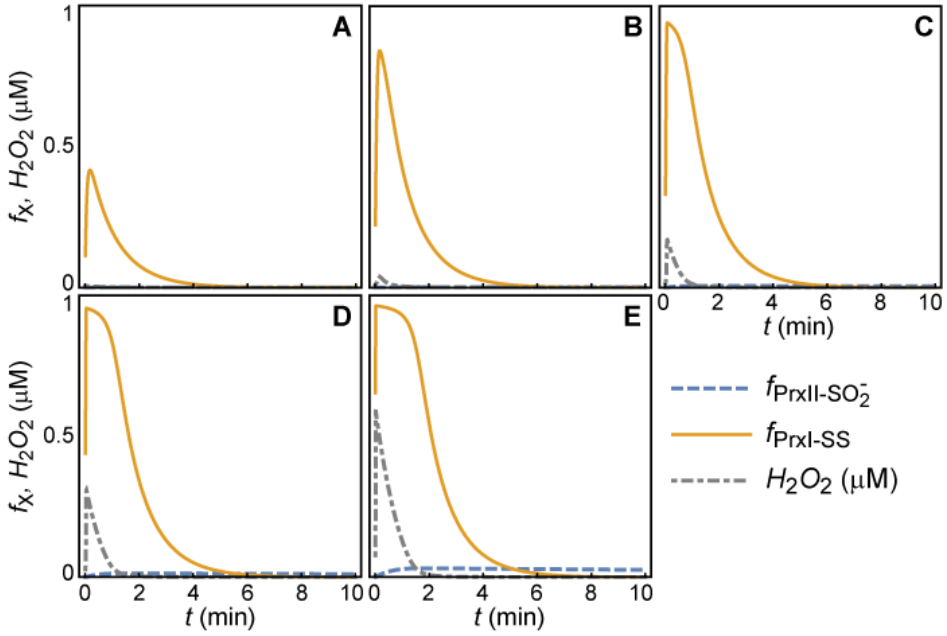

Supplementary Figure 11. Simulated time courses for treatment of HEK293 cells with H_2O_2 boluses. *Treatments under the conditions of the experiments described in Figures 6D and 6F from Tomalin et al.* [56]*. For comparison to Supplementary Figure 10B please note that the mean rate of probe oxidation is proportional to the area under the H_2O_2 curve from t= 30 s to t= 120 s. (A) 5 μM H_2O_2 bolus, (B) 10 μM, (C) 15 μM, (D) 20 μM, (E) 30 μM. Simulations were carried out using Model 2, with the same parameters as for Supplementary Figure 10. Similar results are obtained using Model 1, with the total fractions of disulfide and sulfinate peroxiredoxins as variables.*

1093

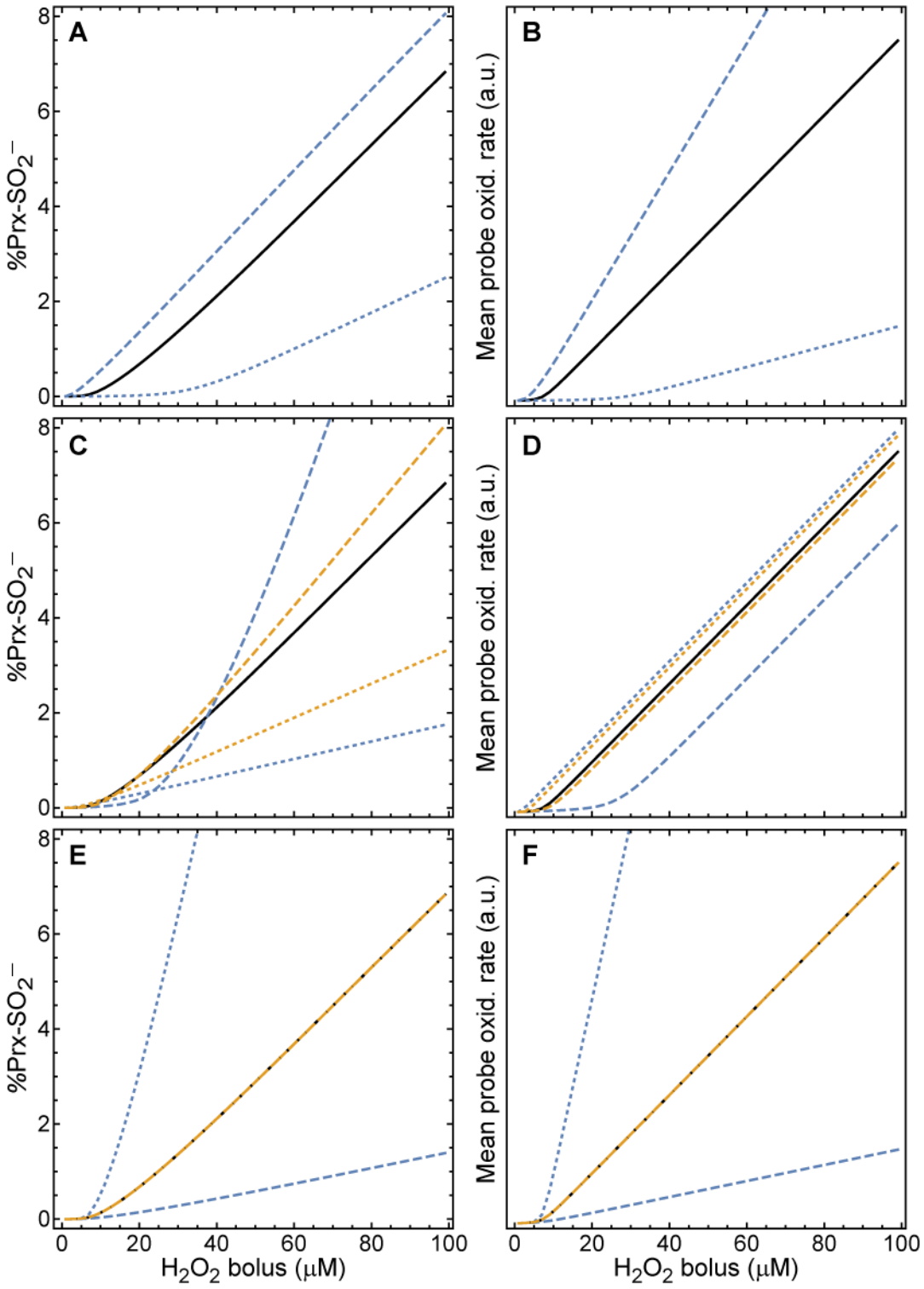

Supplementary Figure 12. Influence of various factors on the threshold for Prx hyperoxidation and cytoplasmic H_2O_2 accumulation. *Percentage of hyperoxidized Prx monomers 10 min after bolus treatment (A,C,E) and mean H_2O_2 probe oxidation rate between t=30 s and t=120 s (B,D,F) under the conditions of the experiments described in Figures 6F and 6D (respectively) from Tomalin et al.* [56]*. Except as otherwise indicated, simulations were carried out using Model 1 and the parameters in Table 2 and Supplementary Table 6 for HEK293 cells (except [Trx1]= 1.5 μM) as reference. Solid black lines, results obtained for the reference parameter values; dotted and dashed lines, effect of 5-fold decrease or increase (respectively) of the following parameters: (A,B) permeability constant; (C,D)* Trx_T*, blue;* V_{Max}^{App}*, yellow; (E,F)* k_{Alt}*, blue;* Prx_T*, yellow, overlapping the black line.*

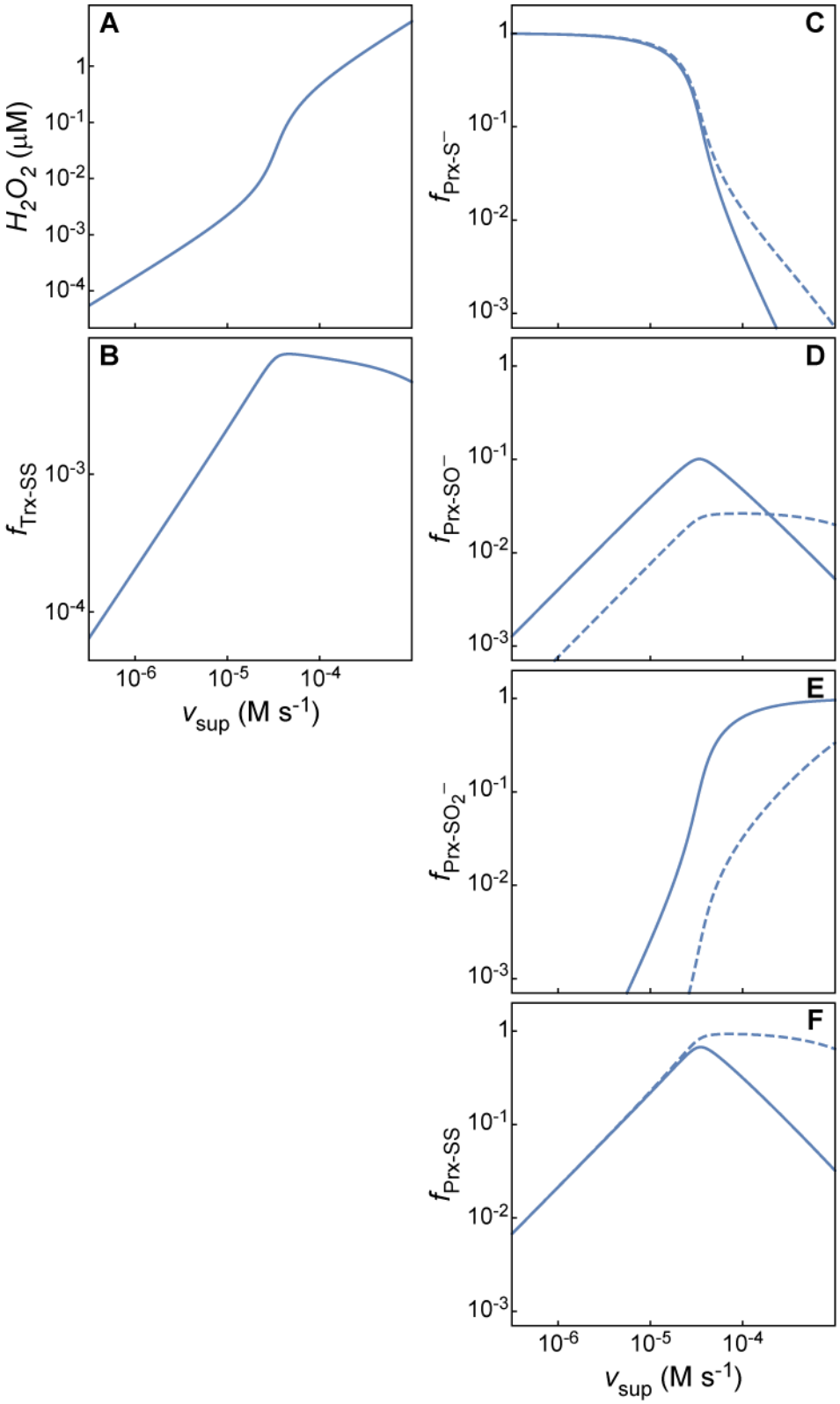

Supplementary Figure 13. Simulated steady state response of the PTTRS in HEK293 cells to H_2O_2 supply. *In panels C-F solid and dashed lines refer to PrxII and PrxI, respectively. Simulations were carried out using a variant of Model 2 (Section 0) replacing H_2O_2 permeation by a prescribed H_2O_2 supply rate (v_{sup}). Parameter values are as shown in Table 2 and Supplementary Table 6 for HEK293 cells, except for [Trx1]= 1.5 μM. Note the quite abrupt decrease in the fraction of both PrxI and PrxII in thiolate form over a narrow range of v_{sup}.*

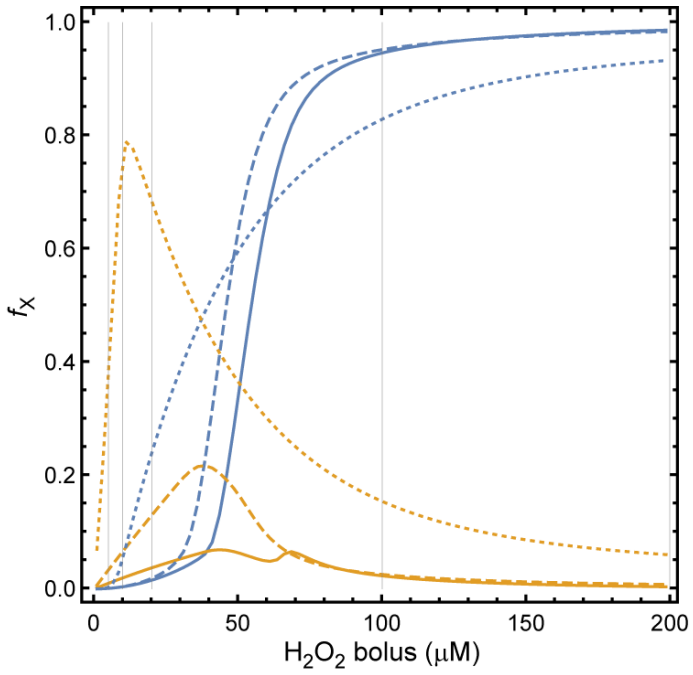

Supplementary Figure 14. Simulation of experiments treating Jurkat T cells with H_2O_2 boluses. *Fraction of Prx as Prx-SO_2^- (blue) and Prx-SS (yellow) for 10^6 Jurkat T cells/mL 10 min after treatment with the indicated boluses, for 100% (solid lines), 30% (dashed) and 3% of the Trx concentration indicated in Supplementary Table 6 for this cell line. The vertical gray lines indicate the boluses examined in Figures 2E and 3A of ref.* [95]*. Comparisons must take into account that the experiments over-estimate the fraction of disulfide-crosslinked Prx dimers due to adventitious oxidation during sample handling.*[95] *Note that the simulations considering the Trx concentration estimated from the proteomic dataset yield a good fit to the experimental observations but those considering 30% or 3% of this concentration do not.*

1124

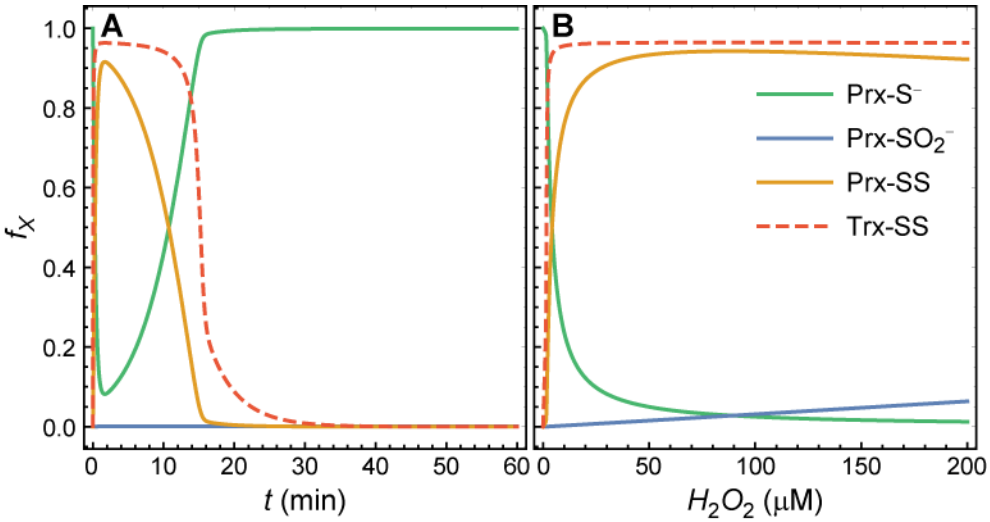

Supplementary Figure 15. Simulation of experiments treating human erythrocytes with H_2O_2 boluses. *Fraction of Prx as Prx-S^-, Prx-SO_2^- and Prx-SS, and of Trx as Trx-SS for 5×10^6 erythrocytes/mL treated with 5 μM H_2O_2 (A, compare to Figure 4A of ref.* [95]*) or 10 min after treatment with the indicated boluses (B, compare to Figure 3B of ref.* [95]*). Comparisons must take into account that the experiments over-estimate the fraction of disulfide-crosslinked Prx dimers due to adventitious oxidation during sample handling.*[95] *Although computational predictions with Model 1 are less accurate than those with the much more complex model in ref.* [31]*, they still provide a good match to the experimental observations.*

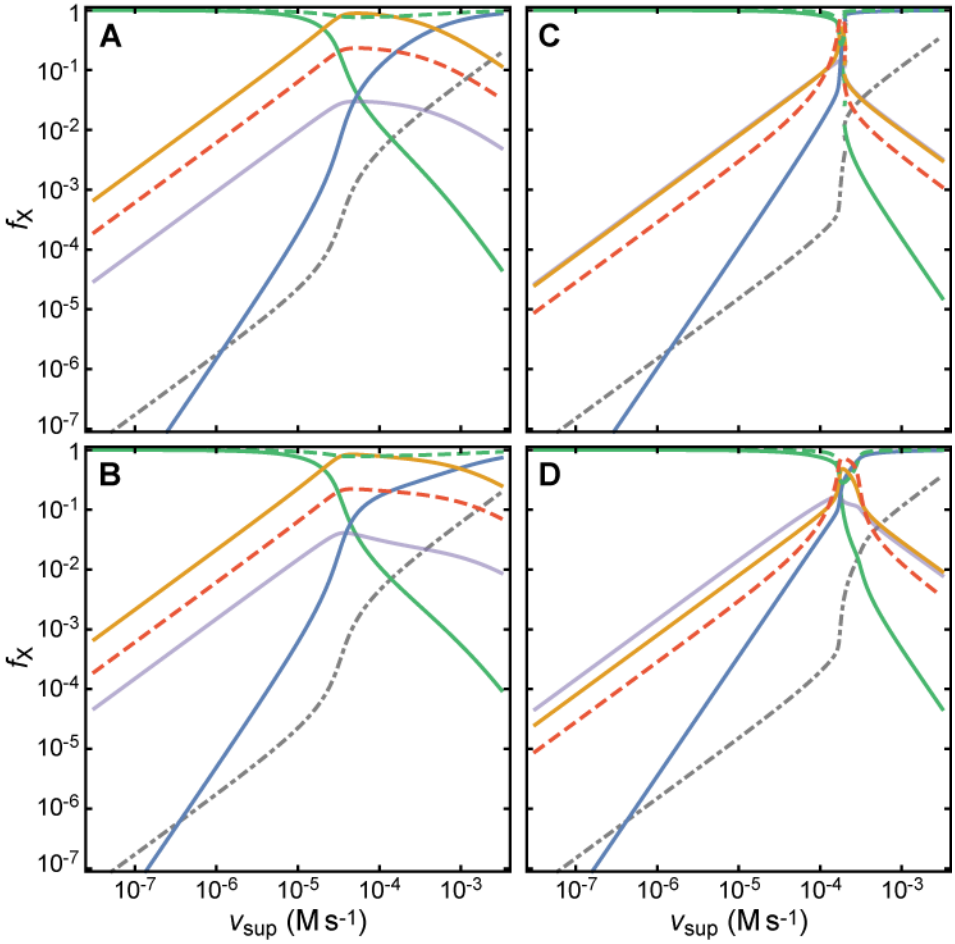

Supplementary Figure 16. Comparison of simulation results from Model 1 (A,C) and Model 2 (B,D) for HEK293 (A,B) and Jurkat T (C,D) cells. *Simulations were carried out using the parameters in Table 2 and Supplementary Table 6, except for [Trx1]= 1.5 μM in the case of HEK293. Both models predict essentially similar behavior. Color codes are as for Figure 2 except that cytoplasmic H_2O_2 concentrations are scaled by 100 μM.*

1132

6. Additional design space slices and responses

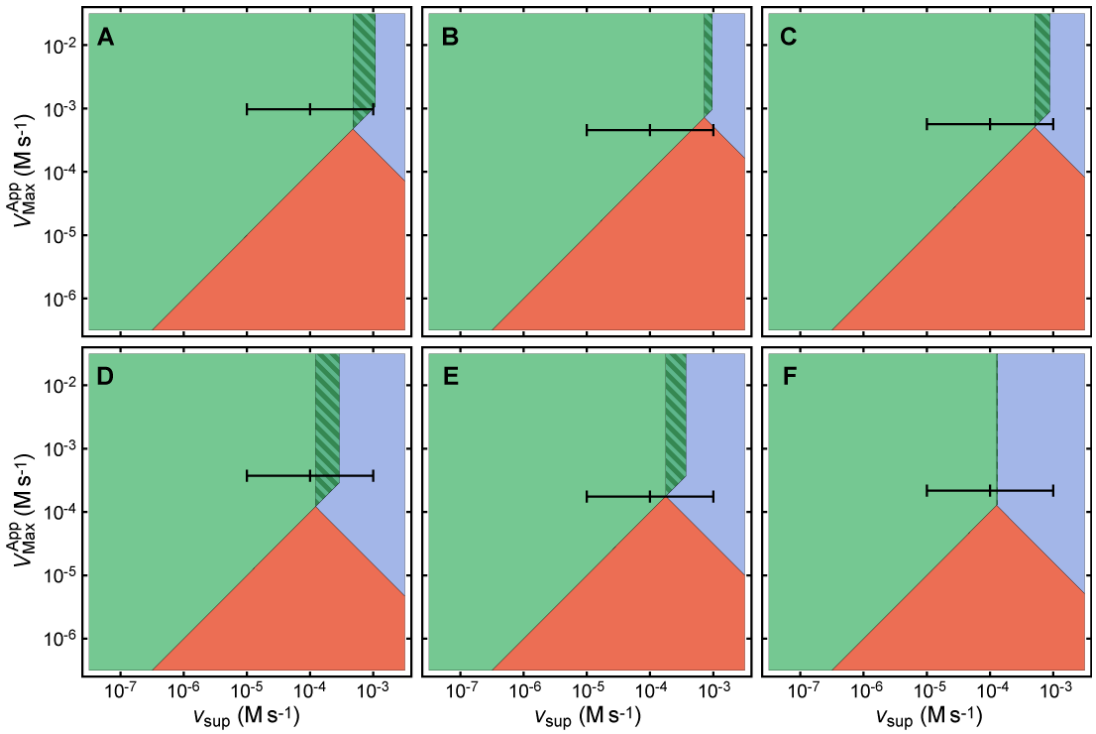

Supplementary Figure 17. Slices of the design space of the PTTRS over the physiological (v_{sup},V_{Max}^{App}) planes for GaMG (A,D) , RKO (B,E), and U-2 OS (C,F) cells. *In lack of reliable morphometric data for these cells, we consider the extreme values of $f_{cytoplasm}$ and $f_{nucleus}$ among the other cells in* ***Supplementary Table 4****. Namely, $f_{cytoplasm}$=0.3, $f_{nucleus}$=0.6 (A-C), and $f_{cytoplasm}$=0.78, $f_{nucleus}$=0.18 (D-F).*

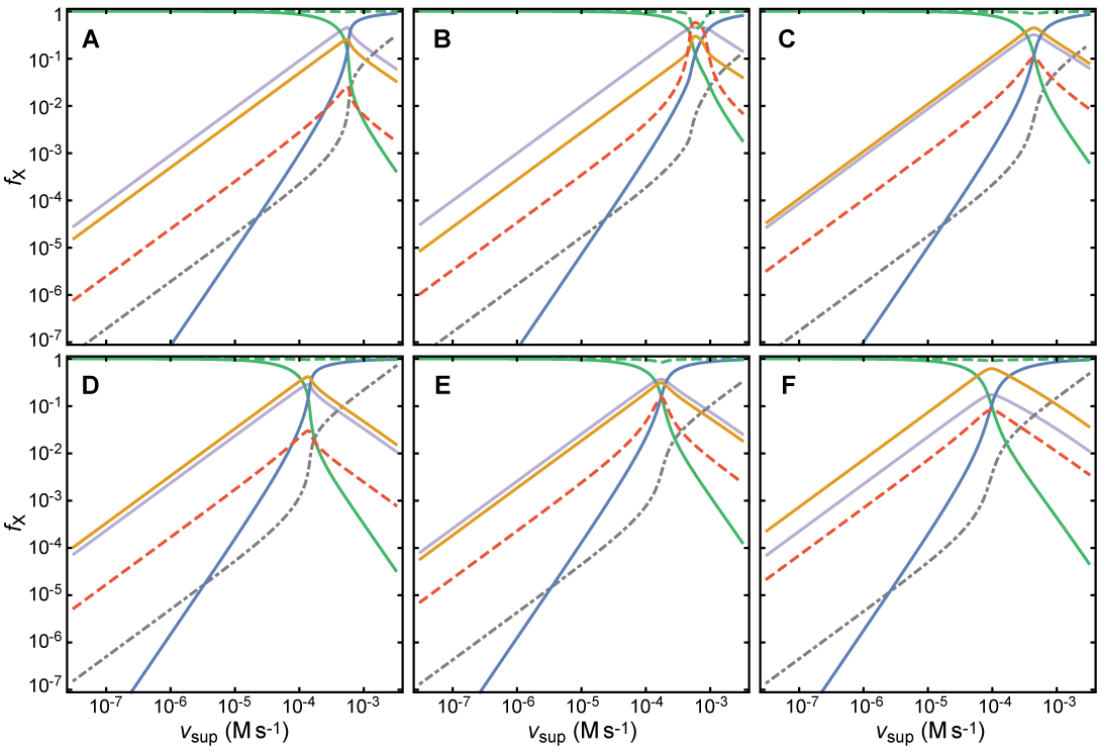

Supplementary Figure 18. Responses of the PTTRS to H_2O_2 supply rates in GaMG (A,D), RKO (B,E), and U-2 OS (C,F) cells. *Morphometric parameters are as for Supplementary Figure 17. Note the logarithmic scales.* Predictions at v_{sup} > ≈0.5 mM s^{-1} may be inaccurate due to neglect of NADPH depletion. *Color codes are as for Figure 2 from the main text. Cytoplasmic H_2O_2 concentrations are scaled by 100 μM.*

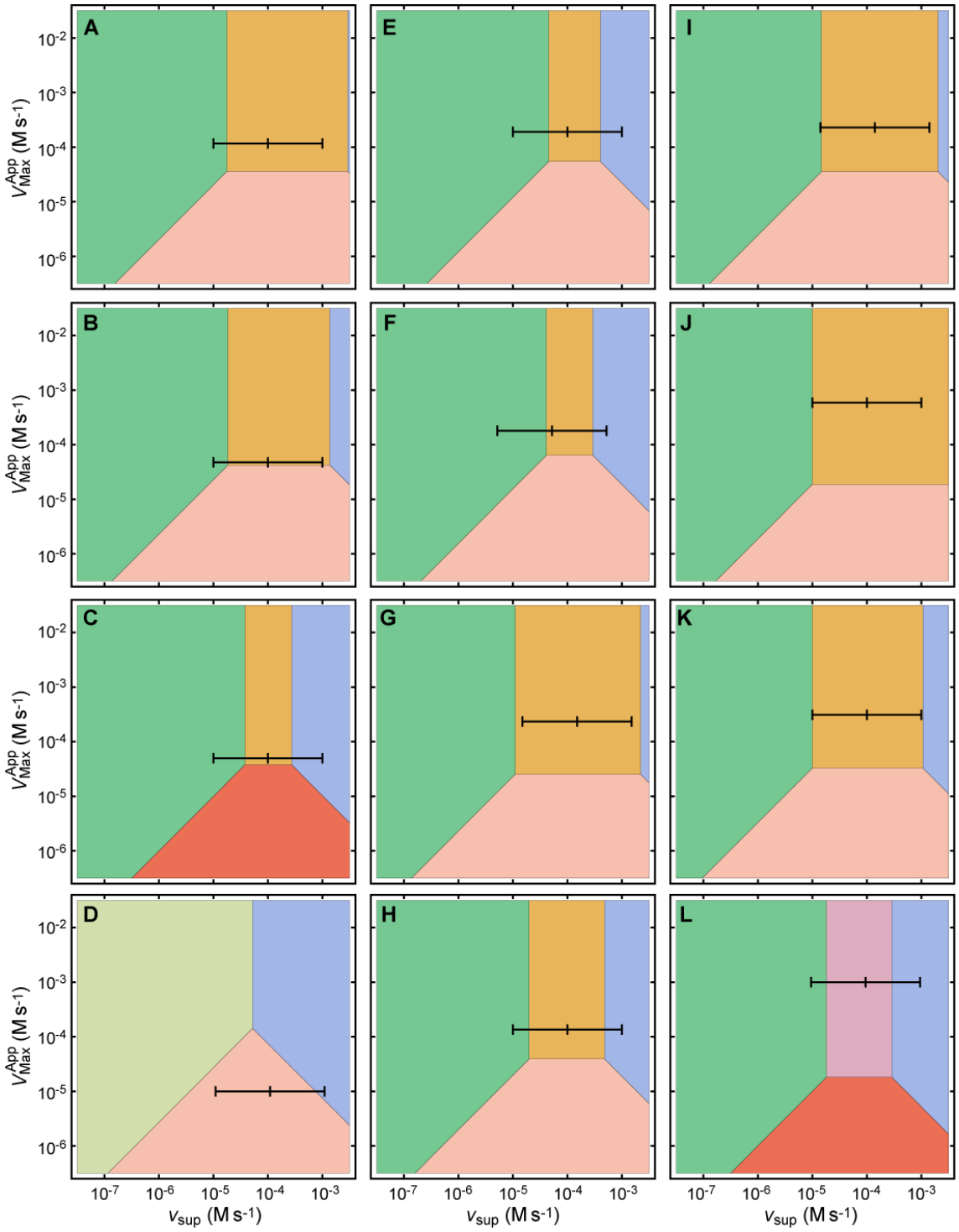

Supplementary Figure 19. Slices of the design space of the PTTRS over the physiological (v_{sup},V_{Max}^{App}) plane considering that only 3% of the Trx1 in nucleated human cells is available to reduce Prx-SS. *The black scales inside the plots mark the apparent V_{Max} of TrxR and the values of v_{sup} corresponding to 1 μM, 10 μM and 100 μM extracellular H_2O_2. These values of v_{sup} were estimated based on the known cell permeability and morphology (HeLa, MCF-7, Jurkat T cells, erythrocytes and S. cerevisiae) or assuming k_{Inf} = 10 s^{-1} (all other cells). Note the logarithmic scales. Color codes are as for Figure 2. A, HepG2, ref.* [52]*; B, HepG2, ref.* [21]*; C, hepatocytes; D, erythrocytes; E, HEK293; F, Jurkat T; G, HeLa; H, K562; I, MCF-7; J, A549; K, LnCap; L, S. cerevisiae.*

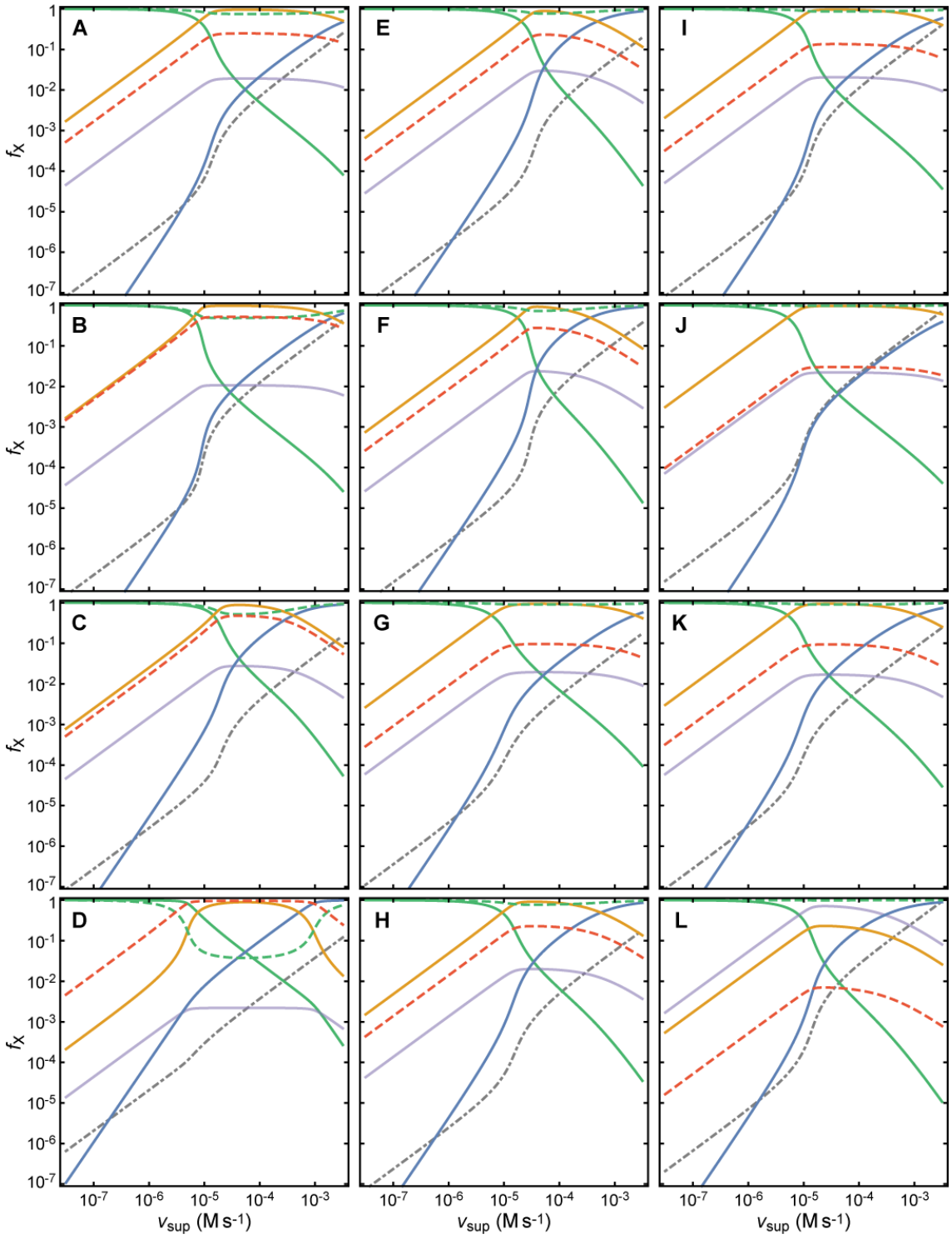

Supplementary Figure 20. Responses of the PTTRS to H_2O_2 supply rates for human cell types and S. cerevisiae considering that only 3% of the Trx1 in nucleated human cells is available to reduce Prx-SS. *Note the logarithmic scales. The plots were obtained by numerical integration of equations (1) in the main text with the parameters in Table 2, except for the concentration of Trx1 in nucleated human cells being 3% of the values presented in that table. Predictions of the responses at $v_{sup} > \approx 0.5$ mM s^{-1} may be inaccurate due to neglect of NADPH depletion. Color codes are as for Figure 2, except that cytoplasmic H_2O_2 concentrations are scaled by 100 μM. A, HepG2, ref.* [52]*; B, HepG2, ref.* [21]*; C, hepatocytes; D, erythrocytes; E, HEK293; F, Jurkat T; G, HeLa; H, K562; I,MCF-7; J, A549; K, LnCap; L, S. cerevisiae.*

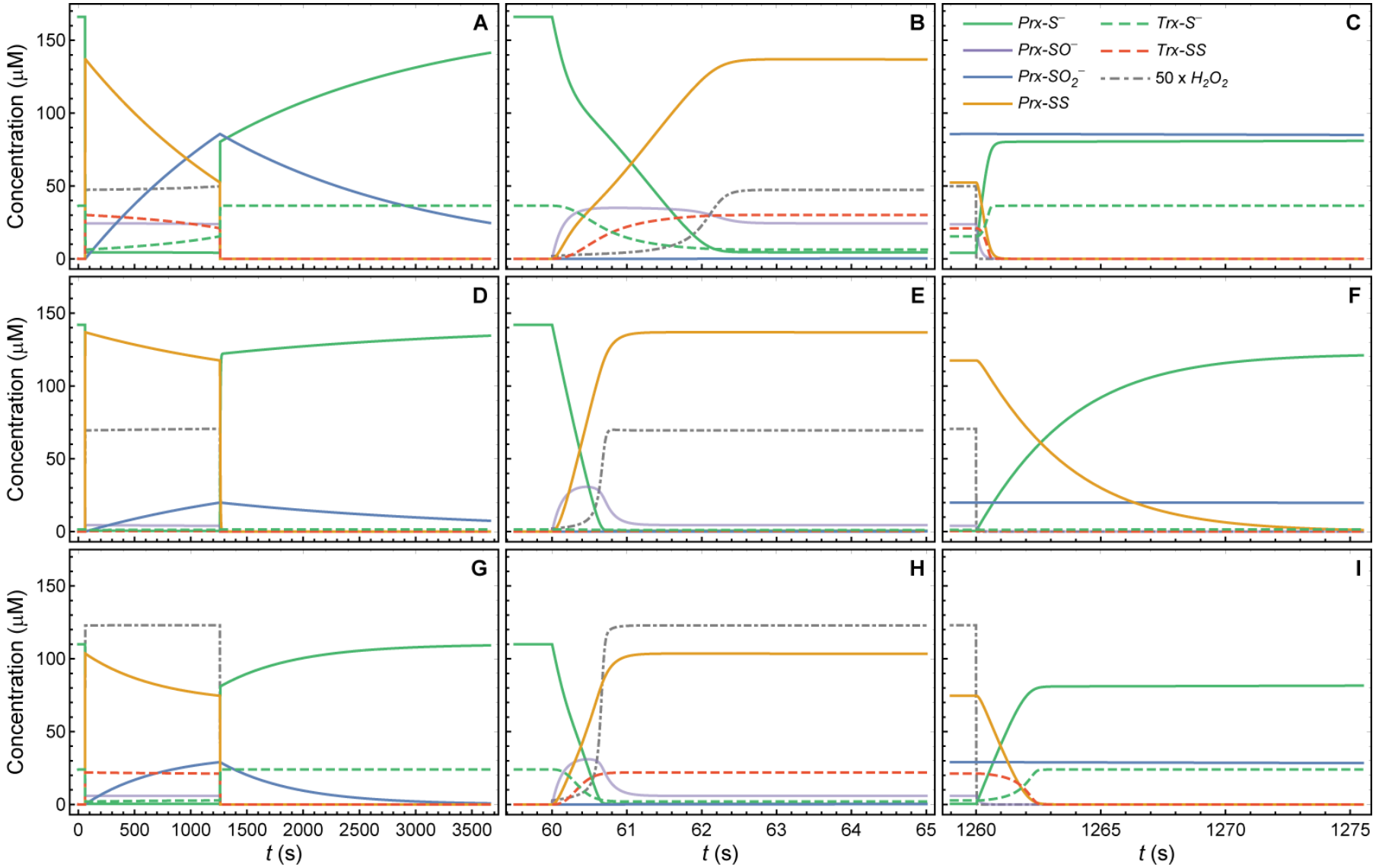
A
B
C
D
E
F
G
H
I
Prx-S⁻
Prx-SO⁻
Prx-SO2⁻
Prx-SS
Trx-S⁻
Trx-SS
50 x H2O2
Concentration (μM)
0
50
100
150
0
500
1000
1500
2000
2500
3000
3500
60
61
62
63
64
65
1260
1265
1270
1275
t (s)

1153

Supplementary Figure 21. Transient response of the PTTRS to temporary increases in H_2O_2 supply beyond the limits of region TTPU. *(A,B,C) Jurkat T cells, Response H; (D,E,F) HEK293 cells with Trx_T set to 1.5 μM, Response PD; (G,H,I) HepG2 cells, Response D. v_{sup} was increased from 10 nM s^{-1} to 250 μM s^{-1} between t= 60 s and t= 1260 s, amounting to a H_2O_2 dose near the limit of what cells can survive. The time scale is expanded around t= 60 s (B,E,H) and t= 1260 s (C,F,I) to show the fast dynamics following the onset and termination of the high-v_{sup} period. H_2O_2 concentrations are multiplied by 50, to fit in the same scale.*

7. References

[1] P.M.B.M. Coelho, A. Salvador, M.A. Savageau, Quantifying global tolerance of biochemical systems: design implications for moiety-transfer cycles., PLoS Computational Biology. 5 (2009) e1000319. doi:10.1371/journal.pcbi.1000319.

[2] M.A. Savageau, P.M.B.M. Coelho, R.A. Fasani, D.A. Tolla, A. Salvador, Phenotypes and tolerances in the design space of biochemical systems., Proceedings of the National Academy of Sciences of the United States of America. 106 (2009) 6435–40. doi:10.1073/pnas.0809869106.

[3] R.A. Fasani, M.A. Savageau, Automated construction and analysis of the design space for biochemical systems, Bioinformatics. 26 (2010) 2601–2609. doi:10.1093/bioinformatics/btq479.

[4] J.G. Lomnitz, M.A. Savageau, Phenotypic deconstruction of gene circuitry, Chaos. 23 (2013) 25108. doi:10.1063/1.4809776.

[5] J.G. Lomnitz, M.A. Savageau, Strategy revealing phenotypic differences among synthetic oscillator designs., ACS Synthetic Biology. 3 (2014) 686–701. doi:10.1021/sb500236e.

[6] J.G. Lomnitz, M.A. Savageau, Elucidating the genotype–phenotype map by automatic enumeration and analysis of the phenotypic repertoire, Npj Systems Biology and Applications. 1 (2015) 15003. doi:10.1038/npjsba.2015.3.

[7] M.A. Savageau, Design principles for elementary gene circuits: Elements, methods, and examples, Chaos. 11 (2001) 142–159. doi:10.1063/1.1349892.

[8] M.A. Savageau, Biochemical systems analysis. I. Some mathematical properties of the rate law for the component enzymatic reactions, Journal Of Theoretical Biology. 25 (1969) 365–369.

[9] M.A. Savageau, Biochemical systems analysis. II. The steady-state solutions for an n-pool system using a power-law approximation, Journal Of Theoretical Biology. 25 (1969) 370–379.

[10] M.A. Savageau, Biochemical systems analysis. III. Dynamic solutions using a power-law approximation, Journal Of Theoretical Biology. 26 (1970) 215–226.

[11] S. Schuster, T. Hofer, Determining all extreme semi-positive conservation relations in

chemical-reaction systems - A test criterion for conservativity, Journal Of The Chemical Society-Faraday Transactions. 87 (1991) 2561–2566.

[12] T. Geiger, A. Wehner, C. Schaab, J. Cox, M. Mann, Comparative proteomic analysis of eleven common cell lines reveals ubiquitous but varying expression of most proteins, Molecular & Cellular Proteomics: MCP. 11 (2012) M111.014050. doi:10.1074/mcp.M111.014050.

[13] W. Liebermeister, E. Noor, A. Flamholz, D. Davidi, J. Bernhardt, R. Milo, Visual account of protein investment in cellular functions, Proceedings of the National Academy of Sciences. 111 (2014) 8488–8493. doi:10.1073/pnas.1314810111.

[14] R. Milo, What is the total number of protein molecules per cell volume? A call to rethink some published values, BioEssays. 35 (2013) 1050–1055. doi:10.1002/bies.201300066.

[15] Z. Wang, W. Shen, D.P. Kotler, S. Heshka, L. Wielopolski, J.F. Aloia, M.E. Nelson, R.N. Pierson, S.B. Heymsfield, Total body protein: a new cellular level mass and distribution prediction model., The American Journal of Clinical Nutrition. 78 (2003) 979–84.

[16] R.J. Ellis, Macromolecular crowding: an important but neglected aspect of the intracellular environment, Current Opinion in Structural Biology. 11 (2001) 114–119. doi:10.1016/S0959-440X(00)00172-X.

[17] C. Fumarola, S. La Monica, R.R. Alfieri, E. Borra, G.G. Guidotti, Cell size reduction induced by inhibition of the mTOR/S6K-signaling pathway protects Jurkat cells from apoptosis., Cell Death and Differentiation. 12 (2005) 1344–57. doi:10.1038/sj.cdd.4401660.

[18] Y. Feng, N. Zhang, K.M. Jacobs, W. Jiang, L. V. Yang, Z. Li, J. Zhang, J.Q. Lu, X.-H. Hu, Polarization imaging and classification of Jurkat T and Ramos B cells using a flow cytometer, Cytometry Part A. 85 (2014) 986–986. doi:10.1002/cyto.a.22524.

[19] L. Brocchieri, S. Karlin, Protein length in eukaryotic and prokaryotic proteomes., Nucleic Acids Research. 33 (2005) 3390–400. doi:10.1093/nar/gki615.

[20] R. Milo, R. Phillips, Cell Biology by the Numbers, 1st ed., Taylor & Francis, New York, 2016.

[21] J.R. Wiśniewski, A. Vildhede, A. Norén, P. Artursson, In-depth quantitative analysis and comparison of the human hepatocyte and hepatoma cell line HepG2 proteomes, Journal of Proteomics. 136 (2016) 234–247. doi:10.1016/j.jprot.2016.01.016.

[22] The UniProt Consortium, UniProt: a hub for protein information, Nucleic Acids Research. 43 (2015) D204–D212. doi:10.1093/nar/gku989.

[23] R. Jiang, H. Shen, Y.-J. Piao, The morphometrical analysis on the ultrastructure of A549 cells., Romanian Journal of Morphology and Embryology. 51 (2010) 663–7.

[24] H. Kempe, A. Schwabe, F. Crémazy, P.J. Verschure, F.J. Bruggeman, The volumes and transcript counts of single cells reveal concentration homeostasis and capture biological noise., Molecular Biology of the Cell. 26 (2015) 797–804. doi:10.1091/mbc.E14-08-1296.

[25] A. Fujioka, K. Terai, R.E. Itoh, K. Aoki, T. Nakamura, S. Kuroda, E. Nishida, M. Matsuda, Dynamics of the Ras/ERK MAPK Cascade as Monitored by Fluorescent Probes, Journal of Biological Chemistry. 281 (2006) 8917–8926. doi:10.1074/jbc.M509344200.

[26] R. Huang, L. Zhao, H. Chen, R.-H. Yin, C.-Y. Li, Y.-Q. Zhan, J.-H. Zhang, C. Ge, M. Yu, X.-M. Yang, Megakaryocytic Differentiation of K562 Cells Induced by PMA Reduced the Activity of Respiratory Chain Complex IV, PLoS ONE. 9 (2014) e96246. doi:10.1371/journal.pone.0096246.

[27] D.C. Lazar, E.H. Cho, M.S. Luttgen, T.J. Metzner, M.L. Uson, M. Torrey, M.E. Gross, P. Kuhn, Cytometric comparisons between circulating tumor cells from prostate cancer patients and the prostate-tumor-derived LNCaP cell line., Physical Biology. 9 (2012) 16002. doi:10.1088/1478-3975/9/1/016002.

[28] M.J. Moore, E.M. Strohm, M.C. Kolios, Assessment of the Nucleus-to-Cytoplasmic Ratio in MCF-7 Cells Using Ultra-high Frequency Ultrasound and Photoacoustics, International Journal of Thermophysics. 37 (2016) 118. doi:10.1007/s10765-016-2129-y.

[29] P.J. Thul, L. Åkesson, M. Wiking, D. Mahdessian, A. Geladaki, H. Ait Blal, T. Alm, A. Asplund, L. Björk, L.M. Breckels, A. Bäckström, F. Danielsson, L. Fagerberg, J. Fall, L. Gatto, C. Gnann, S. Hober, M. Hjelmare, F. Johansson, S. Lee, C. Lindskog, J. Mulder, C.M. Mulvey, P. Nilsson, P. Oksvold, J. Rockberg, R. Schutten, J.M. Schwenk, Å. Sivertsson, E. Sjöstedt, M. Skogs, C. Stadler, D.P. Sullivan, H. Tegel, C. Winsnes, C. Zhang, M. Zwahlen, A. Mardinoglu, F. Pontén, K. von Feilitzen, K.S. Lilley, M. Uhlén, E. Lundberg, A subcellular map of the human proteome, Science. 356 (2017).

[30] F. Antunes, E. Cadenas, Estimation of H2O2 gradients across biomembranes, Febs Letters. 475 (2000) 121–126. doi:doi:10.1016/S0003-9861(02)00049-8.

[31] R. Benfeitas, G. Selvaggio, F. Antunes, P.M.B.M. Coelho, A. Salvador, Hydrogen peroxide metabolism and sensing in human erythrocytes: A validated kinetic model and reappraisal of the role of peroxiredoxin II, Free Radical Biology and Medicine. 74 (2014) 35–49. doi:10.1016/j.freeradbiomed.2014.06.007.

[32] B.K. Huang, H.D. Sikes, Quantifying intracellular hydrogen peroxide perturbations in terms of concentration, Redox Biology. 2 (2014) 955–962. doi:10.1016/j.redox.2014.08.001.

[33] M.C. Sobotta, A.G. Barata, U. Schmidt, S. Mueller, G. Millonig, T.P. Dick, Exposing cells to H2O2: A quantitative comparison between continuous low-dose and one-time high-dose treatments, Free Radical Biology and Medicine. 60 (2013) 325–335. doi:10.1016/j.freeradbiomed.2013.02.017.

[34] B.A. Wagner, J.R. Witmer, T.J. van 't Erve, G.R. Buettner, An Assay for the Rate of Removal of Extracellular Hydrogen Peroxide by Cells., Redox Biology. 1 (2013) 210–217. doi:10.1016/j.redox.2013.01.011.

[35] C.M. Doskey, V. Buranasudja, B.A. Wagner, J.G. Wilkes, J. Du, J.J. Cullen, G.R. Buettner, Tumor cells have decreased ability to metabolize H2O2: Implications for pharmacological ascorbate in cancer therapy, Redox Biology. 10 (2016) 274–284. doi:10.1016/j.redox.2016.10.010.

[36] V. Oliveira-Marques, T. Silva, F. Cunha, G. Covas, H.S. Marinho, F. Antunes, L. Cyrne, A quantitative study of the cell-type specific modulation of c-Rel by hydrogen peroxide and TNF-a, Redox Biology. 1 (2013) 347–352. doi:10.1016/j.redox.2013.05.004.

[37] V. de Oliveira-Marques, L. Cyrne, H.S. Marinho, F. Antunes, A quantitative study of NF-kappa B activation by H2O2: Relevance in inflammation and synergy with TNF-alpha, Journal of Immunology. 178 (2007) 3893–3902.

[38] L. Flohé, G. Loschen, W.A. Gunzler, E. Eichele, Glutathione peroxidase, V. The kinetic mechanism, Hoppe-Seylers Zeitschrift Fur Physiologische Chemie. 353 (1972) 987–999.

[39] G. Takebe, J. Yarimizu, Y. Saito, T. Hayashi, H. Nakamura, J. Yodoi, S. Nagasawa, K. Takahashi, A comparative study on the hydroperoxide and thiol specificity of the glutathione peroxidase family and selenoprotein P, Journal Of Biological Chemistry. 277 (2002) 41254–41258. doi:10.1074/jbc.M202773200.

[40] A.B. Fisher, C. Dodia, Y. Manevich, J.-W. Chen, S.I. Feinstein, Phospholipid Hydroperoxides Are Substrates for Non-selenium Glutathione Peroxidase, Journal Of Biological Chemistry. 274 (1999) 21326–21334.

[41] Y. Manevich, S.I. Feinstein, A.B. Fisher, Activation of the antioxidant enzyme 1-CYS peroxiredoxin requires glutathionylation mediated by heterodimerization with GST,

Proceedings of the National Academy of Sciences. 101 (2004) 3780–3785. doi:10.1073/pnas.0400181101.

[42] S. Zhou, E.M. Sorokina, S. Harper, H. Li, L. Ralat, C. Dodia, D.W. Speicher, S.I. Feinstein, A.B. Fisher, Peroxiredoxin 6 homodimerization and heterodimerization with glutathione S-transferase pi are required for its peroxidase but not phospholipase A2 activity, Free Radical Biology and Medicine. 94 (2016) 145–156. doi:10.1016/j.freeradbiomed.2016.02.012.

[43] R.E. Hansen, D. Roth, J.R. Winther, Quantifying the global cellular thiol-disulfide status, Proceedings of the National Academy of Sciences. 106 (2009) 422–427. doi:10.1073/pnas.0812149106.

[44] N.S. Kosower, E.M. Kosower, B. Wertheim, W.S. Correa, Diamide, a new reagent for the intracellular oxidation of glutathione to the disulfide, Biochemical and Biophysical Research Communications. 37 (1969) 593–596. doi:10.1016/0006-291X(69)90850-X.

[45] C.C. Winterbourn, D. Metodiewa, Reactivity of biologically important thiol compounds with superoxide and hydrogen peroxide, 27 (1999).

[46] J.R. Stone, An assessment of proposed mechanisms for sensing hydrogen peroxide in mammalian systems, Archives Of Biochemistry And Biophysics. 422 (2004) 119–124.

[47] H.S. Marinho, C. Real, L. Cyrne, H. Soares, F. Antunes, Hydrogen peroxide sensing, signaling and regulation of transcription factors., Redox Biology. 2 (2014) 535–562. doi:10.1016/j.redox.2014.02.006.

[48] E. Weerapana, C. Wang, G.M. Simon, F. Richter, S. Khare, M.B.D. Dillon, D.A. Bachovchin, K. Mowen, D. Baker, B.F. Cravatt, Quantitative reactivity profiling predicts functional cysteines in proteomes, Nature. 468 (2010) 790–795.

[49] J.W. Baty, M.B. Hampton, C.C. Winterbourn, Proteomic detection of hydrogen peroxide-sensitive thiol proteins in Jurkat cells, Biochem. J. 389 (2005) 785–795. doi:10.1042/bj20050337.

[50] N. Le Moan, G. Clement, S. Le Maout, F. Tacnet, M.B. Toledano, The Saccharomyces cerevisiae proteome of oxidized protein thiols - Contrasted functions for the thioredoxin and glutathione pathways, Journal Of Biological Chemistry. 281 (2006) 10420–10430.

[51] K. Araki, H. Kusano, N. Sasaki, R. Tanaka, T. Hatta, K. Fukui, T. Natsume, Redox Sensitivities of Global Cellular Cysteine Residues under Reductive and Oxidative Stress,

Journal of Proteome Research. 15 (2016) 2548–2559. doi:10.1021/acs.jproteome.6b00087.

[52] T. Geiger, A. Wehner, C. Schaab, J. Cox, M. Mann, Comparative Proteomic Analysis of Eleven Common Cell Lines Reveals Ubiquitous but Varying Expression of Most Proteins, Molecular & Cellular Proteomics. 11 (2012) M111.014050-M111.014050. doi:10.1074/mcp.M111.014050.

[53] C. Little, P.J. O'brien, Mechanism of Peroxide-Inactivation of the Sulphydryl Enzyme Glyceraldehyde-3-Phosphate Dehydrogenase, European Journal of Biochemistry. 10 (1969) 533–538. doi:10.1111/j.1432-1033.1969.tb00721.x.

[54] C.C. Winterbourn, M.B. Hampton, Thiol chemistry and specificity in redox signaling, Free Radical Biology and Medicine. 45 (2008) 549–561. doi:10.1016/j.freeradbiomed.2008.05.004.

[55] N.J. Adimora, D.P. Jones, M.L. Kemp, A Model of Redox Kinetics Implicates the Thiol Proteome in Cellular Hydrogen Peroxide Responses, Antioxidants & Redox Signaling. 13 (2010) 731–743. doi:10.1089/ars.2009.2968.

[56] L.E. Tomalin, A.M. Day, Z.E. Underwood, G.R. Smith, P. Dalle Pezze, C. Rallis, W. Patel, B.C. Dickinson, J. Bähler, T.F. Brewer, C.J.-L. Chang, D.P. Shanley, E.A. Veal, Increasing extracellular H2O2 produces a bi-phasic response in intracellular H2O2, with peroxiredoxin hyperoxidation only triggered once the cellular H2O2-buffering capacity is overwhelmed, Free Radical Biology and Medicine. 95 (2016) 333–348. doi:10.1016/j.freeradbiomed.2016.02.035.

[57] B. Morgan, D. Ezeriņa, T.N.E. Amoako, J. Riemer, M. Seedorf, T.P. Dick, Multiple glutathione disulfide removal pathways mediate cytosolic redox homeostasis., Nature Chemical Biology. 9 (2013) 119–25. doi:10.1038/nchembio.1142.

[58] S. Mueller, H.D. Riedel, W. Stremmel, Determination of catalase activity at physiological hydrogen peroxide concentrations, Analytical Biochemistry. 245 (1997) 55–60.

[59] J. Switala, P.C. Loewen, Diversity of properties among catalases, Archives of Biochemistry and Biophysics. 401 (2002) 145–154. doi:10.1016/S0003-9861(02)00049-8.

[60] S.G. Rhee, S.W. Kang, T.S. Chang, W. Jeong, K. Kim, Peroxiredoxin, a novel family of peroxidases, IUBMB Life. 52 (2001) 35–41. doi:10.1080/15216540252774748.

[61] B. Manta, M. Hugo, C. Ortiz, G. Ferrer-Sueta, M. Trujillo, A. Denicola, The peroxidase and

peroxynitrite reductase activity of human erythrocyte peroxiredoxin 2., Archives of Biochemistry and Biophysics. 484 (2009) 146–54. doi:10.1016/j.abb.2008.11.017.

[62] A.V. Peskin, F.M. Low, L.N. Paton, G.J. Maghzal, M.B. Hampton, C.C. Winterbourn, The High Reactivity of Peroxiredoxin 2 with H(2)O(2) Is Not Reflected in Its Reaction with Other Oxidants and Thiol Reagents, The Journal of Biological Chemistry. 282 (2007) 11885–11892. doi:10.1074/jbc.M700339200.

[63] A. V Peskin, N. Dickerhof, R.A. Poynton, L.N. Paton, P.E. Pace, M.B. Hampton, C.C. Winterbourn, Hyperoxidation of peroxiredoxins 2 and 3: Rate constants for the reactions of the sulfenic acid of the peroxidatic cysteine, J. Biol. Chem. 288 (2013) 14170–14177. doi:10.1074/jbc.M113.460881.

[64] R.A. Poynton, A. V Peskin, A.C. Haynes, W.T. Lowther, M.B. Hampton, C.C. Winterbourn, Kinetic analysis of structural influences on the susceptibility of peroxiredoxins 2 and 3 to hyperoxidation, Biochemical Journal. 473 (2016) 411–421. doi:10.1042/BJ20150572.

[65] L.A.C. Carvalho, D.R. Truzzi, T.S. Fallani, S. V Alves, J.C. Toledo Junior, O. Augusto, L.E.S. Netto, F.C. Meotti, Urate hydroperoxide oxidizes human peroxiredoxin 1 and peroxiredoxin 2., The Journal of Biological Chemistry. (2017) jbc.M116.767657. doi:10.1074/jbc.M116.767657.

[66] A. V Peskin, N. Dickerhof, R.A. Poynton, L.N. Paton, P.E. Pace, M.B. Hampton, C.C. Winterbourn, Hyperoxidation of peroxiredoxins 2 and 3: Rate constants for the reactions of the sulfenic acid of the peroxidatic cysteine, The Journal of Biological Chemistry. 288 (2013) 14170–14177. doi:10.1074/jbc.M113.460881.

[67] L.A.C. Carvalho, D.R. Truzzi, T.S. Fallani, S. V Alves, J.C. Toledo Junior, O. Augusto, L.E.S. Netto, F.C. Meotti, Urate hydroperoxide oxidizes human peroxiredoxin 1 and peroxiredoxin 2., The Journal of Biological Chemistry. 292 (2017) 8705–8715. doi:10.1074/jbc.M116.767657.

[68] H.A. Woo, S.H. Yim, D.H. Shin, D. Kang, D.-Y. Yu, S.G. Rhee, Inactivation of peroxiredoxin I by phosphorylation allows localized H(2)O(2) accumulation for cell signaling, Cell. 140 (2010) 517–528.

[69] J.H. Seo, J.C. Lim, D.Y. Lee, K.S. Kim, G. Piszczek, H.W. Nam, Y.S. Kim, T. Ahn, C.H. Yun, K. Kim, P.B. Chock, H.Z. Chae, Novel Protective Mechanism against Irreversible Hyperoxidation of Peroxiredoxin N-alpha-terminal acetylation of human peroxiredoxin, Journal Of Biological Chemistry. 284 (2009) 13455–13465. doi:10.1074/jbc.M900641200.

[70] K.-S. Yang, S.W. Kang, H.A. Woo, S.C. Hwang, H.Z. Chae, K. Kim, S.G. Rhee, Inactivation of human peroxiredoxin I during catalysis as the result of the oxidation of the catalytic site cysteine to cysteine-sulfinic acid, J Biol Chem. 277 (2002) 38029–38036.

[71] J.W. Park, J.J. Mieyal, S.G. Rhee, P.B. Chock, Deglutathionylation of 2-Cys Peroxiredoxin Is Specifically Catalyzed by Sulfiredoxin, The Journal of Biological Chemistry. 284 (2009) 23364–23374. doi:10.1074/jbc.M109.021394.

[72] A. V. Peskin, P.E. Pace, J.B. Behring, L.N. Paton, M. Soethoudt, M.M. Bachschmid, C.C. Winterbourn, Glutathionylation of the Active Site Cysteines of Peroxiredoxin 2 and Recycling by Glutaredoxin, The Journal of Biological Chemistry. 291 (2016) 3053–3062. doi:10.1074/jbc.M115.692798.

[73] H.Z. Chae, H.J. Kim, S.W. Kang, S.G. Rhee, Characterization of three isoforms of mammalian peroxiredoxin that reduce peroxides in the presence of thioredoxin, Diabetes Research and Clinical Practice. 45 (1999) 101–112. doi:10.1016/S0168-8227(99)00037-6.

[74] B.K. Huang, T.F. Langford, H.D. Sikes, Using Sensors and Generators of H 2 O 2 to Elucidate the Toxicity Mechanism of Piperlongumine and Phenethyl Isothiocyanate, Antioxidants & Redox Signaling. 24 (2016) 924–938. doi:10.1089/ars.2015.6482.

[75] W.T. Lowther, A.C. Haynes, Reduction of cysteine sulfinic acid in eukaryotic, typical 2-Cys peroxiredoxins by sulfiredoxin., Antioxidants & Redox Signaling. 15 (2011) 99–109. doi:10.1089/ars.2010.3564.

[76] X. Roussel, A. Kriznik, C. Richard, S. Rahuel-Clermont, G. Branlant, Catalytic Mechanism of Sulfiredoxin from Saccharomyces cerevisiae Passes through an Oxidized Disulfide Sulfiredoxin Intermediate That Is Reduced by Thioredoxin, Journal Of Biological Chemistry. 284 (2009) 33048–33055. doi:10.1074/jbc.M109.035352.

[77] X. Roussel, S. Boukhenouna, S. Rahuel-Clermont, G. Branlant, The rate-limiting step of sulfiredoxin is associated with the transfer of the γ-phosphate of ATP to the sulfinic acid of overoxidized typical 2-Cys peroxiredoxins, FEBS Letters. 585 (2011) 574–578. doi:10.1016/j.febslet.2011.01.012.

[78] X. Roussel, G. Béchade, A. Kriznik, A. Van Dorsselaer, S. Sanglier-Cianferani, G. Branlant, S. Rahuel-Clermont, Evidence for the Formation of a Covalent Thiosulfinate Intermediate with Peroxiredoxin in the Catalytic Mechanism of Sulfiredoxin, Journal of Biological Chemistry. 283 (2008) 22371–22382. doi:10.1074/jbc.M800493200.

[79] J.C. Moon, G.M. Kim, E.K. Kim, H.N. Lee, B. Ha, S.Y. Lee, H.H. Jang, Reversal of 2-Cys peroxiredoxin oligomerization by sulfiredoxin, Biochemical and Biophysical Research Communications. 432 (2013) 291–295. doi:10.1016/j.bbrc.2013.01.114.

[80] W. Jeong, S.J. Park, T.-S. Chang, D.-Y. Lee, S.G. Rhee, Molecular Mechanism of the Reduction of Cysteine Sulfinic Acid of Peroxiredoxin to Cysteine by Mammalian Sulfiredoxin, Journal of Biological Chemistry. 281 (2006) 14400–14407. doi:10.1074/jbc.M511082200.

[81] S. Boukhenouna, H. Mazon, G. Branlant, C. Jacob, M.B. Toledano, S. Rahuel-Clermont, Evidence That Glutathione and the Glutathione System Efficiently Recycle 1-Cys Sulfiredoxin *In Vivo*, Antioxidants & Redox Signaling. 22 (2015) 731–743. doi:10.1089/ars.2014.5998.

[82] T.-S. Chang, W. Jeong, H.A. Woo, S.M. Lee, S. Park, S.G. Rhee, Characterization of mammalian sulfiredoxin and its reactivation of hyperoxidized peroxiredoxin through reduction of cysteine sulfinic acid in the active site to cysteine, J. Biol. Chem. 279 (2004) 50994–51001.

[83] H.A. Woo, S.W. Kang, H.K. Kim, K.-S. Yang, H.Z. Chae, S.G. Rhee, Reversible oxidation of the active site cysteine of peroxiredoxins to cysteine sulfinic acid. Immunoblot detection with antibodies specific for the hyperoxidized cysteine-containing sequence, J Biol Chem. 278 (2003) 47361–47364.

[84] M. Chevallet, E. Wagner, S. Luche, A. van Dorsselaer, E. Leize-Wagner, T. Rabilloud, Regeneration of peroxiredoxins during recovery after oxidative stress - Only some overoxidized peroxiredoxins can be reduced during recovery after oxidative stress, Journal Of Biological Chemistry. 278 (2003) 37146–37153. doi:10.1074/jbc.M305161200.

[85] S.J. Wei, A. Botero, K. Hirota, C.M. Bradbury, S. Markovina, A. Laszlo, D.R. Spitz, P.C. Goswami, J. Yodoi, D. Gius, Thioredoxin nuclear translocation and interaction with redox factor-1 activates the activator protein-1 transcription factor in response to ionizing radiation., Cancer Research. 60 (2000) 6688–95.

[86] S.J. Montano, J. Lu, T.N. Gustafsson, A. Holmgren, Activity assays of mammalian thioredoxin and thioredoxin reductase: Fluorescent disulfide substrates, mechanisms, and use with tissue samples, Analytical Biochemistry. 449 (2014) 139–146. doi:10.1016/J.AB.2013.12.025.

[87] S. Lee, S.M. Kim, R.T. Lee, Thioredoxin and Thioredoxin Target Proteins: From Molecular

1440 Mechanisms to Functional Significance, Antioxidants and Redox Signaling. 18 (2012)
1441 1165–1207. doi:10.1089/ars.2011.4322.

1442 [88] X. Wang, S. Ling, D. Zhao, Q. Sun, Q. Li, F. Wu, J. Nie, L. Qu, B. Wang, X. Shen, Y. Bai, Y. Li,
1443 Y. Li, Redox Regulation of Actin by Thioredoxin-1 Is Mediated by the Interaction of the
1444 Proteins via Cysteine 62, Antioxidants & Redox Signaling. 13 (2010) 565–573.
1445 doi:10.1089/ars.2009.2833.

1446 [89] A. Nishiyama, M. Matsui, S. Iwata, K. Hirota, H. Masutani, H. Nakamura, Y. Takagi, H.
1447 Sono, Y. Gon, J. Yodoi, Identification of thioredoxin-binding protein-2/vitamin D(3) up-
1448 regulated protein 1 as a negative regulator of thioredoxin function and expression., The
1449 Journal of Biological Chemistry. 274 (1999) 21645–50. doi:10.1074/JBC.274.31.21645.

1450 [90] K. Hirota, M. Matsui, S. Iwata, A. Nishiyama, K. Mori, J. Yodoi, AP-1 transcriptional activity
1451 is regulated by a direct association between thioredoxin and Ref-1., Proceedings of the
1452 National Academy of Sciences of the United States of America. 94 (1997) 3633–8.

1453 [91] P. Schroeder, R. Popp, B. Wiegand, J. Altschmied, J. Haendeler, Nuclear redox-signaling is
1454 essential for apoptosis inhibition in endothelial cells--important role for nuclear
1455 thioredoxin-1., Arteriosclerosis, Thrombosis, and Vascular Biology. 27 (2007) 2325–31.
1456 doi:10.1161/ATVBAHA.107.149419.

1457 [92] M. Kontou, C. Adelfalk, M. Hirsch-Kauffmann, M. Schweiger, Suboptimal Action of NF-κB
1458 in Fanconi Anemia Cells Results from Low Levels of Thioredoxin, Biological Chemistry.
1459 384 (2003). doi:10.1515/BC.2003.166.

1460 [93] I. Grattagliano, S. Russmann, V.O. Palmieri, P. Portincasa, G. Palasciano, B.H. Lauterburg,
1461 Glutathione peroxidase, thioredoxin, and membrane protein changes in erythrocytes
1462 predict ribavirin-induced anemia[ast], Clin Pharmacol Ther. 78 (2005) 422–432.

1463 [94] R. Eidukevicius, D. Characiejus, R. Janavicius, N. Kazlauskaite, V. Pasukoniene, M.
1464 Mauricas, W. Den Otter, A method to estimate cell cycle time and growth fraction using
1465 bromodeoxyuridine-flow cytometry data from a single sample., BMC Cancer. 5 (2005)
1466 122. doi:10.1186/1471-2407-5-122.

1467 [95] F.M. Low, M.B. Hampton, A. V Peskin, C.C. Winterbourn, Peroxiredoxin 2 functions as a
1468 noncatalytic scavenger of low-level hydrogen peroxide in the erythrocyte, Blood. 109
1469 (2007) 2611–2617. doi:10.1182/blood-2006-09-048728.

1470 [96] L.W. Zhong, E.S.J. Arner, A. Holmgren, Structure and mechanism of mammalian

thioredoxin reductase: The active site is a redox-active selenolthiol/selenenylsulfide formed from the conserved cysteine-selenocysteine sequence, Proceedings Of The National Academy Of Sciences Of The United States Of America. 97 (2000) 5854–5859.

[97] S. Gromer, L.D. Arscott, C.H. Williams, R.H. Schirmer, K. Becker, Human placenta thioredoxin reductase. Isolation of the selenoenzyme, steady state kinetics, and inhibition by therapeutic gold compounds, 273 (1998) 20096–20101. doi:10.1074/jbc.273.32.20096.

[98] A.A. Turanov, D. Su, V.N. Gladyshev, Characterization of Alternative Cytosolic Forms and Cellular Targets of Mouse Mitochondrial Thioredoxin Reductase, Journal of Biological Chemistry. 281 (2006) 22953–22963. doi:10.1074/jbc.M604326200.

[99] S. Urig, K. Becker, On the potential of thioredoxin reductase inhibitors for cancer therapy., Seminars in Cancer Biology. 16 (2006) 452–65. doi:10.1016/j.semcancer.2006.09.004.

[100] R.A. Cairns, I.S. Harris, T.W. Mak, Regulation of cancer cell metabolism, Nature Reviews Cancer. 11 (2011) 85–95. doi:10.1038/nrc2981.

[101] J. Fan, J. Ye, J.J. Kamphorst, T. Shlomi, C.B. Thompson, J.D. Rabinowitz, Quantitative flux analysis reveals folate-dependent NADPH production., Nature. 510 (2014) 298–302. doi:10.1038/nature13236.

[102] M. V Ursini, A. Parrella, G. Rosa, S. Salzano, G. Martini, Enhanced expression of glucose-6-phosphate dehydrogenase in human cells sustaining oxidative stress., Biochemical Journal. 323 (1997) 801–6.

[103] H.N. Kirkman, W.G. Wilson, E.H. Clemons, Regulation of glucose-6-phosphate-dehydrogenase .1. Intact red- cells, Journal of Laboratory and Clinical Medicine. 95 (1980) 877–887.

[104] A. Salvador, M.A. Savageau, Quantitative evolutionary design of glucose 6-phosphate dehydrogenase expression in human erythrocytes, Proceedings of the National Academy of Sciences. 100 (2003) 14463–14468. doi:10.1073/pnas.2335687100.

[105] K. Birsoy, R. Possemato, F.K. Lorbeer, E.C. Bayraktar, P. Thiru, B. Yucel, T. Wang, W.W. Chen, C.B. Clish, D.M. Sabatini, Metabolic determinants of cancer cell sensitivity to glucose limitation and biguanides., Nature. 508 (2014) 108–12. doi:10.1038/nature13110.

[106] A. Kuehne, H. Emmert, J. Soehle, M. Winnefeld, F. Fischer, H. Wenck, S. Gallinat, L. Terstegen, R. Lucius, J. Hildebrand, N. Zamboni, Acute Activation of Oxidative Pentose Phosphate Pathway as First-Line Response to Oxidative Stress in Human Skin Cells., Molecular Cell. 59 (2015) 359–371. doi:10.1016/j.molcel.2015.06.017.

[107] A. Salvador, M.A. Savageau, Evolution of enzymes in a series is driven by dissimilar functional demands, Proceedings of the National Academy of Sciences. 103 (2006) 2226–2231. doi:10.1073/pnas.0510776103.

[108] M.R. Branco, H.S. Marinho, L. Cyrne, F. Antunes, Decrease of H2O2 plasma membrane permeability during adaptation to H2O2 in Saccharomyces cerevisiae., The Journal of Biological Chemistry. 279 (2004) 6501–6506. doi:10.1074/jbc.M311818200.

[109] C.D. Powell, D.E. Quain, K.A. Smart, Chitin scar breaks in aged Saccharomyces cerevisiae, Microbiology. 149 (2003) 3129–3137. doi:10.1099/mic.0.25940-0.

[110] M. Kamihira, M. Taniguchi, T. Kobayashi, Sterilization of Microorganisms with Supercritical Carbon Dioxide, Agricultural and Biological Chemistry. 51 (1987) 407–412. doi:10.1080/00021369.1987.10868053.

[111] P. Jorgensen, J.L. Nishikawa, B.-J. Breitkreutz, M. Tyers, Systematic Identification of Pathways That Couple Cell Growth and Division in Yeast, Science. 297 (2002) 395–400. doi:10.1126/science.1070850.

[112] M. Uchida, Y. Sun, G. McDermott, C. Knoechel, M.A. Le Gros, D. Parkinson, D.G. Drubin, C.A. Larabell, Quantitative analysis of yeast internal architecture using soft X-ray tomography., Yeast (Chichester, England). 28 (2011) 227–36. doi:10.1002/yea.1834.

[113] S. Ghaemmaghami, W.-K.K. Huh, K. Bower, R.W. Howson, A. Belle, N. Dephoure, E.K. O'Shea, J.S. Weissman, Global analysis of protein expression in yeast, Nature. 425 (2003) 737–741. doi:10.1038/nature02046.

[114] J.E. Erman, L.B. Vitello, Yeast cytochrome c peroxidase: mechanistic studies via protein engineering., Biochimica et Biophysica Acta. 1597 (2002) 193–220.

[115] N. Ertugay, H. Hamamci, Continuous cultivation of bakers' yeast: Change in cell composition at different dilution rates and effect of heat stress on trehalose level, Folia Microbiologica. 42 (1997) 463–467. doi:10.1007/BF02826554.

[116] J.S. Jeong, S.J. Kwon, S.W. Kang, S.G. Rhee, K. Kim, Purification and Characterization of a Second Type Thioredoxin Peroxidase (Type II TPx) from Saccharomyces cerevisiae†,

Biochemistry. 38 (1998) 776–783. doi:10.1021/BI9817818.

[117] C.A. Tairum, M.C. Santos, C.A. Breyer, R.R. Geyer, C.J. Nieves, S. Portillo-Ledesma, G. Ferrer-Sueta, J.C. Toledo, M.H. Toyama, O. Augusto, L.E.S. Netto, M.A. de Oliveira, M.A. de Oliveira, Catalytic Thr or Ser Residue Modulates Structural Switches in 2-Cys Peroxiredoxin by Distinct Mechanisms., Scientific Reports. 6 (2016) 33133. doi:10.1038/srep33133.

[118] R. Ogusucu, D. Rettori, D.C. Munhoz, L.E. Soares Netto, O. Augusto, Reactions of yeast thioredoxin peroxidases I and II with hydrogen peroxide and peroxynitrite: Rate constants by competitive kinetics, Free Radical Biology and Medicine. 42 (2007) 326–334. doi:10.1016/j.freeradbiomed.2006.10.042.

[119] C.A. Tairum Jr., M.A. de Oliveira, B.B. Horta, F.J. Zara, L.E.S. Netto, Disulfide Biochemistry in 2-Cys Peroxiredoxin: Requirement of Glu50 and Arg146 for the Reduction of Yeast Tsa1 by Thioredoxin, Journal of Molecular Biology. 424 (2012) 28–41. doi:10.1016/j.jmb.2012.09.008.

[120] M.A. Oliveira, K.F. Discola, S. V. Alves, F.J. Medrano, B.G. Guimarães, L.E.S. Netto, Insights into the Specificity of Thioredoxin Reductase−Thioredoxin Interactions. A Structural and Functional Investigation of the Yeast Thioredoxin System, Biochemistry. 49 (2010) 3317–3326. doi:10.1021/bi901962p.

[121] D.C. Munhoz, L.E.S. Netto, Cytosolic Thioredoxin Peroxidase I and II Are Important Defenses of Yeast against Organic Hydroperoxide Insult CATALASES AND PEROXIREDOXINS COOPERATE IN THE DECOMPOSITION OF H2O2 BY YEAST, Journal of Biological Chemistry. 279 (2004) 35219–35227. doi:10.1074/jbc.M313773200.

[122] F.-M. Lian, J. Yu, X.-X. Ma, X.-J. Yu, Y. Chen, C.-Z. Zhou, Structural snapshots of yeast alkyl hydroperoxide reductase Ahp1 peroxiredoxin reveal a novel two-cysteine mechanism of electron transfer to eliminate reactive oxygen species., The Journal of Biological Chemistry. 287 (2012) 17077–87. doi:10.1074/jbc.M112.357368.